Measuring the tau polarisation at the ILC and Optimisation study of the Asian GEM Module

by

Keita Yumino

A Doctor thesis

Submitted to
The Graduate University for Advanced Studies, SOKENDAI
on June 30, 2023
for the Degree of Doctor of Philosophy

Supervisor: Assoc. Prof. Daniel Jeans
Cosupervisor: Prof. Manobu Tanaka

CONTENTS

LIST OF FIGURES

Abstract

The International Linear Collider (ILC) is a next-generation high-energy electron-positron linear collider whose design and development are being promoted through international collaboration and has been proposed to study physics at the tera-scale and beyond. In the ILC, electrons and positrons, which are elementary particles, collide with each other, thus enabling clean initial conditions. This clean initial state is ideal for high-precision measurements and is expected to extend and complement the results of the Large Hadron Collider (LHC). This thesis consists of two major parts. The first part is tau reconstruction and tau polarisation measurements at the International Large Detector (ILD) which is one of the detector concepts at the ILC. The second part is about the Time Projection Chamber (TPC), which is the central tracker of the ILD which plays a central role in the measurements and about the optimisation of Gas Electron Multiplier (GEM), one of the Micro Pattern Gaseous Detector (MPGD).

In the first part of the thesis, the reconstruction of tau lepton pair and the measurement of the tau polarisation at the ILC operation at 250 GeV with polarized electron and positron beams with and an integrated luminosity of were investigated using Geant4 simulation in ILD. Collision of electron and positron generates tau lepton pair in the ILC and this process can be used to search for new interactions, also making use of our ability to measure the tau polarisation. Correct reconstruction of the tau decay mode is important for the tau polarisation measurement. In the Standard Model (SM), the properties of the fermion pair production process can be precisely predicted both within the SM including extensions to describe new physics. This thesis describes the reconstruction of the tau pair at a high-energy electron-positron collider and the use of the tau decays to measure their polarisation.

In the last half of the thesis, the optimisation study of the TPC equipped with a GEM is described. The physics program at collider experiments requires essentially perfect efficiency to reconstruct charged particles produced in collisions to measure their direction, their origin with respect to the interaction vertex to identify displaced vertices and to estimate their momentum. The analysis of tau leptons, as described in the first part of the thesis, relies on the good performance of the charged particle tracking system. In the ILC, MPGDs such as GEMs are used in the TPC endplate to amplify and detect ionized electrons in the reconstruction of charged particle trajectories. In the GEM-based module currently under development, Gas gain non-uniformity was found by measurement. The difference is about 50% at maximum. If the applied voltage is increased to obtain a sufficient signal even at a place where the gas gain is small, the gas gain becomes too large at a place where the gas gain is large, and the possibility of discharge will be too high. This discharge causes a part of the GEM to carbonize, resulting in a short circuit and making it impossible to apply voltage and to form the high voltage necessary for gas amplification. In this thesis, the study of GEM design optimization has been performed by theoretical approach to find the conditions under which the thickness dependence of the gas gain is minimum. Derived is an analytic equation of the gas gain variation and found the stability condition for the first time in this thesis.

CHAPTER 1

STANDARD MODEL OF PARTICLE PHYSICS

Contents

The Standard Model (SM) of strong and electroweak interactions is so far the most successful theory in particle physics, describing a wide range of properties of elementary particles.

In the SM, all known elementary particles are classified as quarks, leptons, gauge bosons and scalar bosons. There are three generations of leptons and quarks to constitute all matter, four gauge bosons that mediate strong and electroweak interactions, and scalar bosons (Higgs) that break electroweak symmetry and give mass to all elementary particles. Figure. 1 shows the particles in the SM [1].

In 2012, at the Large Hadron Collider (LHC) [2] in CERN, two experimental groups ATLAS [3, 4] and CMS [5] discovered a Higgs-like particle, which was a missing piece of SM particles. Figures. 1.2 shows the event display of the candidate reaction of $h \to 4e$ [6].

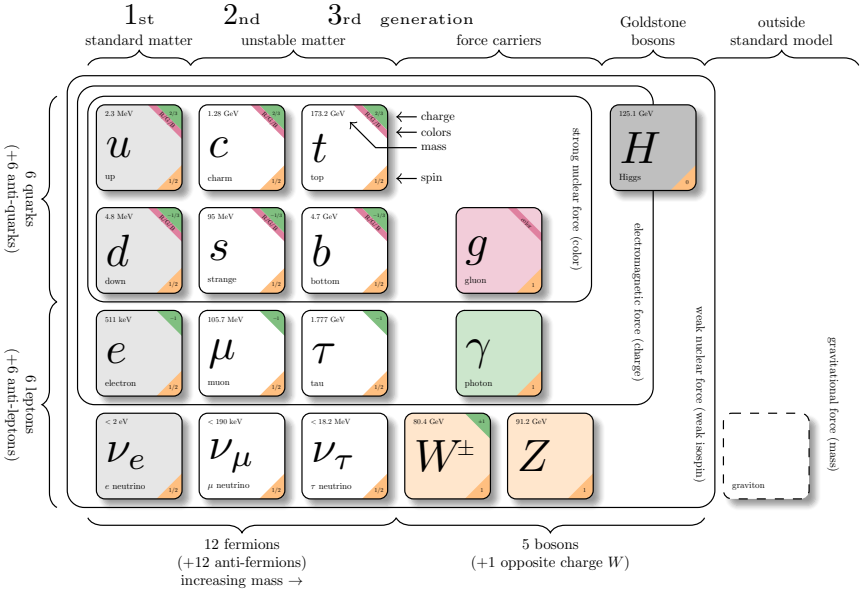

Figure 1.1: Standard Model particles.

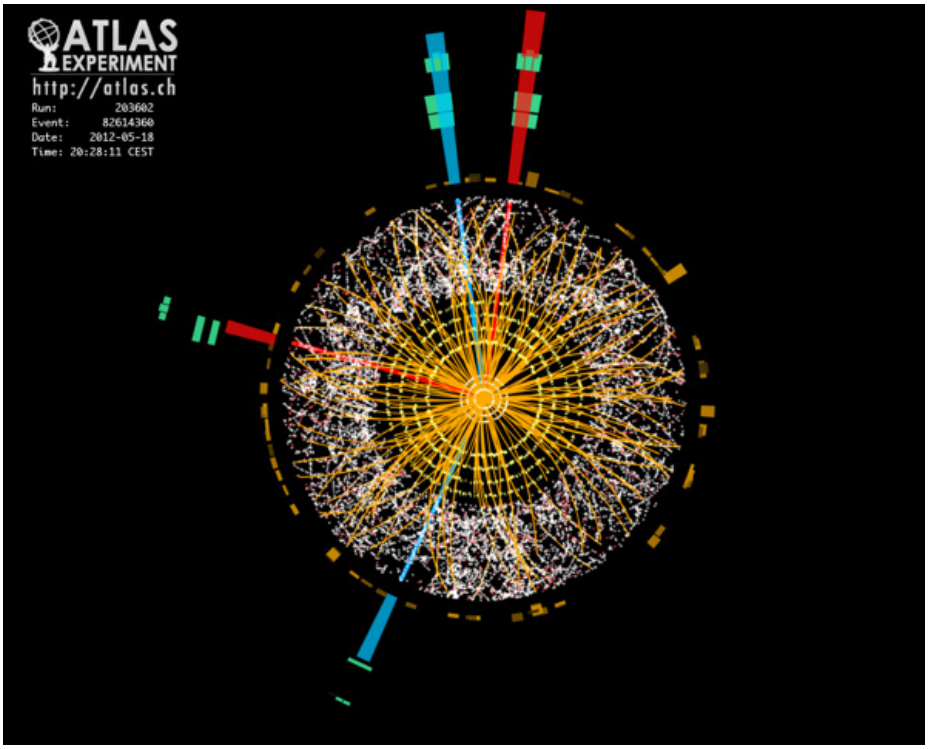

Figure 1.2: Event display of the candidate reaction of $h \to 4e$.

1.1 A theoretical framework

The following theoretical description of elementary particle physics are referred from several textbooks [7, 8].

1.1.1 $U(1)$ gauge symmetry and Electromagnetic Interaction

Maxwell equations describes the classical mechanical definition of the electromagnetism. As an extension of this, Quantum Electrodynamics (QED) describes the electromagnetic interaction.

In particle physics, the symmetry of the elementary particle field is fully specified by the Poincare invariance. The translational invariance of spacetime and the Lorentz invariance of spacetime satisfy the symmetry of rotation and boost, and the Lorentz invariance defines the symmetry of the field spacetime. Assuming a Dirac field describing a fermion ψ, the interaction with the gauge boson is naturally introduced when these invariances of a field are obtained by local transformations.

Dirac introduced an equation describing the free propagation of fermions with mass m by making the Schrödinger equation relativistic.

$$i\gamma^\mu \partial_\mu \psi - m_f \psi = 0 \tag{1.1}$$

where γ^μ are the Dirac matrices and ψ is the four component spinor representing the fermionic field as a function of spacetime coordinates $x^\mu = (t, x, y, z)$.

The Lagrangian density $\mathcal{L}$ of the Dirac equation can be written as

$$\mathcal{L} = i\bar{\psi}\gamma^\mu \partial_\mu \psi - m_f \bar{\psi}\psi \tag{1.2}$$

where $\bar{\psi} = \psi^\dagger \gamma^0$ is the adjoint spinor. The locally given phase transformation is described as follows.

$$\psi(x) \to \psi'(x) = e^{-iQ\chi(x)}\psi(x) \tag{1.3}$$

where Q represents charge of $U(1)$ symmetry and $\chi(x)$ denotes a spacetime coodinates.

The Lagrangian to which the local transformation is applied can be described as

$$\begin{aligned} \mathcal{L} = i\bar{\psi}\gamma^\mu \partial_\mu \psi - m_f \bar{\psi}\psi \quad &\to \quad i\bar{\psi}'\gamma^\mu \partial_\mu \psi' - m_f \bar{\psi}'\psi' \\ &= \quad i\bar{\psi}\gamma^\mu \partial_\mu \psi + \bar{\psi} Q \partial_\mu \chi(x) \psi - m_f \bar{\psi}'\psi' \\ &\neq \quad \mathcal{L} \end{aligned}$$

This Lagrangian is not invariant under the local phase transformation. However, the invariance can be achieved by introducing a covariant derivative and replacing with the partial derivative ∂_μ,

$$\partial_\mu \quad \to \quad D_\mu \equiv \partial_\mu + iQA_\mu(x) \tag{1.4}$$

where the new vector field $A_{mu(x)}$) is the electromagnetic field and required to transform as

$$A_\mu(x) \quad \to \quad A'_\mu(x) = A_\mu(x) + \partial_\mu \chi(x) \tag{1.5}$$

This local invariance leads to conservation of current, as suggested by Noether's theorem.

$$J^\mu = Q\bar{\psi}\gamma^\mu \psi. \tag{1.6}$$

With this new vector field and set of local invariant transformations, the given new Lagrangian, which is

$$\mathcal{L} = i\bar{\psi}\gamma^\mu D_\mu \psi - m_f \bar{\psi}\psi \tag{1.7}$$

can keep the invariance. The following Lagrangian density can be used to obtain Maxwell's equations:

$$\mathcal{L} = -\frac{1}{4}F_{\mu\nu}F^{\mu\nu} - J^{\mu}A_{\mu}, \tag{1.8}$$

where $F^{\mu\nu}$ is the electromagnetic field tensor or field strength tensor defined as $F^{\mu\nu} = \partial^{\mu}A^{\nu} - \partial^{\nu}A^{\mu}$. The first term $-\frac{1}{4}F_{\mu\nu}F^{\mu\nu}$ gives the kinetic energy of electromagnetic field.

Due to the requirement of local gauge invariance, it is necessary to introduce a vector particle γ, described by the field $A_{\mu}(x)$, whose form of interaction is automatically given. Adding the kinetic term of the γ just described to the above Lagrangian establishes a Lagrangian that can describe quantum electrodynamics:

$$\mathcal{L}_{QED} = \underbrace{i\bar{\psi}\gamma^{\mu}\partial_{\mu}\psi}_{\text{fermion kinetic term}} - \underbrace{m_f\bar{\psi}\psi}_{\text{fermion mass term}} - \underbrace{Q\bar{\psi}\gamma^{\mu}A_{\mu}\psi}_{\text{interaction term}} - \underbrace{\frac{1}{4}F_{\mu\nu}F^{\mu\nu}}_{\text{field kinetic term}} \tag{1.9}$$

It might seem that the field A_{μ} can take mass term as a coefficient of a quadratic term of the field like $m^2A^{\mu}A_{\mu}$. However, this would break gauge invariance, is not invariant under the local transformation. Thus, the mass of the A_{μ} must be 0 and this is consistent with experimantal result that the mass of the photon is 0.

1.1.2 $SU(2)$ gauge symmetry and Weak Interaction

Let's assume that the Dirac Lagrangian is given.

$$\mathcal{L} = i\bar{\Psi}\gamma^{\mu}\partial_{\mu}\Psi \tag{1.10}$$

where Ψ is Dirac spinor which is regarded as a doublet consisting of two component Dirac fields e, ν_e by considering the internal space symmetry of a fermion.

$SU(2)$ transformation can be applied to the Dirac spinor as

$$\Psi \to \Psi' = e^{-i\vec{\lambda}(x)\cdot\tau}\Psi(x) \tag{1.11}$$

with $\vec{\lambda}$ and τ being a real vector and the Pauli matrices, respectively.

$$\vec{\lambda}\cdot\tau = \lambda_1\begin{pmatrix}0 & 1\\ 1 & 0\end{pmatrix} + \lambda_2\begin{pmatrix}0 & -i\\ i & 0\end{pmatrix} + \lambda_3\begin{pmatrix}1 & 0\\ 0 & -1\end{pmatrix} \tag{1.12}$$

The invariance of the Dirac Lagrangian under the transformation for a massless fermion is

$$\begin{aligned}\mathcal{L} = i\bar{\Psi}\gamma^{\mu}\partial_{\mu}\Psi \quad &\to \quad i\bar{\Psi}'\gamma^{\mu}\partial_{\mu}\Psi'\\ &\approx \quad (1+i\vec{\lambda}(x)\cdot\tau)i\bar{\Psi}\gamma^{\mu}\partial_{\mu}(1-\vec{\lambda}(x)\cdot\tau)\Psi\\ &= \quad i\bar{\Psi}\gamma^{\mu}\partial_{\mu}\Psi + \bar{\Psi}\gamma^{\mu}\partial_{\mu}\vec{\lambda}(x)\cdot\tau\Psi\\ &\neq \quad \mathcal{L}\end{aligned}$$

The covariant derivative is introduced in order to preserve the invariance under local $SU(2)$ transformations:

$$\partial_{\mu} \to D_{\mu} \equiv \partial_{\mu} + i\frac{1}{2}g_2\mathbf{W}_{\mu}(x) \tag{1.13}$$

where a $SU(2)$ coupling g_2 is introduced and the three vector fields $W_\mu(x)$ are massless and required to transform as

$$W_\mu(x) \to W'_\mu(x) = U(x)W(x)U(x)^\dagger + \frac{2i}{g_2}(\partial_\mu U(x))U(x)^\dagger \tag{1.14}$$

where $U(x)$ is the $SU(2)$ transformation.

The Lagrangian being invariant under local $SU(2)$ transformations can be written as

$$\mathcal{L}_{SU(2)} = i\bar{\Psi}\gamma^\mu\partial_\mu\Psi - ig_2 W_\mu(x)\bar{\Psi}\gamma^\mu\Psi \tag{1.15}$$

1.1.3 $SU(2) \times U(1)$ gauge transformation

In the SM, the weak interaction is coupled only to the left-handed doublet and there are no right-handed neutrinos. Therefore, different gauge transformations must be applied to left- and right-handed particles. Let's consider the doublet of left-handed electrons and electron-neutrinos and the singlet of right-handed electrons.

$$\begin{aligned}
L = \begin{pmatrix} \nu_L \\ e_L \end{pmatrix} &\to L' = \exp(-\frac{i}{2}\beta(x)Y)\exp(-\frac{i}{2}\alpha(x)\cdot\tau)L \\
&\sim (1 - \frac{i}{2}\beta(x)Y - \frac{i}{2}\alpha(x)\cdot\tau)L \\
e_R &\to e'_R = \exp(-\frac{i}{2}\beta(x)Y)e_R \\
&\sim (1 - \frac{i}{2}\beta(x)Y)e_R
\end{aligned}$$

where $\alpha(x), \beta(x)$ are functions of time and space, and Y is called the weak hypercharge which is a generator of $U(1)$. The covariant derivatives for both the doublet and the singlet are given as

$$\begin{aligned}
L : \partial_\mu &\to D_\mu = \partial_\mu + \frac{ig_1}{2}B_\mu Y + \frac{ig_2}{2}W_\mu\cdot\tau \\
e_R : \partial_\mu &\to D_\mu = \partial_\mu + \frac{ig_1}{2}B_\mu Y
\end{aligned}$$

where B_μ and W_μ are the gauge fields corresponding to the $U(1)$ and $SU(2)$ gauge transformations and τ is the three generator of $SU(2)$ transformation. Then,

$$\begin{aligned}
B_\mu(x) &\to B'_\mu(x) = B_\mu(x) + \frac{\partial_\mu\beta(x)}{g_1} \\
W_\mu(x) &\to W'_\mu(x) = U(x)W_\mu(x)U^\dagger(x) + \frac{2i}{g_2}(\partial_\mu U(x))U^\dagger(x)
\end{aligned}$$

The $SU(2) \times U(1)$ gauge invariant Lagrangian with the kinematic term of B_μ and W_μ is given as

$$\begin{aligned}
\mathcal{L}_{SU(2)\times U(1)} =& i\gamma^\mu L^\dagger(\partial_\mu + \frac{ig_1}{2}B_\mu Y + \frac{ig_2}{2}W_\mu\cdot\tau)L + i\gamma^\mu e_R^\dagger(\partial_\mu + \frac{ig_1}{2}B_\mu Y)e_R \\
&- \frac{1}{4}B_{\mu\nu}B^{\mu\nu} - \sum\frac{1}{4}W^i_{\mu\nu}W_i^{\mu\nu}
\end{aligned} \tag{1.16}$$

where $W_{\mu\nu}$ is the field strength tensor:

$$W_{\mu\nu} = \partial_\mu W_{\nu i} - \partial_\nu W_{\mu i} - \sum_{jk} \epsilon_{ijk} W_{\mu j} W_{\nu k}.$$

B_μ and W_μ are mixed after the spontaneous symmetry breaking. The fields of photon and Z boson, A_μ and Z_μ can be described as

$$\begin{aligned} A_\mu &\rightarrow B_\mu \cos\theta_W + W^3_\mu \sin\theta_W \\ Z_\mu &\rightarrow B_\mu \sin\theta_W - W^3_\mu \cos\theta_W \end{aligned}$$

where θ_W is the weak mixing angle (so-called Weinberg angle) which has the following relationship with the couplings g_1 and g_2:

$$\begin{aligned} \sin\theta_W &= \frac{g_1}{\sqrt{g_1^2 + g_2^2}} \\ \cos\theta_W &= \frac{g_2}{\sqrt{g_1^2 + g_2^2}}. \end{aligned}$$

1.1.4 The Higgs mechanism

There are no mass terms for fermions and gauge fields in the Lagrangian introduced in the previous section. The local gauge invariance requires the massless particles and is no longer valid when the mass terms are inserted into the Lagrangian by hand. However, it is experimentally confirmed that the fermions and W, Z bosons have masses, which violates the requirement of the local gauge invariance. This problem can be solved by introducing the spontaneous symmetry breaking where the electroweak symmertry is broken without introducing a massterm in the Lagrangian. The Higgs mechanism which is the simplest choice for this symmetry breaking can naturally give masses to the fermion fields and the gauge boson fields by introducing a $SU(2)_L$ doublet Φ which is composed of four real scalar fields $\phi_1, \phi_2, \phi_3, \phi_4$.

$$\Phi = \begin{pmatrix} \phi_1 + i\phi_2 \\ \phi_3 + i\phi_4 \end{pmatrix} \tag{1.17}$$

Then, the corresponding Lagrangian with the kinetic term and the potential term is given by

$$\mathcal{L}_H = (D^\mu \Phi)^\dagger (D_\mu \Phi) - V(\Phi^\dagger \Phi) \tag{1.18}$$

where D^μ is the electroweak covariant derivative:

$$D^\mu = \partial_\mu + \frac{ig_1}{2} B_\mu Y + \frac{ig_2}{2} W_\mu, \tag{1.19}$$

and $V(\Phi^\dagger \Phi)$ is the potential term:

$$V(\Phi^\dagger \Phi) = \mu^2 (\Phi^\dagger \Phi) + \lambda (\Phi^\dagger \Phi)^2 \tag{1.20}$$

where μ^2 and λ are real parameters. If μ^2 is negative, the non-zero global minimum can be found at (Figure.1.1.4 [9])

$$\Phi^\dagger \Phi = (\phi_1^2 + \phi_2^2 + \phi_3^2 + \phi_4^2) = -\frac{\mu^2}{2\lambda} \tag{1.21}$$

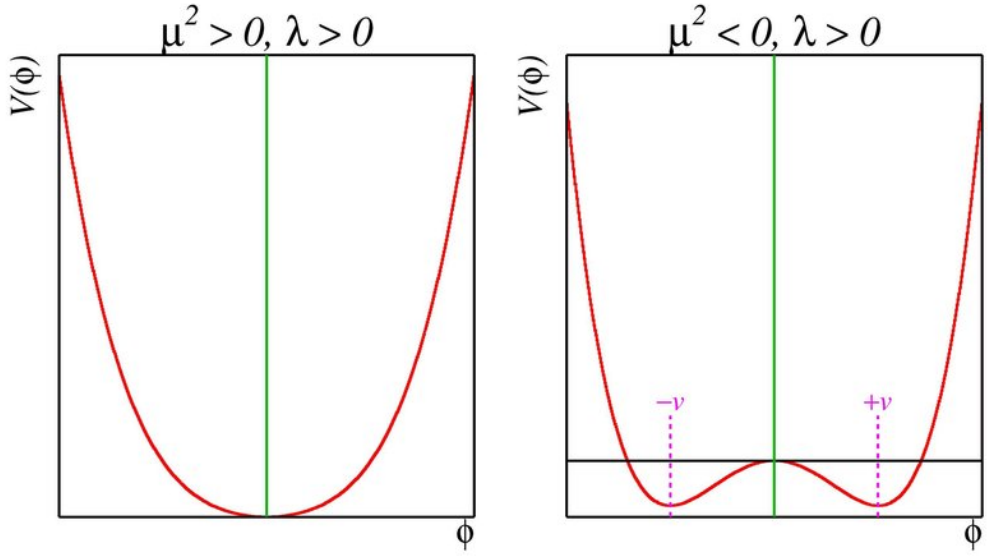

Figure 1.3: The Higgs potential of a scalar field ϕ.

The ground state of the vacuum, which is the minimum of the potential, has an infinite solutions, so any point on the 4-dimensional hypersphere can be chosen. Let us choose the point:

$$\phi^2_{1,min} = \phi^2_{2,min} = \phi^2_{4,min} = 0 \tag{1.22}$$

and

$$\phi^2_{3,min} = -\frac{\mu^2}{2\lambda} = v^2 \tag{1.23}$$

with the vacuum expectation value (VEV) of the field

$$v = \sqrt{-\frac{\mu^2}{2\lambda}} \tag{1.24}$$

The VEV of the complex scalar double can be written as

$$\Phi_0 \equiv \langle 0| \Phi |0\rangle = \frac{1}{\sqrt{2}} \begin{pmatrix} 0 \\ v \end{pmatrix} \tag{1.25}$$

This leads to the spontaneous $SU(2)$ symmetry breaking. We can write

$$\Phi(x) = \frac{1}{\sqrt{2}} \begin{pmatrix} 0 \\ v + H(x) \end{pmatrix} \tag{1.26}$$

where $H(x)$ is the Higgs field. This equation gives

$$\begin{aligned}(D^\mu\Phi)^\dagger(D_\mu\Phi) = & \underbrace{\frac{1}{2}(\partial^\mu H)(\partial_\mu H)}_{\text{kinetic energy term of the Higgs field}} + \underbrace{\frac{1}{4}g_2^2 W^-_\mu W^{+\mu}(v+H)^2}_{\text{interaction term with } W \text{ boson}} \\ & + \underbrace{\frac{1}{4}(g_1^2+g_2^2)Z_\mu Z^\mu (v+H)^2}_{\text{interaction term with } Z \text{ boson}}\end{aligned} \tag{1.27}$$

The masses of the vector bosons can be described as the corresponding coefficients of the quadratic terms of the fields:

$$m_W = \frac{vg_2}{2}, \quad m_Z = \frac{v\sqrt{g_1^2 + g_2^2}}{2}. \tag{1.28}$$

1.1.5 The mass of fermions

The Lagrangian of the fermion mass term can be written as

$$\mathcal{L} = -m_f\bar{\psi}\psi = -m_f(\bar{\psi}_L\psi_R + \bar{\psi}_R\psi_L) \tag{1.29}$$

where ψ_L is the left-handed $SU(2)$ double

$$\psi_L = \begin{pmatrix} u_L \\ d_L \end{pmatrix} \tag{1.30}$$

and ψ_R is the right-handed singlet.

This Lagrangian is not invariant under $SU(2)_L$ gauge transformation. In order to make the Lagrangian gauge invariant, the interactions between the Higgs boson and the fermions are introduced. These terms are called Yukawa couplings. The Lagrangian can be written as

$$\begin{aligned} \mathcal{L}^f_{\text{Yukawa}} &= -\frac{\lambda_f}{\sqrt{2}}(v+H)\bar{\psi}_L\psi_R - \frac{\lambda_f}{\sqrt{2}}(v+H)\bar{\psi}_R\psi_L \\ &= \underbrace{-\frac{\lambda_f v}{\sqrt{2}}(\bar{\psi}_L\psi_R + \bar{\psi}_R\psi_L)}_{\text{fermion mass term}} \underbrace{-\frac{\lambda_f}{\sqrt{2}}H(\bar{\psi}_L\psi_R + \bar{\psi}_R\psi_L)}_{\text{interaction term}} \end{aligned}$$

The corresponding coefficient gives mass to each of the fermions:

$$m_f = \frac{\lambda_f v}{\sqrt{2}}. \tag{1.31}$$

where λ_f are Yukawa couplings for each of the fermions. This term indicates that the masses of the fermions are generated from the couplings to the Higgs field. The second term, the interaction term, indicates that the couping strength between the fermions and the Higgs boson g_{Hff} is proportional to the masses of the each of the fermions:

$$g_{Hff} = \frac{m_f}{v}. \tag{1.32}$$

The masses for quarks are also described in the same way. The introduction of the Yukawa coupling is necessary to explain the experimental observations of fermion masses, however, there is no mechanism in SM to determine this Yukawa couping, which is left as a free parameter in SM. For this reason, it is particularly interestring to study the coupling between the Higgs boson and fermions.

1.1.6 Precise measurement of Higgs boson and the Beyond the Standard Model

SM is an effective theory that can describe a lot of phenomena at the low energy region ($\mathcal{O}(100)$ GeV). However, there are still a number of phenomena, such as

gravity, neutrino mass, dark matter, and dark energy, that cannot be explained within the framework of SM. Therefore, it is obviously clear that a new theory, Beyond the Standard Model (BSM), is needed to describe these phenomena.

As described previous section, the couplings of matter fermions and gauge bosons to the Higgs boson are proportional to the masses of the particles in the SM. If there is a new physics beyond the SM, these coupling constants can be deviated from the SM predictions, and the Higgs potential is unique for the SM, so the verification of these two things are crucial to the search of BSM physics.

In addition, the pattern of deviations from the SM expectation of coupling between SM particles and Higgs is possible to give an indication of how the Higgs sector should be extended, such as Supersymmetry model, Composite Higgs model, and so on. These deviations are predicted to be small. Therefore, the precise measurements of the Higgs properties are crucial. Figures.1.4 show an examples of deviation patterns predicted by each model and the power of the ILC precision to distinguish different models of BSM [10].

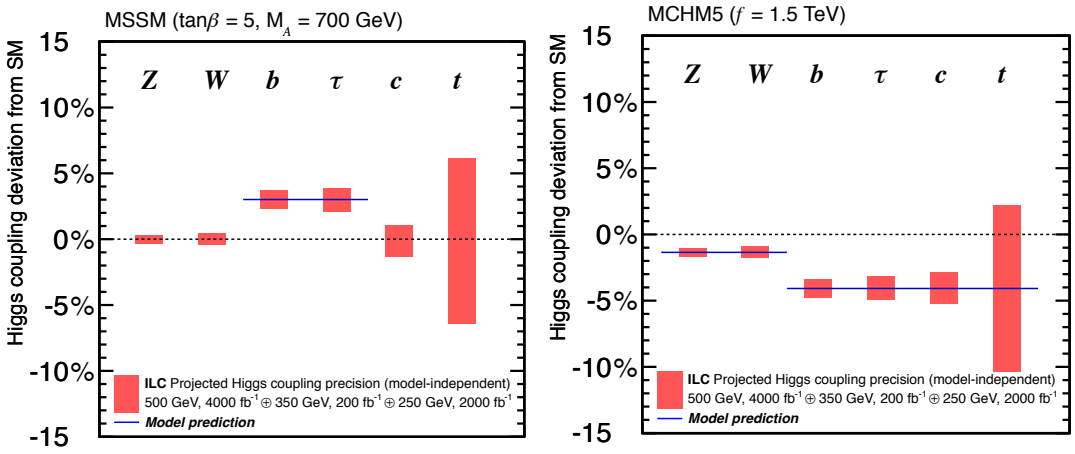

Figure 1.4: The deviation patterns of the Higgs couplings at ILC. (Left) A supersymmetric model. (Right) A composite Higgs model.

1.1.7 Physics beyond the Standard Model

Thanks to the low background in the ILC compared to the LHC because of collisions between elementary particles and the fully reconstructed final state environment, the study of final states in fermion pairs has excellent sensitivity to a wide range of phenomena, and is a strong test for several theories beyond the SM. While LHC directly finds new particles, ILC can indirectly indicate the existence of new particles by observing the deviation from the Standard Model caused by heavy particles, such as heavy spin-1 gauge boson Z'.

The Z' boson is a new neutral gauge boson that couples to fermions in the SM and appears in extended gauge group models as a heavy gauge boson corresponding to $U(1)$ symmetry, and appears as a resonance in the invariant mass spectrum of the lepton pair. There are several models that propose the Z' boson, all inspired by grand unified theory. Deviations from the SM can be tested for the Kaluza-Klein mass scale up to 15 TeV in the early stage of ILC.

Seqential Standard Model (SSM)

In the SSM model [11], the coupling constant of Z' to fermions is the same as the gauge boson Z in the standard theory.

Alternative Left-Right symmetric model (ALR)

The ALR model [11] is a minimal extension of the SM gauge symmetry, derived from the $E6$ model, in which $SU(2)_R$ is added to SM $SU(2)_L$:

$$SU(3) \times SU(2) \times U(1) \times SU(2)_R \tag{1.33}$$

The $E6$ model

The $E6$ model [11, 12, 13] is on the special $U(1)$ that arises by decomposing $E6$ into

$$E6 \rightarrow SO(10) \times U(1)_\Psi \rightarrow SU(5) \times U(1)_\chi \times U(1)_\Psi \rightarrow SM \times U(1)_\beta \tag{1.34}$$

The Z' is represented by a linear combination of two special $U(1)$ gauge bosons.

$$Z' = Z_\chi \cos\beta + Z_\Psi \sin\beta \tag{1.35}$$

where β is the mixing angle defining the spontaneous breaking of $E6$. Depending on the specific value of each β, $\beta = 0$, $\beta = \frac{\pi}{2}$, $\beta = -\arctan\sqrt{\frac{5}{3}}$, different scenarios Z'_χ, Z'_ψ, and Z'_η can be defined, respectively.

The Gauge-Higgs Unification Model (GHU)

One of the fundamental problem of the SM is that there is no principle that regulates the Higgs interactions. One answer to this problems is the Gauge-Higgs Unification model [14]. In the Gauge-Higgs Unification model (GHU), Higgs boson is a part of extra-dimensional components of the gauge potential and appears as a fluctuation mode of Aharonov-Bohm (AB) phase θ_H in the fifth-dimension. The relevant parameter for SM is the θ_H

The Gauge-Higgs Unification model predicts that the Z' boson can be identified as the Kaluza-Klein (KK) excited neutral vector bosons (γ, Z, Z_R). Figure. 1.5 shows the tau polarisation and cross-section as a function of centre-of-mass energy on SM and Gauge-Higgs Unification model with polarised and unpolarised beam. For the cross-section only, large deviation from SM can be observed at > 1 TeV. However, for the tau polarisation, large deviation can be observed even in ILC-250.

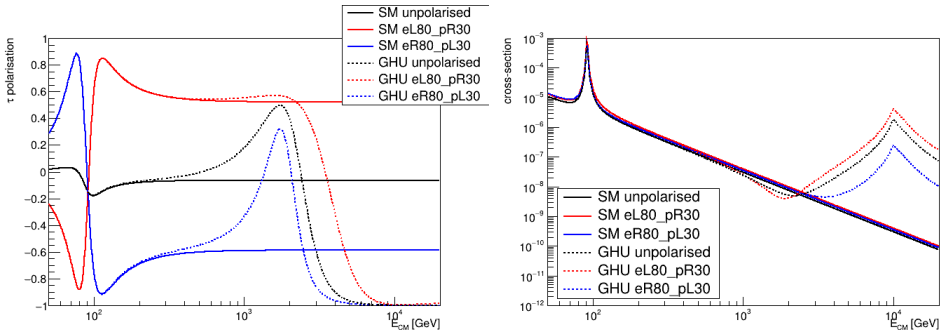

Figure 1.5: Tau polarisation (Left) and Cross-section (Right) on SM and Gauge-Higgs Unification model with polarised and unpolarised beam as a function of the centre-of-mass energy.

CHAPTER 2

INTERNATIONAL LINEAR COLLIDER PROJECT

Contents

2.1 Introduction

The most exciting subject at the energy frontier of experimental high energy particle physics is the detailed investigation of the Higgs boson's properties. As explained in the previous chapter, physics beyond the currently directly-probed energy scale is expected to leave its imprints on the properties of the Higgs, so the Higgs can be used to probe the nature of this new physics.

The Higgs boson was discovered at the Large Hadron Collider (LHC) (a proton-proton collider at 14 TeV), which continues to operate, making Higgs measurments with ever-increasing precision. The forthcoming luminosity upgrade to HL-LHC will provide further significant improvements in our understanding of the Higgs boson. After this experimental program, Higgs couplings

to other SM particles will typically be measured to the several-% level. Such precision will be able to confirm the general pattern of Higgs coupling strengths, e.g. that the coupling is proportional to the particle mass, but is not sufficient to resolve the small, typically %-level, variations in couplings expected to be induced via the virtual effects by new physics at the TeV-scale or higher. To probe the Higgs boson with the precision required to probe such effects requires a new experimental approach.

A collider of leptons has certain advantages over a proton collider such as LHC for precision measurements. The elementary nature of the initial state particles provides hard collisions with rather uniform initial conditions, in contrast to the extraction of partons from a certain Distribution Function within the composite proton. The absence of strong interactions between the inital particles reduces the total interaction cross-section by many orders of magnitude, so "signal" events in which the Higgs boson is produced via electro-weak interactions make up a reasonable fraction of all hard interactions; it also essentially removes the effect of pile-up interactions, in which several paricles from the same bunches collide.

Several electron-positron colliders are being proposed to enable high-precision measurements of the Higgs boson, all of which make use of the "Higgs-strahlung" process $e^+e^- \to HZ$, whose cross-section is maximised at a centre-of mass energy of $\sim$250 GeV. The ILC, CLIC [15] and CCC projects [16] propose a collider consisting of linear accelerators, using different technologies to accelerate the beams; on the other hand the FCC [17] and CEPC projects [18, 19] propose large circular electron-positron colliders. The collider geometry (linear or circular) has a significant effect on the luminosity available at different centre-of-mass energies. Assuming similar power consumption, the above proposals give similar luminosity at the optimal Higgs-strahlung energy of 240$\sim$250 GeV. The luminosity of circular colliders depends strongly on energy, being much higher at lower energies, such as at the Z-pole 91 GeV, but limited at higher energies due to synchrotron radiation losses. The luminosity of linear colliders, on the other hand, tends to rise rather slowly with increasing energy.

Linear colliders in addition allow the use of longitudinally polarised beams, providing initial particles which are dominantly left- or right-handed. Given the maximal parity violation of electro-weak physics, this provides an important additonal tool to probe the structure of many interactions.

The different "Higgs Factory" collider options listed above have similar potential to measure Higgs boson physics at the Higgs-strahlung threshold; where they differ is in the remainder of their physics program: either extremely high luminosity running at lower energies, or the possibility to directly produce electron-positron collisions at higher energies of 1 TeV or above.

2.2 ILC

The International Linear Collider (ILC) is a future linear electron-positron collider that will begin operation as a Higgs factory (ILC250) at a center-of-mass energy of 250 GeV. Its two linear accelerators are based on Superconducting Radio Frequency (SCRF) technology, which can provide an accelerating gradient of $\sim$ 35 MV/m. Both electron and positron beams are polarised, to 80% and

30% respectively.

The ILC is conceived as a staged project starting at 250 GeV, and designed to be upgraded in both luminosity and energy. A luminosity ugrade would involve the installation of more RF power to accelerate the beams, while an energy upgrade involves the lengthening of the the accelerator tunnels and installation of additional accelerating structures, potentially using an improved technology with higher accelerating gradient. Upgrades to 1 TeV or higher are envisioned after the conclusion of the lower-energy stages. A baseline running scenario has 2 ab^{-1} delivered at 250 GeV, 0.2 ab^{-1} at 350 GeV, and 4 ab^{-1} at 500 GeV. The main focus of the 250 GeV run is the Higgs-strahlung process, at 350 GeV a scan of the top quark pair threshold, and at 500 GeV (or better 550 GeV) Higgs–top quark and double Higgs production. This luminosity is split among different combinations of the beam polarisations.

Figure. 2.1 shows a schematic image of the ILC [20].

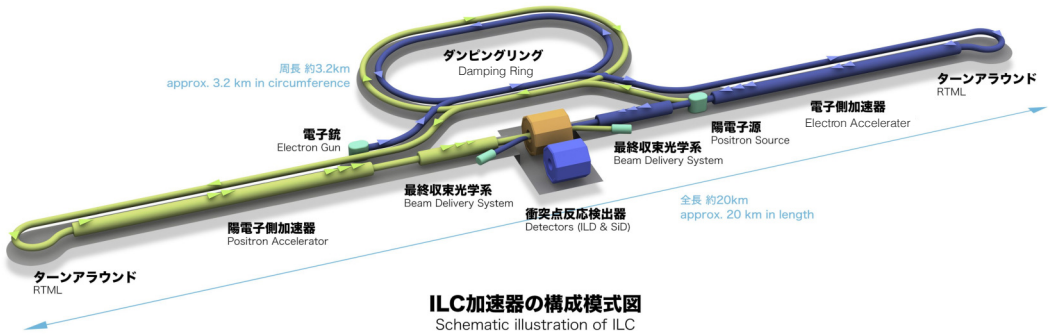

Figure 2.1: Schematic image of the ILC

A strained GaAs/GaAsP photocathode illuminated with circularly polarised laser light produced a beam of polarised electrons, which are collected, collimated and bunched into a small phase-space region within the damping ring at 5 GeV. They are then transferred to the end of the electron linear accelerator, within which they are accelerated to 125 GeV in niobium superconducting RF cavities operating at a frequency of 1.3 GHz and accelerating gradient of 35 MV/m. Every second bunch of high energy electrons is used to create polarised positrons: the bunch is passed through a helical undulator, which produces circularly polarised X-rays. These are then converted in a tungsten target, and the emitted positrons collected. The positrons are collected within the damping rings, before being passed to the positron linear acclelerator and accelerated to the nominal beam energy. The beam bunches are focussed to nanometer size in the Beam Delivery System before colliding at the Interaction Point. Detectors installed at the IP record the collisions.

Basic ILC machine parameters at the different energy points are presented in Tab. 2.1 [21].

Name		Unit	Baseline 500 GeV machine			1st stage	L upgrade	E_{CM} upgrade	
								A	B
Center-of-mass energy	E_{CM}	GeV	250	350	500	250	500	1000	1000
Collision rate	f_{rep}	Hz	5	5	5	5	5	4	4
Number of bunches	N_{b}		1312	1312	1312	1312	2625	2450	2450
Bunch population	N	$\times 10^{10}$	2.0	2.0	2.0	2.0	2.0	1.74	1.74
Bunch separation	Δt_{b}	ns	554	554	554	554	366	366	366
Pulse current	I_{bram}	mA	5.8	5.8	5.8	5.8	8.8	7.6	7.6
Main linac average gradient	G_{a}	MV/m	14.7	21.4	31.5	31.5	31.5	38.2	38.2
Average total beam power	P_{mean}	MW	5.9	7.3	10.5	5.9	21.0	27.2	27.2
Estimated AC power	P_{AC}	MW	122	121	163	129	204	300	300
RMS bunch length	σ_z	mm	0.3	0.3	0.3	0.3	0.3	0.250	0.225
Electron RMS energy spread	$\Delta p/p$	%	0.190	0.158	0.124	0.190	0.124	0.083	0.085
Positron RMS energy spread	$\Delta p/p$	%	0.152	0.100	0.070	0.152	0.070	0.043	0.047
Electron polarization	P_-	%	80	80	80	80	80	80	80
Positron polarization	P_+	%	30	30	30	30	30	20	20
Horizontal emittance	$\gamma\varepsilon_x$	μm	10	10	10	10	10	10	10
Vertical emittance	$\gamma\varepsilon_y$	nm	35	35	35	35	35	30	30
IP horizontal beta function	β_x^*	mm	13.0	16.0	11.0	13.0	11.0	22.6	11.0
IP vertical beta function	β_y^*	mm	0.41	0.34	0.48	0.41	0.48	0.25	0.33
IP RMS horizontal beam axis	σ_x^*	nm	729.0	683.5	474	729	474	481	335
IP RMS vertical beam axis	σ_x^*	nm	7.7	5.9	5.9	7.7	5.9	2.8	2.7
Luminosity	L	$\times 10^{34}\mathrm{cm}^{-2}\mathrm{s}^{-1}$	0.75	1.0	1.8	0.75	3.6	3.6	4.9
Fraction of luminosity in top 1%	$L_{0.01}/L$		87.1%	77.4%	58.3%	87.1%	58.3%	59.2%	44.5%
Average energy loss	δ_{BS}		0.97%	1.9%	4.5%	0.97%	4.5%	5.6%	10.5%
Number of pairs per bunch crossing	N_{pairs}	$\times 10^3$	62.4	93.6	139.0	62.4	139.0	200.5	382.6
Total pair energy per bunch crossing	E_{pairs}	TeV	46.5	115.0	344.1	46.5	344.1	1338.0	3441.0

Table 2.1: ILC basic machine parameters

The ILC beam structure is shown in Figure 2.2. A single train consists of 1312 bunches each separated by 554 ns, and is repeated at 5 Hz.

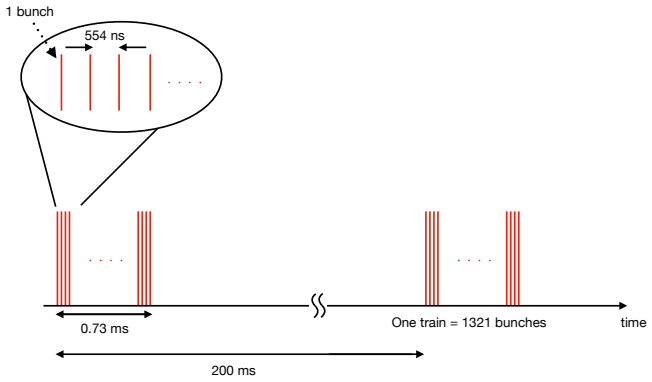

Figure 2.2: Bunch structure of ILC

2.3 ILC detectors

The ILC is designed with a so-called push-pull system, which allows two detectors to share a single collision point. Detectors are mounted on movable platforms which allow one detector to be moved onto the collision point, and the other moved out into a maintainence position. This will allow two experimental groups to profit from the data produced at ILC. Two detector concepts are currently being developed for the ILC: the International Large Detector (ILD) and the Silicon Detector (SiD), shown in Fig. 2.3 [21]. The Japanese group is mainly involved in the development of the ILD, which is the focus of this thesis.

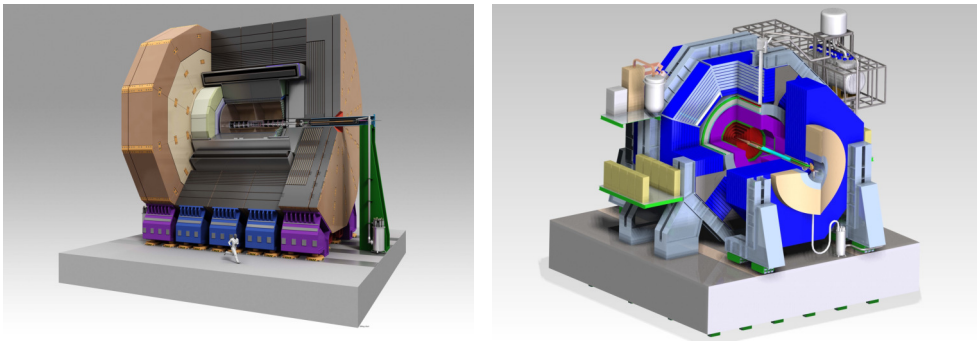

Figure 2.3: Schematic image of detector concepts ILD (left) and SiD (right)

2.4 International Large Detector

ILD is designed as a general-purpose detector to fully harvest the physics potential of the ILC. Consideration of the various expected physics processes have lead to the requirements which inform its design.

Momentum resolution

The Higgs-strahlung process $e^+e^- \to HZ$ has the great advantage that, thanks to the well-known initial four-momentum – the presence of a Higgs boson can be inferred by measuring the Z boson four-momentum and computing the mass recoiling against it. The precision on this "recoil mass" depends on two factors: the initial beam energy spread and the precision with which the Z is measured. The most sensitive channel is $Z \to \mu^+\mu^-$, in which the experimental precision depends on the tracker momentum resolution. The required momentum resolution of the ILD was chosen so as to give similar contributions to the "recoil mass" resolution from these two effects: it results in a transverse momentum resolution requirement of $\delta p_T/p_T \sim 3 \times 10^{-5} p_T[GeV]$.

Jet Energy measurement

Many of the final states to be measured at ILC involve the decays of intermediate bosons W, Z, H. Their dominant decay mode is into quarks which further hadronise into systems of hadronic jets. The ability to distinguish the hadronic decays of on-shell W and Z bosons is a major aim of ILC detectors. ILD has chosen to use the "Particle Flow Analysis" (PFA) approach to jet reconstruction to achieve this goal. PFA is a method that identifies each particle in a jet and measures the momentum and energy of each type of particle with the most appropriate instrument. Electromagnetic calorimeters measure the energy of photons, and neutral hadrons measure their energy with electromagnetic calorimeters and hadron calorimeters. Since charged particles are measured by the calorimeter, clusters are separated and the energy of the charged particle clusters is not used in the jet energy reconstruction, so the PFA must accurately separate the charged particle showers in the calorimeter. Thus, by measuring the particle energy of each final state with the appropriate sub-detector, sufficient jet energy resolution can be achieved to reconstruct and distinguish between the W, Z, and Higgs particles decaying into the jet and their invariant masses.

Vertex performance

The identification of the relatively long-lived hadrons produced in heavy quark decays require a very precise vertexing system, which can identify the production vertices of stated decaying just 10s of microns from the main interaction point. The ability to tag charmed hadron decays is significantly more challenging than b-quark decays, and is therefore a good aim for detector design.

Hermeticity

To identify physics signatures with a missing momentum signature, excellent coverage of the solid angle around the interaction point is needed. The design of individual parts of the detector are designed to avoid dead regions through which a particle could escape detection, and special emphasis has been put to the forward regions of the detector to ensure maximal coverage.

Particle identification

In general, a detector for ILC should be able to identify and measure the direction and energy of the wide range of particles produced in ILC collisions. It should have excellent ability to distinguish electrons from muons from charged hadrons, and photons from neutral hadrons. The ability to separate different hadrons (pions, kaons, protons) would be an added advantage.

2.4.1 ILD design

The cross-sectional view of the ILD shown in Fig. 2.4 [21]. It has a radius of ~ 8 m and a total length of ~ 14 m. A superconducting solenoid with an inner diameter of ~ 3.5 m and a length of ~ 4 m can generate a 3.5 T magnetic field.

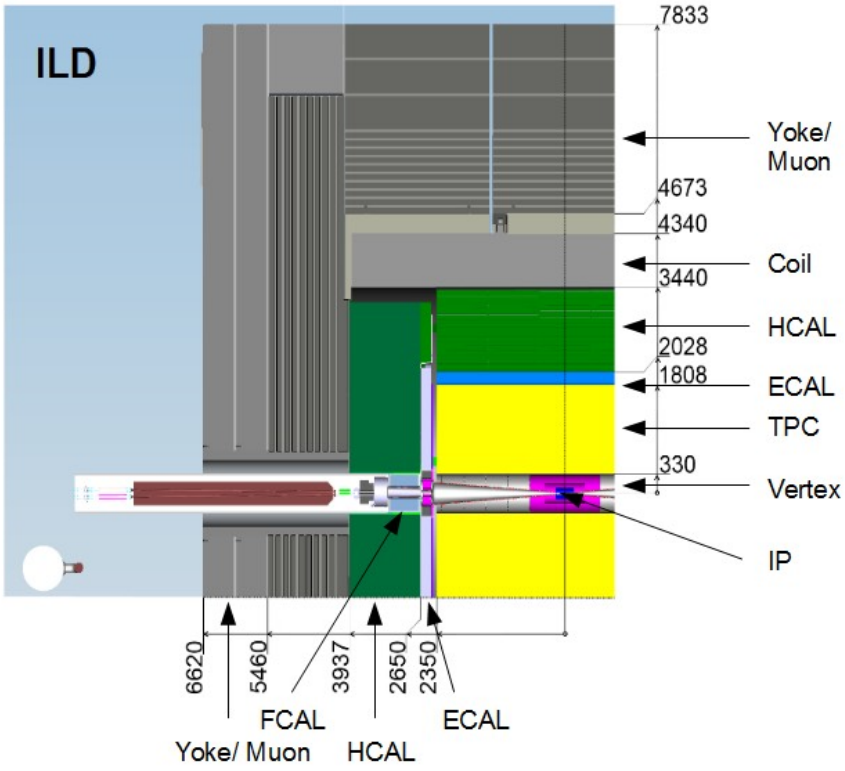

Figure 2.4: Cross-sectional view of the ILD

We next briefly describe the various sub-detectors which make up the ILD.

2.4.2 Vertex detector

The vertex detector is the innermost, multi-layered pixel detector in the ILD for measuring precise vertex information, with an array of pixel sensors [21]. When a particle with a lifetime measurable by the vertex detector, the charged tracks from this particle decay are displaced from the nominal interaction point. By reconstructing the tracks of those decay products, the decay vertex is reconstructed. This is accomplished by measuring very precisely the track parameters

of the charged particles near the interaction point, to enable the identification of heavy quarks (charms and bottoms) and tau leptons.

The performance goal of the ILD vertexing system is to achieve a track impact parameter resolution, the minimum distance from a track to the beam axis, $\sigma > 5 \oplus \frac{10}{p \sin^{\frac{3}{2}} \theta} \mu m$. To meet these specifications, the vertex detector is designed with three double-layers of silicon pixel sensors, placed $\sim 17, 40, 60\ mm$ from the beamline. A single-hit spatial resolution of 3 μm satisfies the requirements. To accomodate the shape of the beam-pipe, the inner-most double layer is a little shorter than the others. Special emphasis is put on a low-mass design which minimises the effect of multiple scattering on low-momentum particles.

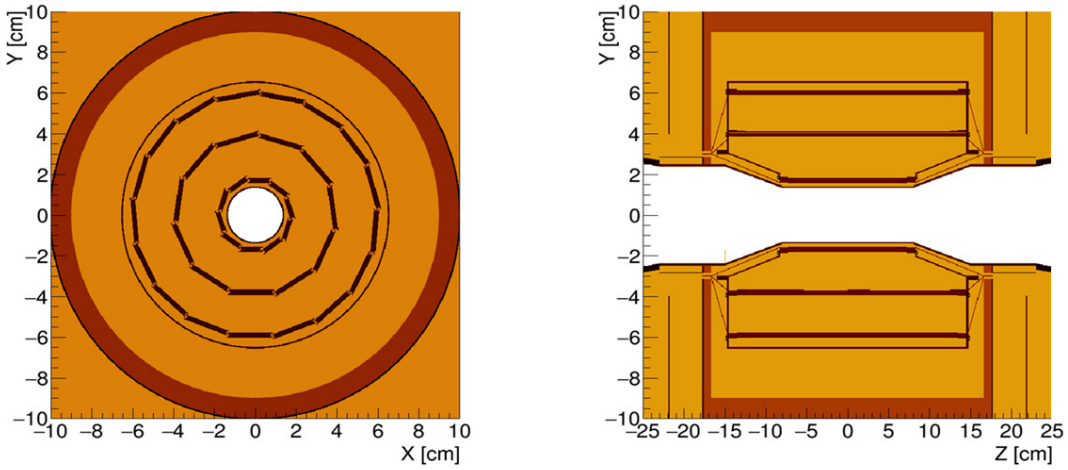

Figure 2.5: Layout of the vertex detector

2.4.3 Silicon trackers

The vertex detector is complemented by additional silicon tracking detectors, shown in Fig. 2.6 [21]. The Silicon Intermediate Tracker (SIT) consists of two silicon tracker layers in the barrel region, which serve to link the main TPC tracker to the vertex detector.

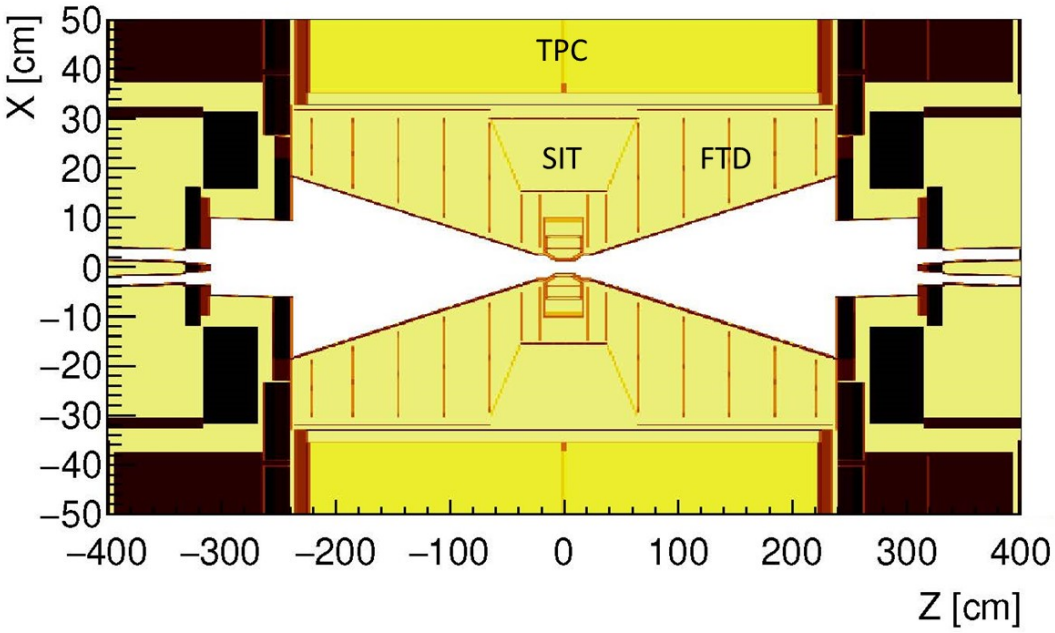

Figure 2.6: Layout of the silicon trackers

The Forward Tracker Disks (FTD) extend the silicon tracker coverage in the forward region. It consists of seven silicon pixel/strip sensors on each side of the IP, filling the gap between the conical beam pipe and inner radius of the TPC. The inner-most pair of disks are considered a part of the vertex detector system, providing precise track measurements near the IP. A visualisation of the FTD system and beampipe are shown in Fig. 2.7 [21].

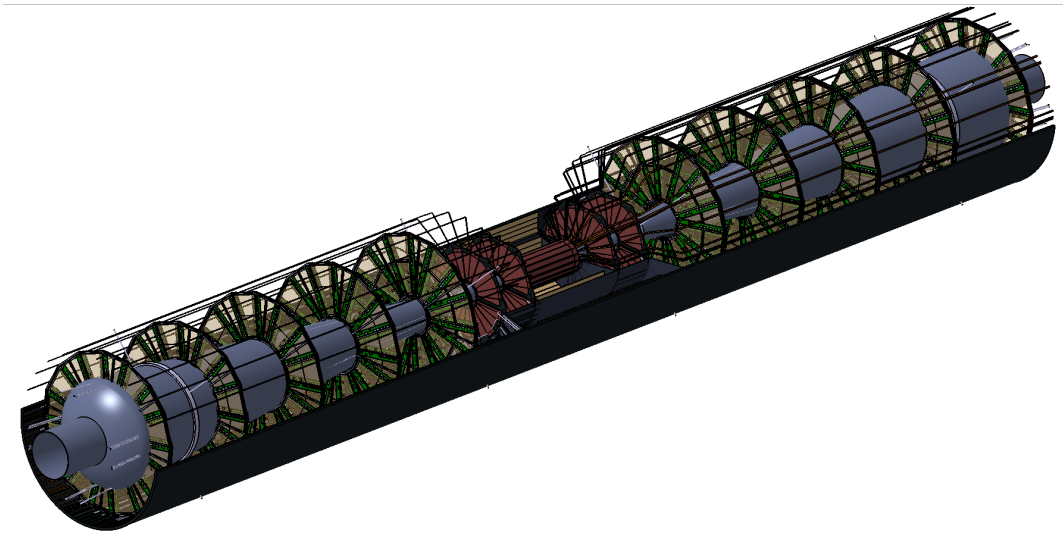

Figure 2.7: Structure of the forward tracking detector system. The beampipe is shown in light grey and the suppot cylinder in dark grey. Seven disks are placed on each side of the IP. The inner-most pairs of disks, and the vertex detector, are shown in brown. Cable paths are also shown.

2.4.4 Time Projection Chamber

The Time Projection Chamber (TPC) is the central tracker of the ILD [21]. TPC can measure the momenta of charged particles precisely using up to 224 space points per track. The inside of the TPC is filled with gas, Ar-CF_4-iC_4H_{10} (so-called T2K gas) is used in the ILD. Ionised electrons are produced when charged particles collide with gas molecules as they pass through the TPC. Electric fields and magnetic fields are applied in the axis direction, and it consists mainly of a field cage that forms the electric field and endplates for amplifying and collecting electron signals. For PFA performance, the TPC is required to have a very low material budget and precise momentum resolution of 1×10^{-4} GeV/c at 3.5 T magnetic field.

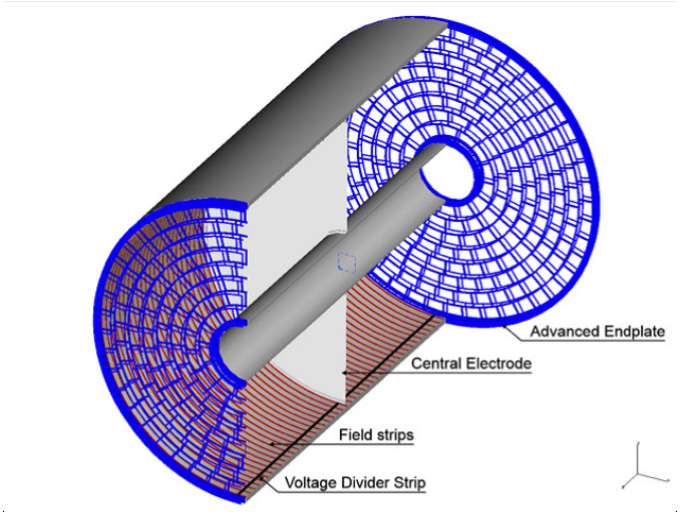

Figure 2.8: Layout of the Time Projection Chamber

2.4.5 Silicon Envelope Tracker

The Silicon Envelope Tracker (SET) is a silicon tracker layer which envelops the outer barrel surface of the TPC. It serves to give a very precise track position measurement at the end of each track. When combined with the precise inner silicon hits and the large number of TPC hits, the required momentum resolution $\delta p_T/p_T \sim 3 \times 10^{-5} p_T[GeV]$ can be attained.

2.4.6 Electromagnetic calorimeter

The electromagnetic calorimeter (ECAL) is a sampling calorimeter installed outside the tracking system to measure the energy of electrons and photons through electro-magnetic shower [21]. It is made by tungsten absorber layer and silicon/scintillator as active layers. The tungsten absorbing layer causes a cascade shower of incident particles. Tungsten has a small radiation length (3.5 mm) and Molière radius (9.3 mm), enabling compact and accurate electromagnetic calorimeters. To achieve an required energy resolution, the ECAL is longitudinally segmented into about 30 layers and the active layers are segmented into cells with a size of 5 to 10 mm in the horizontal direction, which can achieve the pattern recognition performance needed by PFA reconstruction.

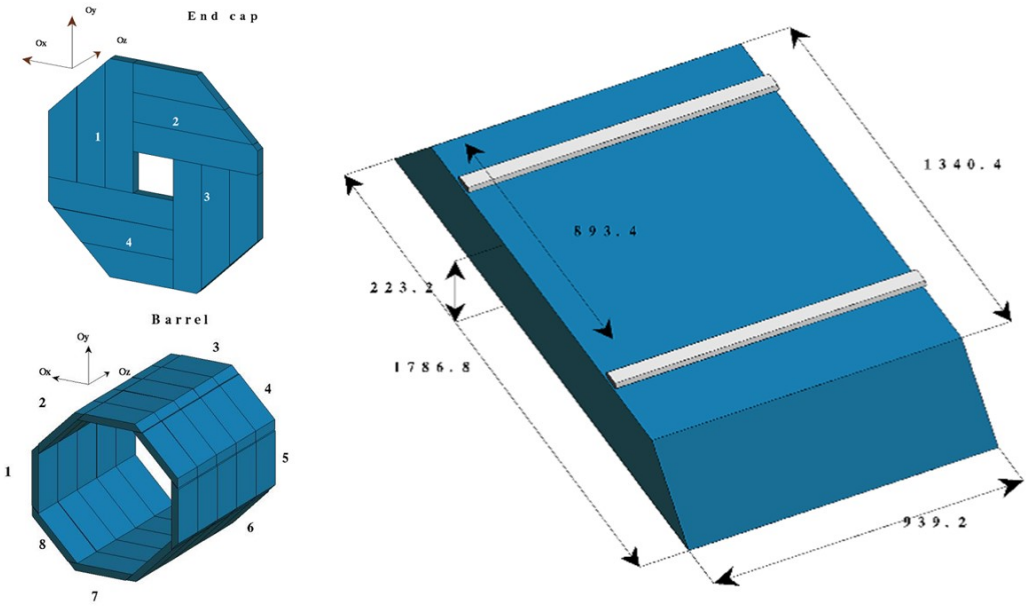

Figure 2.9: General layout of the ECAL. The barrel detector (bottom left) is made of 40 identical modules (right). The structure of an endcap is shown (top left).

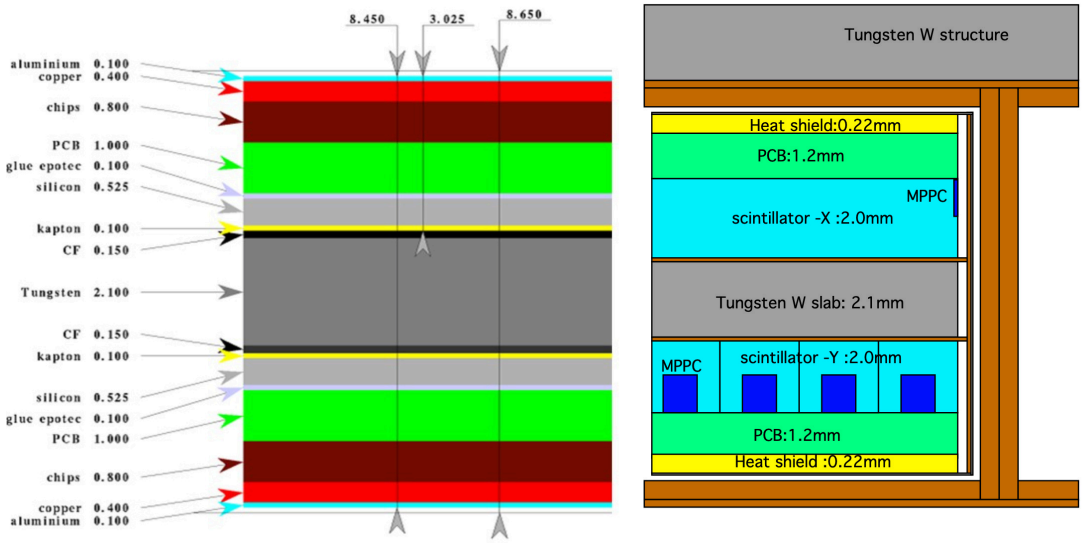

Figure 2.10: Layout of the ECAL sensitive layer for the two technologies being considered for ILD: silicon (left) and scintillator strips (right).

2.4.7 Hadron Calorimeter

The hadron calorimeter (HCAL) is a sampling calorimeter installed outside the ECAL to measure the energy of hadrons through hadronic shower. It is made by 48 sensitive layers with steel absorber and schintillator tiles or gaseous devices as an active medium. HCAL accurately measures the energy of neutral hadrons while separating energy loss between charged and neutral hadrons.

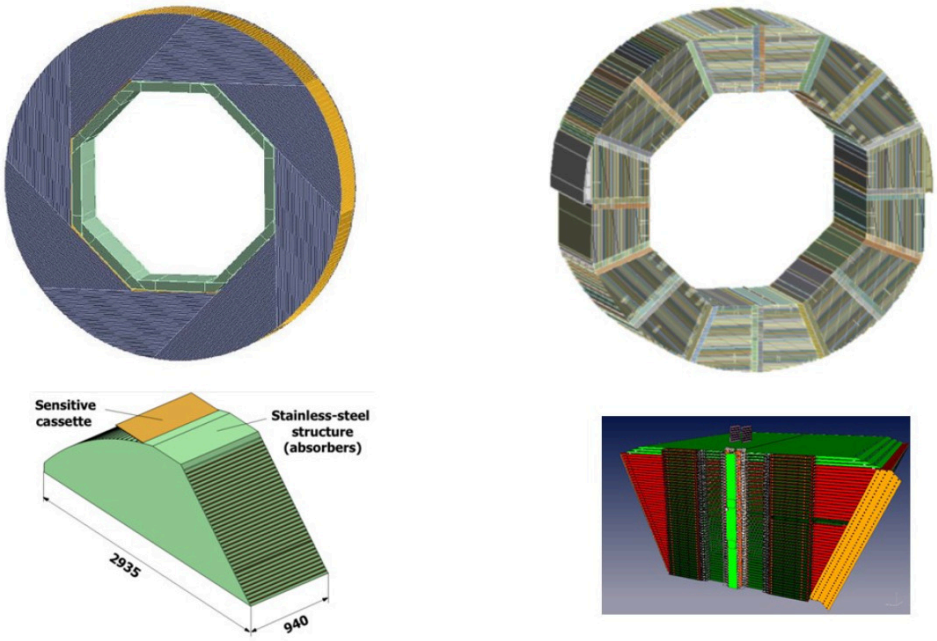

Figure 2.11: General layout of the HCAL. Two different geometrical layouts are proposed (left and right).

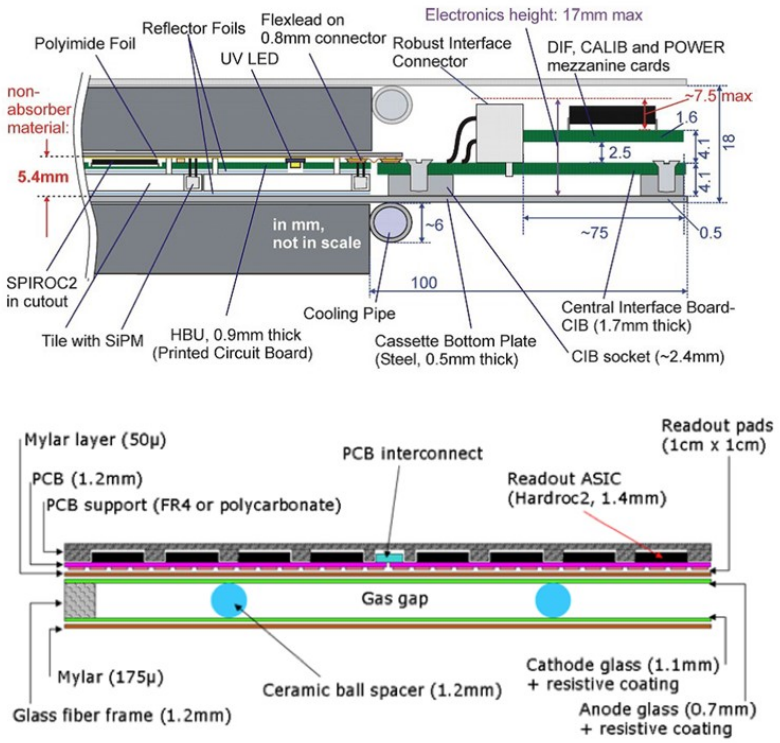

Figure 2.12: Layout of the HCAL sensitive layer, for the scintillator (top) and gaseous RPC (bottom) readout technology options

2.4.8 Forward detectors

The forward detectors – LumiCal, BeamCal and LHCAL – are installed close to the beam axis. Figure. 2.13 shows the layout of the forward detectors [21].

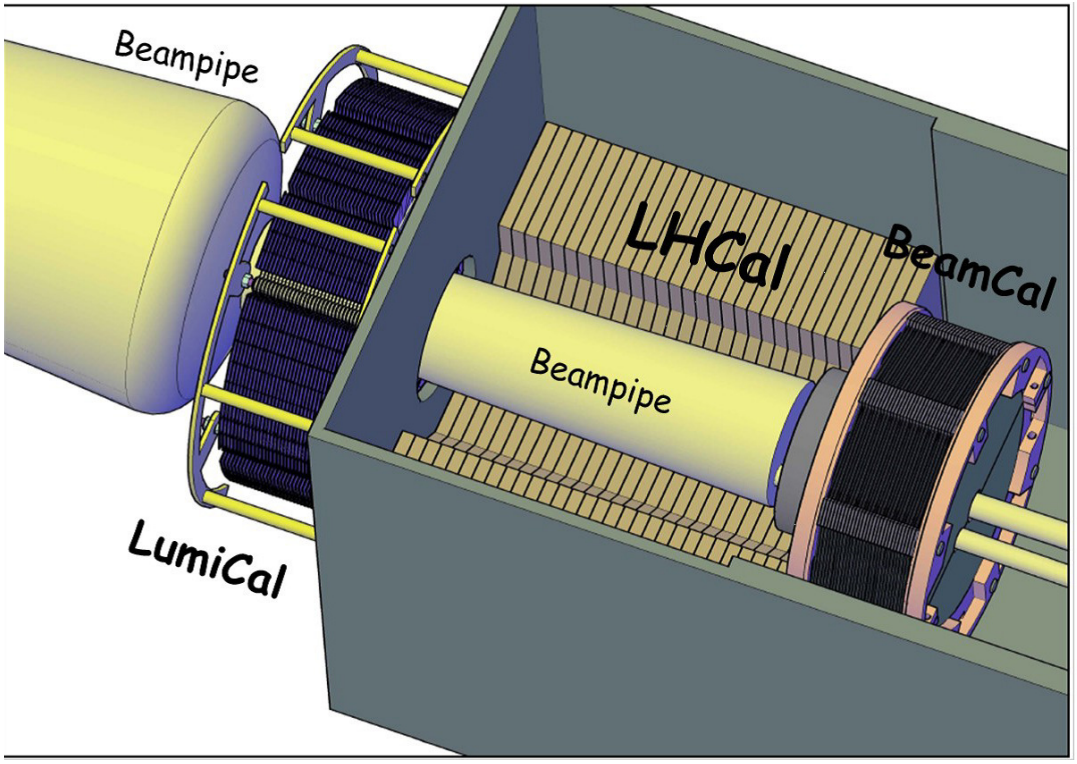

Figure 2.13: Layout of the forward detectors

LumiCal is an electromagnetic calorimeter made of silicon and tungsten. It is positioned around the beam axis and aims to measure luminosity by counting Bhabha scattering, which has an extremely large cross section in electron-positron collisions. A compact readout scheme is needed to provide thin showers which help meet the extremely good understanding of angular acceptance required. The current prototype design is shown in Fig. 2.14 [21].

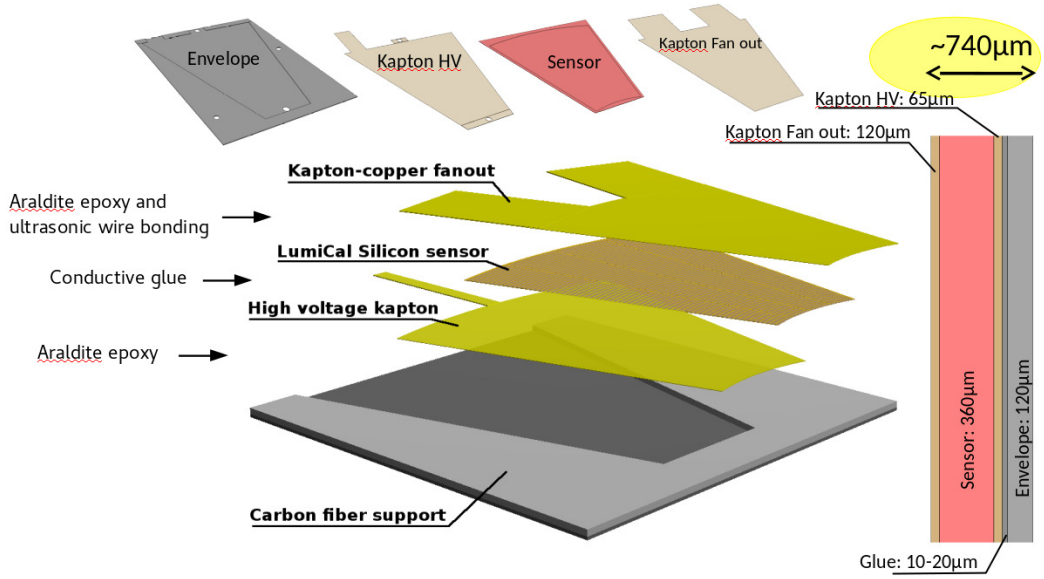

Figure 2.14: Layout of the LumiCAL

The role of the BeamCal and LHCAL is to ensure that calorimeters cover all solid angle in the forward region, with the exception of the in- and out-going beampipes, which each have $\mathcal{O}(cm)$ radius.

2.4.9 The coil, return yoke, and muon system

Both the tracker momentum resolution and Particle Flow performance depend on a strong magnetic field. ILD is designed to have a 3.5 T field produced by a large superconducting solenoid placed outside the calorimeters. The solenoidal field is returned by a thick iron return yoke, dimensioned to reduce the stray field leaking outside the detector (and thereby allowing work on the second detector in the same experimental hall), as shown in Fig. 2.15 [21]. The iron return yoke is instrumented with 10 layers of sensitive detectors (e.g. scintillator bars) which can be used as a muon detection system.

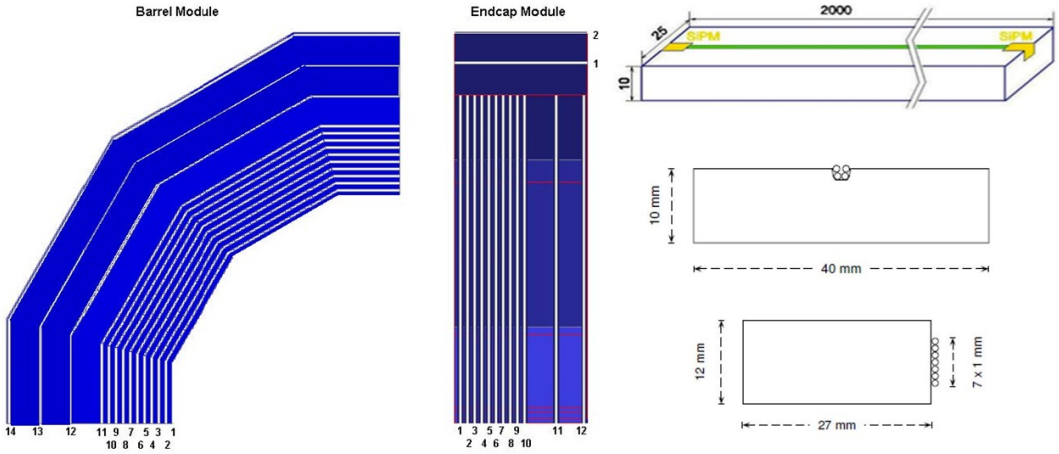

Figure 2.15: Layout of the iron yoke

2.5 ILD performance

This ILD design is implemented in DD4hep software [22], and interfaced to Geant4 [23] to simulate physics events within it. The Geant4 simulation produces collections of "simulated hits" in each sub-detector. These are then digitised to correctly describe the expected properties of the electronics circuits used to collect and record detector signals. The digitised hits are then passed to reconstruction algorithms which identify particle tracks in the tracking detectors, clusters in the calorimeters, and produce an overall reconstruction of the event based on Particle Flow reconstruction, producing a list of final state particles whose parameters are determined by the most appropriate sub-detectors (usually the one providing the most precise measurement).

2.5.1 Particle Flow Analysis

The PandoraPFA algorithm is used to reconstruct particles within an event, as illustrated in Fig. 2.16 [24]. The resulting jet energy resolution is shown in Fig. 2.17 [25]. The figure shows the purely calorimetric resolution in blue, and the results of PFA in the solid black line. PFA resolution is a significant improvement over the calorimeter-only result at all jet energies. At jet energies above 100 GeV the largest contribution to the resolution is the "confusion" term, which is due to calorimeter deposits being mis-assigned to the wrong particle; at smaller jet energies the largest contribution is due to the single-particle calorimeter energy resolution.

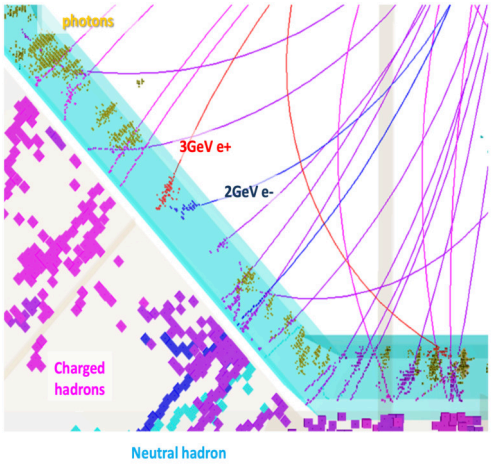

Figure 2.16: A display of a section of an event reconstructed by PFA. Charged particle tracks (lines) impinge on the electromagnetic (cyan) and hadronic (light grey) calorimeters. The PFA reconstruction assigns calormeter hits to clusters, and if appropriate these clusters to charged particle tracks.

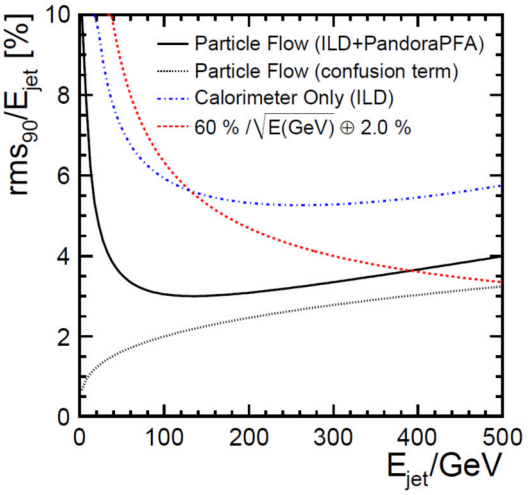

Figure 2.17: Jet Energy Resolution performance of PandoraPFA in ILD.

Part 1

CHAPTER 3

MEASUREMENT OF THE TAU POLARISATION

3.1 Introduction

The fermion–pair production reaction $e^+e^- \to f\overline{f}$ is the simplest process which occurs at an electron-positron collider. In the Standard Model, it proceeds at leading order via s-channel exchange of a photon and Z boson for the charged leptons and quarks; in the case of an electron final state, additional t-channel diagrams contribute. Thanks to its simplicity, its properties can be precisely predicted both within the SM including extensions to describe new physics.

Since the Z couples differently to left- and right-handed fermions, the fermion-pair reaction is different for fermions of different chirality. The precise experimental verification of these chiral couplings to the Z boson is one of the key aspects of the Electro-Weak program at future Higgs-Top-Electroweak–factory colliders such as the ILC. This study of Z couplings can be done either at a dedicated collider run at the Z-pole, or at higher centre-of-mass energies by making use of the "radiative return", in which Initial State Radiation returns the effective centre-of-mass energy to the Z mass.

How to control the chirality of the fermions in the $e^+e^- \to f\overline{f}$ process? In the case of linear colliders such as the ILC, the initial electron and positron beams can be longitudinally polarised: i.e. the majority of beam particles are in a particular helicity state, positive or negative. Since the fermions involved in the $e^+e^- \to f\overline{f}$ process have – with the exception of the top quark – masses much smaller than the $\mathcal{O}(100)$ GeV centre-of-mass energy, the helicity state of a fermion corresponds almost exactly to its chirality under the weak interactions. By using spin-polarised beams, one can therefore enrich the initial colliding beam particles in a particular chiral state. By flipping the polarisation, the contribution of the other chiral state can be enhanced, allowing the chiral couplings to be extracted. Since the initial particles are electrons/positrons, this provides direct measurement of the electron's chiral couplings.

The angular distribution of the final state fermions in this process is determined by the conservation of angular momentum. In the case of polarised beams, there is an average net angular momentum along the z (beam) axis. If left- or right- handed final-state fermions are preferentially produced in the reaction, then a forward-backward asymmetry (A_{FB}) is be introduced: the final state

fermion will more (or less) often be produced in the forward direction, depending on the initial beam polarisation. A measurement of A_{FB} can be combined with the known beam polarisation to extract the Left-Right Asymmetries (A_{LR}) of the electron and final state fermion couplings.

An additional handle is to reconstruct the helicity of the final state fermions. In the case of a collider without longitudinal beam polarisation, as is typical at high-energy circular colliders, this is the only handle on the chiral couplings. The helicity of fermions is not directly measurable, and is accessible via their interactions or decays. At collider experiments, consideration of particle decays is the only viable approach. Electron and muon decays are not registered with the experiments, due to their long decay length, while lighter quarks are either essentially stable (u, d, s) or hadronise before they decay (c, b) thereby greatly complicating the extraction of helicity information. The two remaining fermions, the τ lepton and top quark, do allow the reconstruction of their helicity. The top is produced in very high energy collisions above 350 GeV, while the τ gives access to a very wide range of centre-of-mass energies.

In this chapter we describe the reconstruction of the process $e^+e^- \to \tau^+\tau^-$ at a high-energy electron-positron collider, and the use of the τ decays to measure their polarisation.

3.2 Tau lepton

The tau is the most massive of the SM fermions, at 1.77 GeV, and decays via the weak interaction to a tau neutrino and a virtual W boson with a relatively short lifetime of 2.9×10^{-13} s. The many possible final states of the decay are summarised in Fig. 3.1 [26]. The largest fraction is to $\tau^+ \to \pi^+\pi^0\nu_\tau$ ($\sim 26\%$), followed by the leptonic decays $\tau^+ \to (\mu^+, e^+)\nu_{(\mu,e)}\nu_\tau$ ($\sim 17\%$ each), and the simplest hadronic decay $\tau^+ \to \pi^+\nu_\tau$ ($\sim 11\%$).

The kinematics of τ decay is strongly influenced by the initial τ helicity. This is most easily understood in $\tau^+ \to \pi^+\nu_\tau$, in which the spin-$\frac{1}{2}$ τ decays to a spin-$\frac{1}{2}$ anti-neutrino and a scalar π^+. Since the anti-neutrino must have positive helicity due to the maximal parity violation of the weak interaction, it is preferentially produced in the same direction as the initial τ spin. If the tau has positive helicity, the neutrino tends to be produced along the tau momentum, while if it has negative helicity, the neutrino goes in the opposite direction. In this case, the angle the neutrino (or, equivalently, the pion) momentum makes with the τ momentum direction, defined in the τ rest frame, has optimal sensitivity to the underlying τ helicity. In the case of other hadronic decay modes, more complex functions of final particle momenta in the τ rest frame can give the same sensitivity to the helicity.

We can define "polarimeter vectors", functions of the tau decay products' momenta, which are sensitive to the tau spin orientation. In the case of $\tau \to \pi\nu$ and $\tau \to \rho\nu \to \pi^\pm\pi^0\nu$ decay modes, optimal polarimeters $\mathbf{P}$, which maximise the sensitivity, are

$$\mathbf{P}_\pi = \mathbf{p}_\nu \tag{3.1}$$

$$\mathbf{P}_\rho = 2(\mathbf{q}\cdot\mathbf{p}_\nu)\mathbf{q} - m_q^2\mathbf{p}_\nu \tag{3.2}$$

where $\mathbf{q} = \mathbf{p}_{\pi^\pm} - \mathbf{p}_{\pi^0}$, and $\mathbf{p}_\nu, \mathbf{p}_{\pi^\pm}, \mathbf{p}_{\pi^0}$ are the 3-momenta of the neutrino,

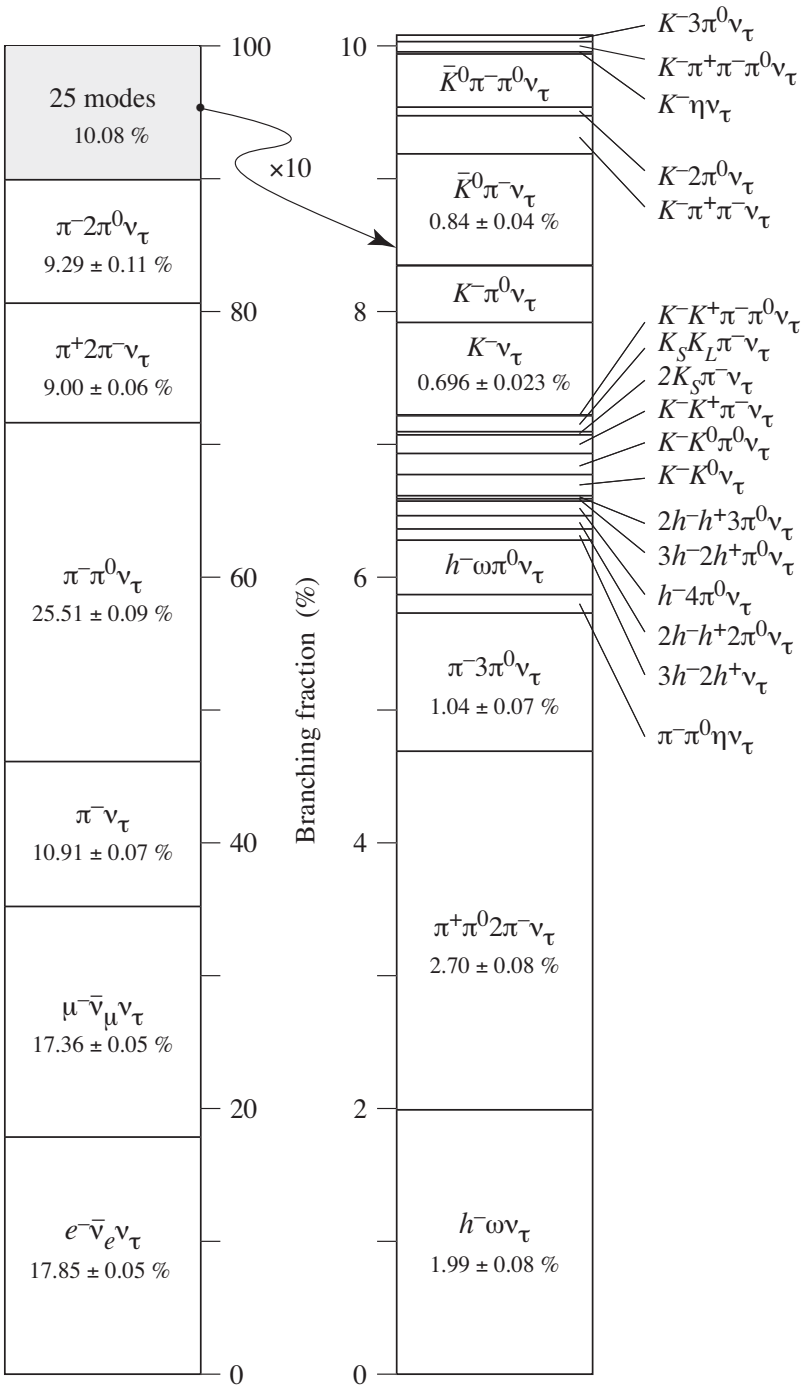

Figure 3.1: Branching fraction of tau lepton.

charged, and neutral pion in the tau lepton rest frame. The cosine of the angle this polarimeter vector makes to the tau momentum direction is the optimal estimator of the tau helicity, which we call the "polarimeter". Example distributions of the polarimeter in these two decay modes, calculated using the MC-truth momenta of tau decays products, are shown in Fig. 3.2.

In the case of fully-leptonic decays, the τ decays to three fermions, two of which cannot be observed. The momentum of the visible lepton does have some sensitivity to the τ helicity, although it is reduced with respect to the hadronic decays. For this reason we do not consider these decays for measurement of the

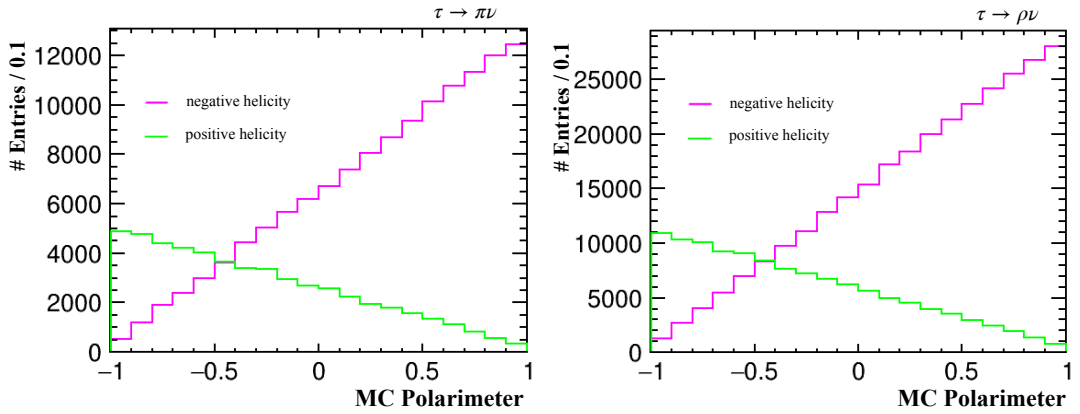

Figure 3.2: MC polarimeter for $\tau \to \pi\nu$ decay (left) and $\tau \to \rho\nu$ decay (right). Distributions for positive (negative) helicity taus are shown in green (magenta).

tau polarisation.

3.3 Tau reconstruction method

As mentioned above, the reconstruction of optimal estimators of the tau helicity requires the knowledge of decay products' momenta in the tau rest frame. In the case of the process $e^+e^- \to \tau^+\tau^-(\gamma)$, the two τ rest frames are not directly reconstructible due to the presence of undetected neutrinos.

In this section we first describe the traditional "cone" method to explicitly reconstruct the tau momenta in the case of back-to-back taus, and the closely related "mid-point" method. We then describe our newly-developed "impact parameter" method which can be applied to a wider range of $\tau^+\tau^-$ kinematics.

We discuss the case of single-prong τ decays, in which a single charged particle is produced in the decay. Multi-prong decays are relatively rare, however they provide additional constraints thanks to the possibility of explicitly reconstructing the tau decay vertex.

3.3.1 Simulation setup

To develop and study the performance of these methods, samples of $e^+e^- \to \tau^+\tau^-$ events were generated using the WHIZARD event generator (version 2.85) [27]. The samples took account of the expected beam energy spread expected at ILC-250 due to the intrinsic accelerator energy spread as well as the spectrum induced by beamstrahlung. Samples were produced with 100% polarised beams, and mixed with appropriate weights to simulate the expected ILC-250 beam polarisations of $\pm 80\%(\mp 30\%)$ for the electron (positron). The effects of initial and final state radiation were included, and the tau leptons were decayed using TAUOLA [28], taking account of their helicities.

3.3.2 Cone method

If we can assume the τ energy E_τ and that the tau has decayed to a single neutrino, then the tau mass constraint can be used to constrain the tau momentum

p_τ to lie at a well-defined angle β to the visible tau momentum p_{vis} on the surface of a cone around the visible tau momentum

$$\cos\beta = \frac{\vec{p}^2_{vis} + |P_{vis}|E_\nu cos\alpha}{|\vec{p}_\tau||\vec{p}_{vis}|}, \tag{3.3}$$

where $\cos\alpha$ is

$$\begin{aligned}\cos\alpha &= \frac{(E_{vis}+E_\nu)^2 - m_\tau^2 - \vec{p}^2_{vis} - E_\nu^2}{2E_\nu|\vec{p}_{vis}|} \\ &= \frac{E_{vis}^2 + 2E_\nu E_{vis} - m_\tau^2 - \vec{p}^2_{vis}}{2E_\nu|\vec{p}_{vis}|}\end{aligned} \tag{3.4}$$

If we consider the reaction $e^+e^- \to \tau^+\tau^-$ in its centre-of-mass frame, and without any initial state radiation, then the two taus have known energy (half the centre-of-mass energy) and are produced back-to-back. The momentum of each tau lies on a cone around its visible momentum. A consistent solution in the event can be found by "flipping" one cone (i.e. reflecting it in the plane normal to its axis and containing the nominal interaction point (IP)), and finding the intersections of the two cones, as illustrated in Fig. 3.3 In the ideal case, these two cones intersect along two (possibly degenerate) directions.

If some of the assumptions are not exactly satisfied (e.g. there is Initial State Radiation (ISR) or Final State Radiation (FSR), or significant beam energy spread) the cones may not intersect, and no solutions can be identified.

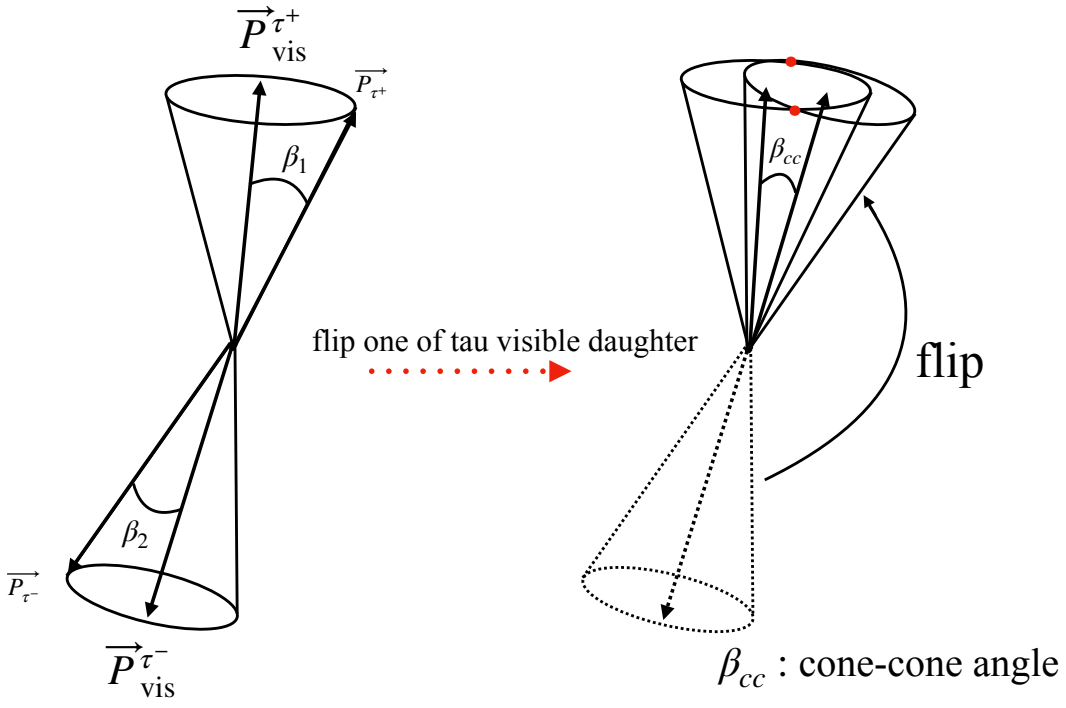

Figure 3.3: Illustration of the "cone" reconstruction method.

To study the efficiency of the method, we first apply it using the MC-truth momenta of visible tau decay products as input. The fraction of events in which the two cones intersect – in other words the efficiency – is shown in Fig. 3.4 as

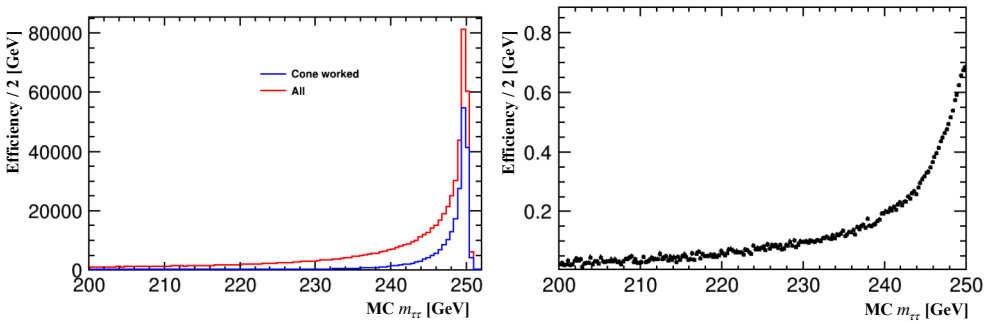

Figure 3.4: Left: distribution of $m_{\tau\tau}$ for all events, and for those in which the cone method found at least one solution. Right: Cone method efficiency as a function of $m_{\tau\tau}$.

a function of the true invariant mass of the tau lepton pair.
The efficiency is $\sim 70\%$ for events with $m_{\tau\tau} \sim 250$ GeV, drops to around 20% by 240 GeV, and falls further at smaller invariant. This is because events with small $m_{\tau\tau}$ must have had significant ISR, which invalidates both the back-to-back and E_τ assumptions.

For events for which "Cone method" cannot find a solution, i.e. the two cones do not intersect, we can define an approximate solution as the vector midway between the two cones at their points of closest approach, as illustrated in Fig. 3.5. We call this "Midpoint method".

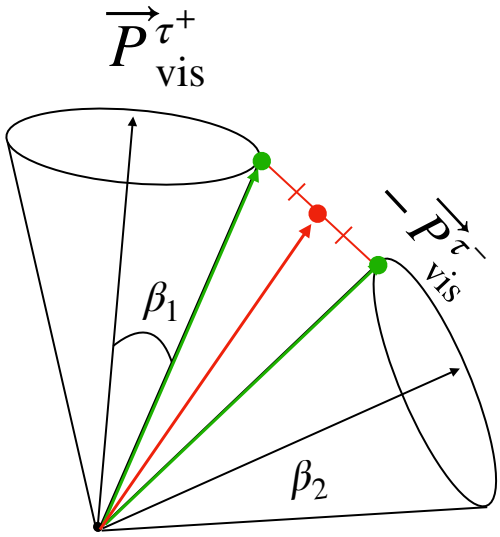

Figure 3.5: Illustration of the "midpoint" method.

Once the tau lepton momenta have been reconstructed, the decay products momenta can be boosted into the tau rest frame, and the polarimeters calculated.

3.3.3 Polarimeter reconstruction

Here we restrict ourselves to events with $m_{\tau\tau} \geq 240\ GeV$ in which at least one of the τ has decayed to either $\pi\nu$ or $\rho\nu$. The cone method gives two possible solutions, which we treat equally. For each solution, we calculate the polarimeter

for each τ which decays into one of the above modes, using the MC-truth momenta of visible particles as input. A comparison between the true polarimeter, which uses the MC τ momentum as an input, and the polarimeter using momenta reconstructed by the cone method, is shown in Fig. 3.6, separately for the two decay modes. The general reconstruction of the polarimeter is quite good, particularly for decays to $\pi\nu$. The ρ decay mode shows some more significant migrations.

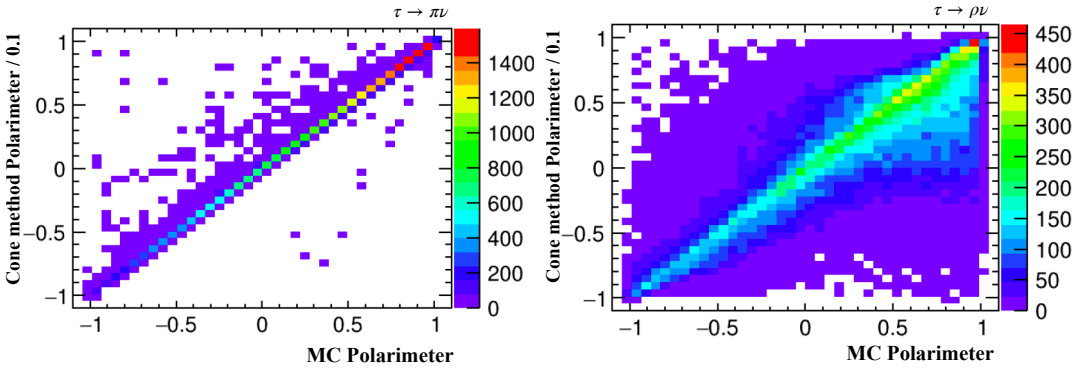

Figure 3.6: Comparison of the polarimeter calculated using the tau momentum reconstructed by the cone method that using the MC-truth tau momentum, for $\tau \to \pi\nu$ (left) and $\tau \to \rho\nu$ decays (right).

Events for which the cone method found no solutions for the tau momenta were passed to the midpoint method. The polarimeters calculated using the results of the mid-point method are compared to the MC-truth polarimeter in Fig. 3.7. The extracted polarimeters are less precise than for the cone method, since the method is used only if the kinematic assumptions are significantly violated, resulting in less accurate reconstruction.

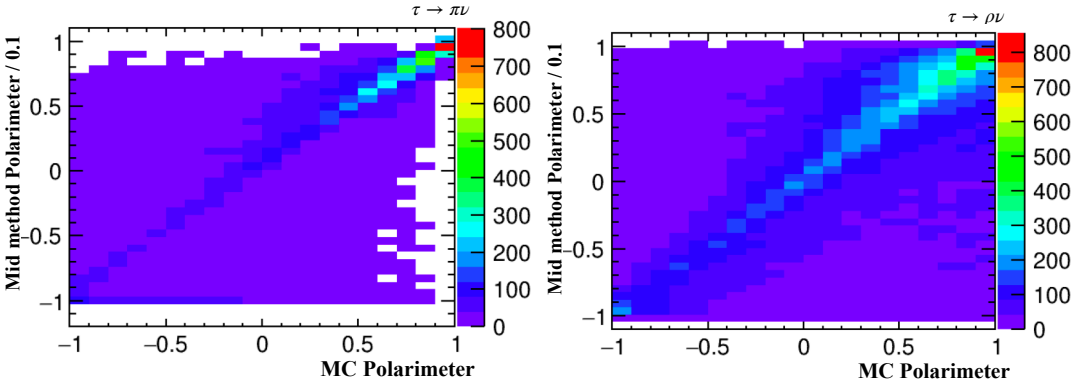

Figure 3.7: Comparison of the polarimeter calculated using the tau momentum reconstructed by the midpoint method that using the MC-truth tau momentum, for $\tau \to \pi\nu$ (left) and $\tau \to \rho\nu$ decays (right).

3.3.4 Impact parameter method

We have seen that the traditional "cone" method has only limited applicability at high energy electron-positron collider experiments, mostly due to the significant probability of initial state radiation which invalidates the assumptions behind the method.

To improve the situation, we have developed a new method to reconstruct di-tau events which removes the troublesome assumptions, replacing them with information which will be available at the future generation of Higgs factories. The key aspects which allow new constraints are the extremely good impact parameter resolution provided by the experiments (at the μm level, significantly smaller than the typical impact parameters of tau decay products), coupled with the "nano-beam" scheme used in the colliders to enhance the luminosity, which ensures that the transverse size of the beam-beam interaction region is small compared to both the tau decay length and the typical impact parameter resolution of the detectors.

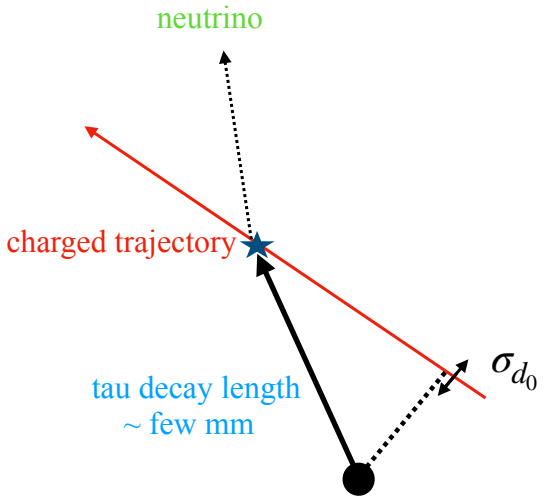

Figure 3.8: Schematic image of the impact parameter in a tau decay.

Collinear ISR

We first assume that the two taus are produced back-to-back in the plane transverse to the beam-line. This assumption allows the presence of ISR, provided that it is collinear with the beam-line, as it indeed dominantly is. We can then define a tau-tau production plane which contains the beamline and both tau momenta, which is oriented at some azimuthal angle ϕ, which is to be determined.

Charged particle trajectories

The charged decay products of the tau lepton are precisely measured by the tracking system of the detector. The vertex detector in particular precisely reconstructs the particle trajectory close to the interaction point. For simplicity we assume that the tau decays to a single charged particle in addition to some number of neutral particles. The intersection of the charged decay product of

the tau with the tau-tau production plane can be calculated. A linear approximation for the trajectory in the vicinity of the IP is appropriate given the typical momenta and magnetic field, which makes the math trivial: Let d be the position of a point on the trajectory of the charged particle with respect to the nominal interaction point (IP), and p the particle momentum at that point. It is convenient to define d as the point of closest approach (PCA) to the IP. Neglecting the track curvature, a general point r on the trajectory close to the PCA can be approximated by

$$r = d + \alpha\hat{p} \tag{3.5}$$

where $\hat{p}$ is a unit vector parallel to p and α a real number. The intersection of the approximated trajectory with a plane containing the z axis at an azimuthal angle ϕ occurs when

$$\tan\phi = \frac{r_y}{r_x} = \frac{d_y + \alpha\hat{p}_y}{d_x + \alpha\hat{p}_x}, \tag{3.6}$$

or when

$$\alpha = \frac{d_y\cos\phi - d_x\sin\phi}{\hat{p}_x\sin\phi - \hat{p}_y\cos\phi} \tag{3.7}$$

This intersection represents the point at which the tau lepton decayed.

Production vertex

The transverse size of the interaction region is very small ($nm \sim \mu m$), so we can assume that the taus are produced at a point somewhere along the nominal beam line, whose position we assume is very precisely known by analysis of the vast majority of events containing promptly produced particles. We cannot directly reconstruct the production position along the beamline so we leave it as a parameter z_{IP} to be determined. [1]

A particular choice of the two parameters ϕ and z_{IP} determines the production and decay vertices of the two taus, and also the direction of their momenta (in the assumption of negligible bending in the experiment's magnetic field within the short tau flight path). This is illustrated in Fig. 3.9.

Energy and momentum conservation and m_τ

Given the two tau directions, we can calculate the tau energies if we make additional assumptions: that the centre-of-mass energy is the nominal one, that any 4-momentum lost to ISR can be modeled as that of a single photon collinear to the beamline, and the tau lepton mass.

The transverse momentum p_T is assumed to be the same for each tau in order to conserve the event's transverse momentum; the magnitude of the total tau momenta are then given by $p_i = p_T/\sin\theta_i$, and the z momenta by $p_{z,i} = p_T/\tan\theta_i$, where θ_i is the polar angle of the tau direction. Conservation of energy gives $E_{\tau,1} + E_{\tau,2} + E_{ISR} = E_{CM}$, where $E_{\tau,1(2)}$ is the energy of tau 1(2), E_{ISR} the energy carried by ISR photons, and E_{CM} is the centre-of-mass energy. Assuming one ISR photon collinear with the beam, momentum conservation in the z directions gives $E_{ISR} = |p_{z,1} + p_{z,2}|$.

[1] We note that a particularly long-lived tau which travels several *cm* before decaying may have its trajectory directly reconstructed within the vertex detector: a very rare case which we do not address here.

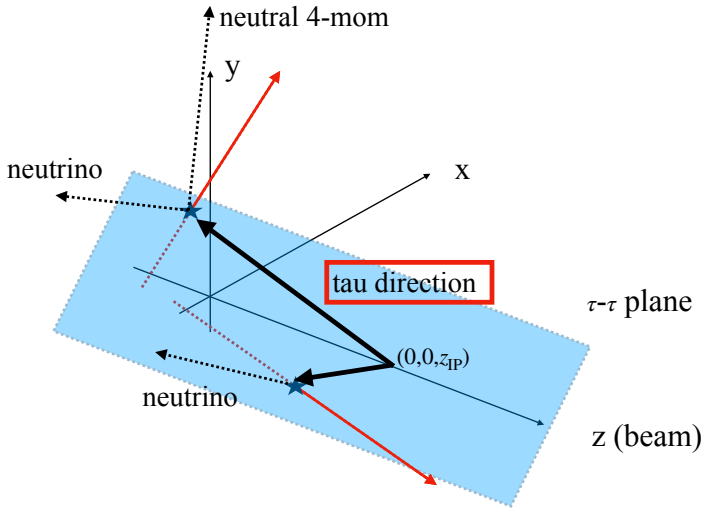

Figure 3.9: Schematic image of calculating tau direction.

We can then write

$$\begin{aligned} E_{CM} &= E_{\tau,1} + E_{\tau,2} + E_{ISR} \\ &= \sqrt{p_1^2 + m_\tau^2} + \sqrt{p_2^2 + m_\tau^2} + |p_{z,1} + p_{z,2}| \\ &\approx p_1 \left[1 + \frac{m_\tau^2}{2p_1^2}\right] + p_2 \left[1 + \frac{m_\tau^2}{2p_2^2}\right] + |p_{z,1} + p_{z,2}| \end{aligned} \tag{3.8}$$

in the limit $p_i \gg m_\tau$. Rewriting in terms of p_T, $\theta_{1,2}$

$$\begin{aligned} 0 \approx\ & p_T^2(|\cot\theta_1 + \cot\theta_2| + \csc\theta_1 + \csc\theta_2) \\ & - p_T E_{CM} \\ & + \frac{1}{2} m_\tau^2 (\sin\theta_1 + \sin\theta_2) \end{aligned} \tag{3.9}$$

which is a quadratic equation in p_T, with solutions

$$\begin{aligned} p_T &\approx \frac{E_{CM}}{2A}\left(1 \pm \sqrt{1 - 4AC\frac{m_\tau^2}{E_{CM}^2}}\right), \\ A &= |\cot\theta_1 + \cot\theta_2| + \csc\theta_1 + \csc\theta_2 \\ C &= \frac{1}{2}(\sin\theta_1 + \sin\theta_2) \end{aligned} \tag{3.10}$$

Since $AC(m_\tau/E_{CM})^2 \sim 10^{-3} \to 10^{-4}$ over the whole range of θ_1, θ_2, we can safely ignore the solution with $p_T \approx 0$ and approximate

$$p_T \approx \frac{E_{CM}}{A}. \tag{3.11}$$

Neutrino mass

We have shown that, given a choice of the two parameters ϕ and z_{IP}, the trajectories of charged tau daughters can be used to calculate the tau 4-momenta and the energy lost to (collinear) ISR. The question is now how to choose the parameters

ϕ and z_{IP}? The measured 4-momenta of the visible tau jets provide additional information. By comparing the calculated tau 4-momentum with the measured visible tau jet 4-momentum, the 4-momentum of the invisible part of the tau decay can be extracted, which should correspond to the 4-momentum carried by the neutrino(s) produced in the decay. Since we are considering hadronic tau decays, it should be consistent with a single neutrino, so the invariant mass of the invisible 4-momentum (the "missing mass") should ideally be zero.

Figure 3.10 shows the result of a scan of the $z_{IP} - \phi$ for a single event. The left (centre) plots show the absolute value of the squared invariant mass of the invisible 4-momentum for the two tau jets. A good solution would be one at which these two lines intersect, and both neutrinos have a mass consistent with zero. To find these, we consider the sum of the squared masses, shown on the right-hand figure. We search for well-separated local minima in this distribution. If such a minimum corresponds to a mass of less than 5.0 GeV, it are considered as a potential event solution.

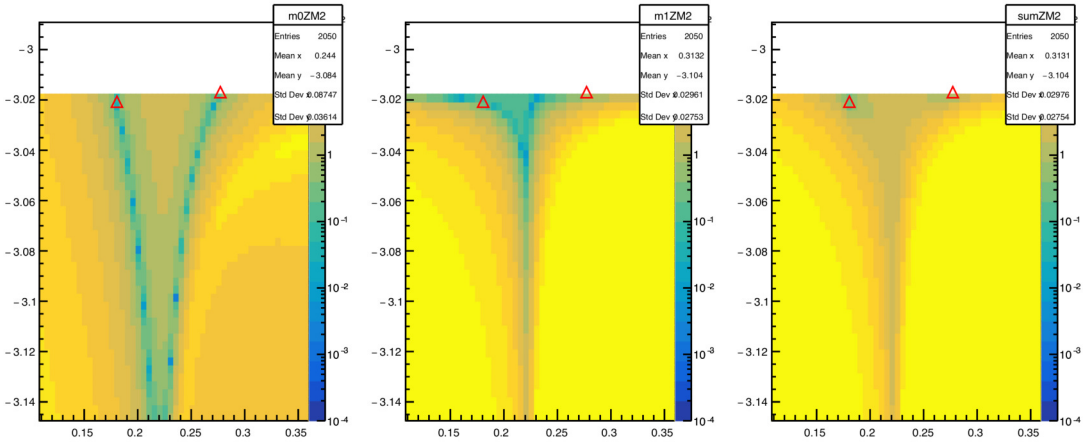

Figure 3.10: Choosing the values of z, ϕ. The horizontal and vertical axes are z ([mm]) and ϕ [rad], and the colour scale represents the sum of the absolute squared neutrino masses for the negative (positive) tau on the right (center), and their sum (right). The two triangles, identified as local minima of the right-hand plot, are the selected solutions.

Additional events are show in Figs. 3.11 and 3.12. The number of identified solutions varies from event-to-event. Sometimes no good solutions are found, in others 10 or more can be identified.

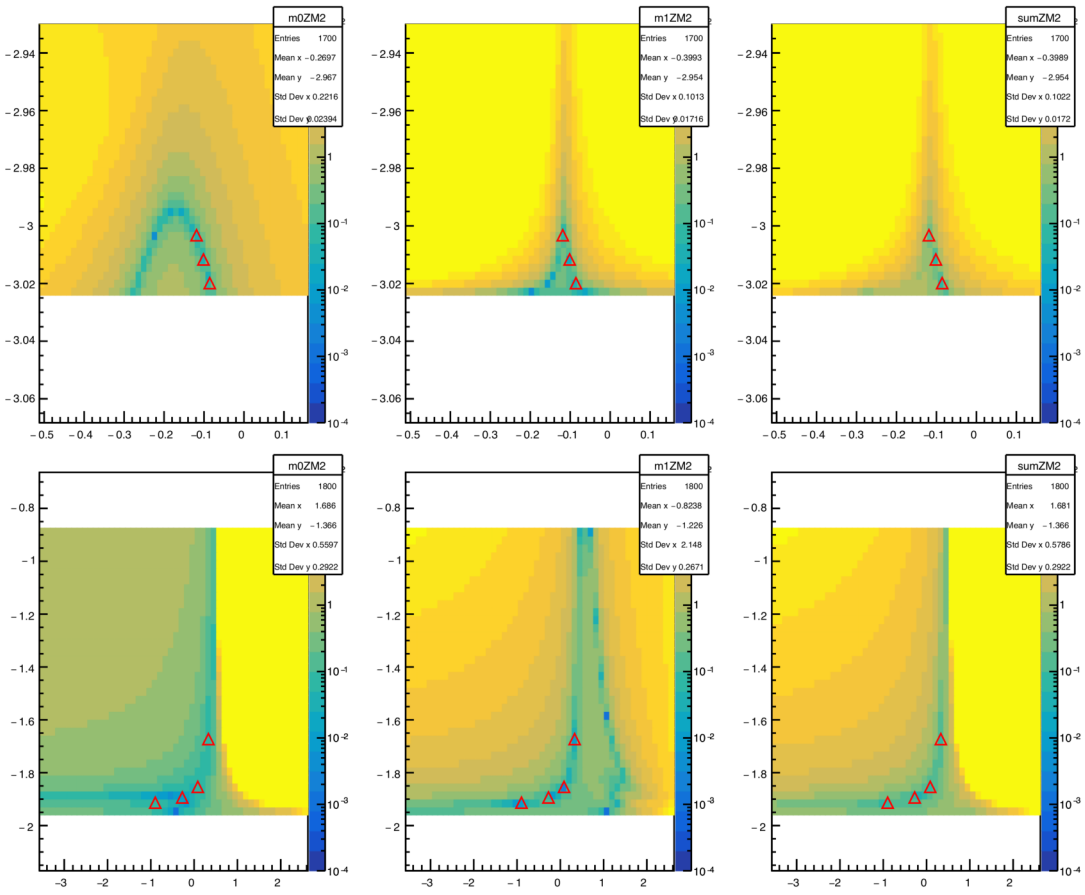

Figure 3.11: Example event with 3 and 4 solutions. The horizontal axis and the vertical axis are z and ϕ, respectively. The colour scale represents the invariant mass of neutrino. ed triangles show the position of identified solutions.

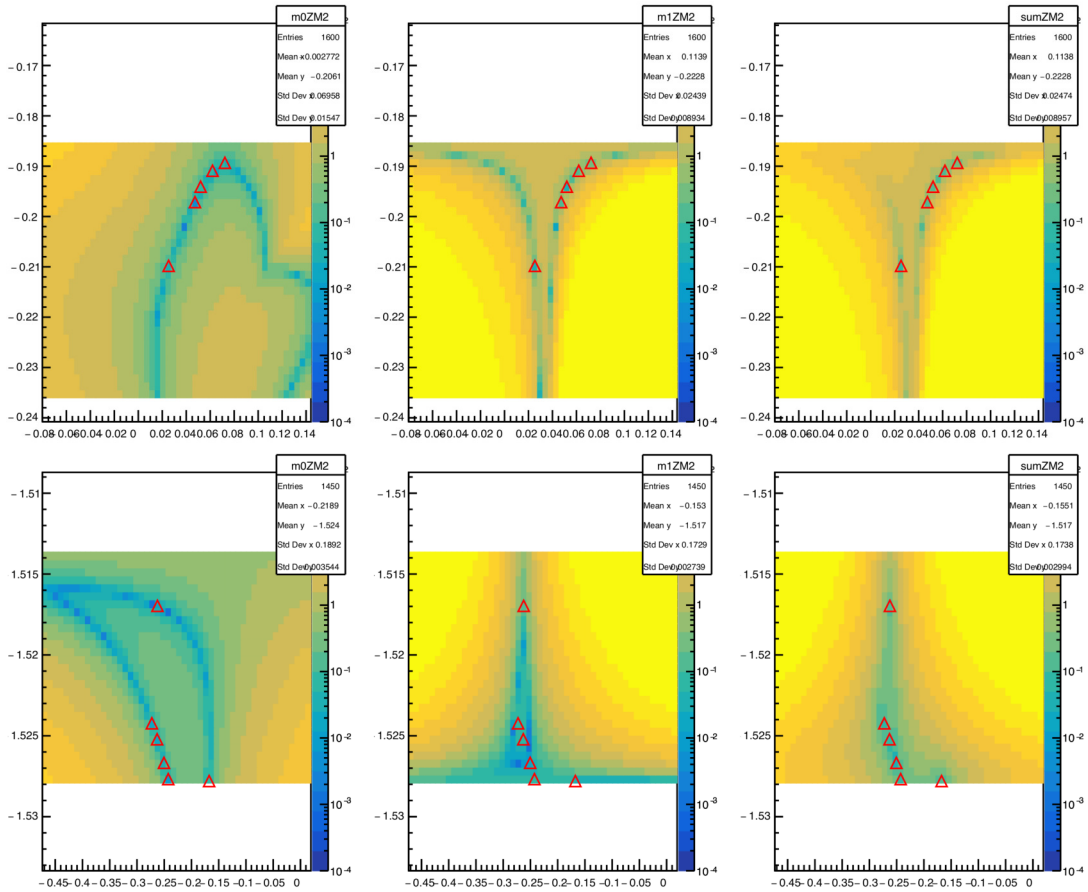

Figure 3.12: Example event with 5 to 6 solutions. The horizontal axis and the vertical axis are z and ϕ, respectively. The colour scale represents the invariant mass of neutrino. ed triangles show the position of identified solutions.

Number of solutions

Figure 3.13 shows the number of solutions found per event. The first plot considers all tau-pair events, and shows that there is a significant fraction of events for which zero solutions are identified. For reasons which are explained in the next section, we also plot the number of solutions in the subset of events in which the p_T of ISR photons is below 5 GeV, and in which no FSR photons are emitted. In this subset, the fraction of events with no solutions is very significantly reduced.

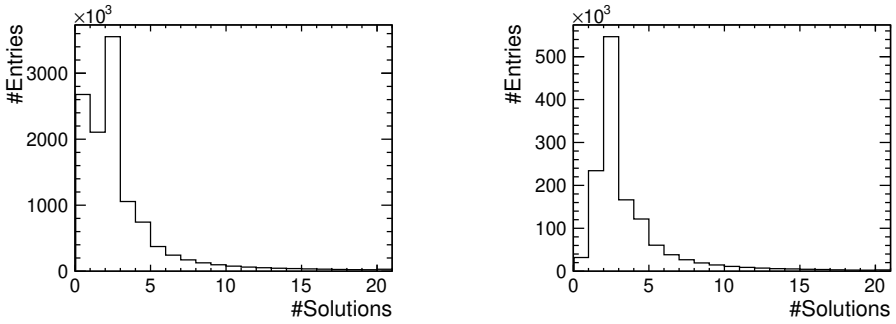

Figure 3.13: The number of solutions for all events (left) and for events with no FSR photon and ISR photon which has low transverse momentum $p_T < 5$ GeV (right).

It is difficult to distinguish which of multiple solutions is the correct one: they all satisfy the various constraints to a similar degree. One could imagine using additional information to distinguish them. For example, z_{IP} should typically follow a particular distribution of well-defined size determined by the collider parameters (at ILC, nominally a Gaussian with width ~ 200 μm and mean 0); if one of the solutions falls far from this distribution, it could be deweighted or discarded. Other ways to select solutions could depend on the solutions with more probable tau decay kinematics or $m_{\tau\tau}$, however this depends on the assumed physics model, which is what we are trying to measure. In the analyses shown in this thesis, we give equal weight to all identified solutions.

Figure 3.14 shows the angle between the MC-truth tau direction and the direction reconstructed by this method. Since multiple solutions are possible, the distribution includes all solutions. The angle is typically rather small, with most solutions being within a few mrad of the true direction, showing that the results are reasonable. We note that there is a relatively long tail extending to several 10s of mrad, due to "incorrect" solutions.

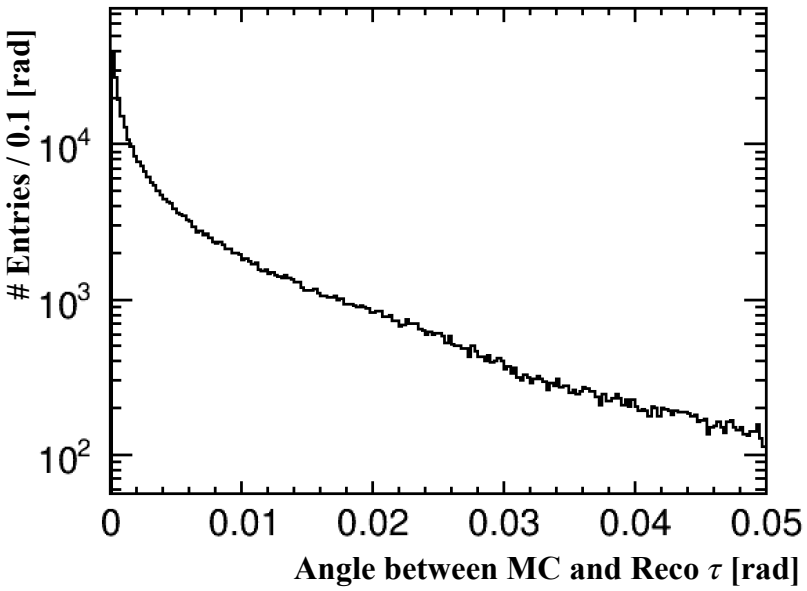

Figure 3.14: Angle between MC and reconstructed tau

Efficiency

Figure 3.15 shows the distribution in the invariant mass of tau-tau for all events containing at least one tau decay to π or ρ (red), and for the subset of those events in which the impact parameter method identifies at least one solution. We can clearly see peaks both at high mass and at the Z pole around 91 GeV.

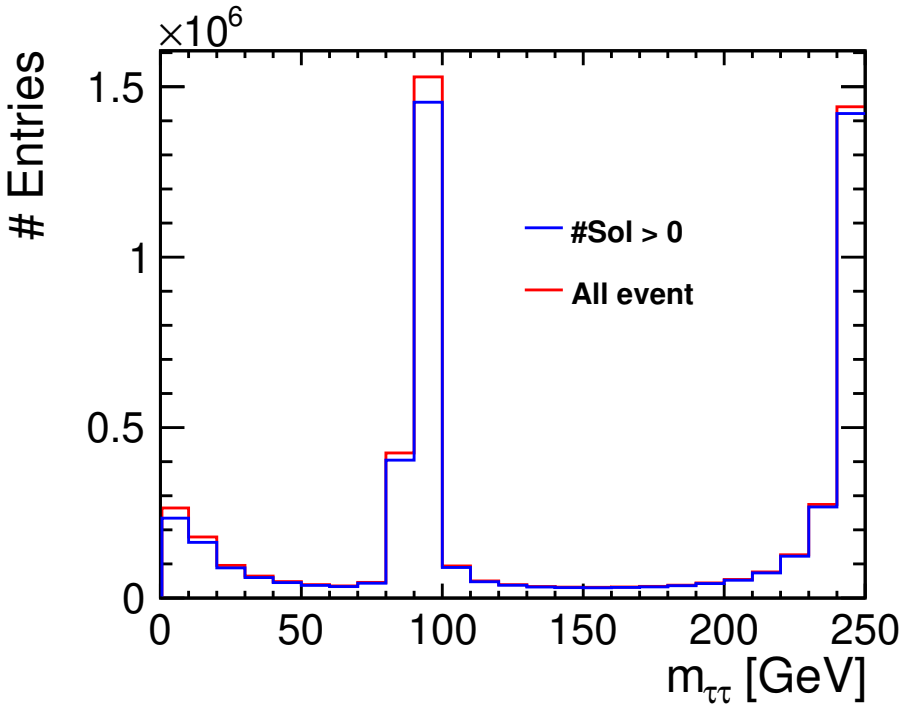

Figure 3.15: Comparison with MC $m_{\tau\tau}$for events with at least 1 τ decay to π or ρ. The red line represents all events and the blue line represents for events for which the impact parameter method can find at least one solution.

Figure 3.16 shows the method efficiency as a function of MC $m_{\tau\tau}$ for these same events. The black line corresponds to all events without any additional cut. The efficiency is above 95% at high mass, and reduces to 60 $\sim$ 70% at lower masses. There is an intriguing feature around the Z-pole.

We try to understand the drop in efficiency by cutting events with large initial or final state radiation. Removing events containing ISR with a total transverse momentum greater than 5 GeV results in the blue curve. Such events invalidate the assumption of collinear ISR, and are therefore expected to cause problems to the method, particularly at lower $m_{\tau\tau}$ where the amount of ISR is larger. The absolute efficiency indeed increases by 20 $\sim$ 30% for $m_{\tau\tau}$ below the nominal centre-of-mass energy. The structure around m_Z remains.

Removing events in which the tau-pair emit final state radiation results in the green curve, in which the efficiency is generally increased, and the feature around m_Z has disappeared. Final State Radiation is typically emitted close to one of the tau directions, and is therefore typically included into the visible tau jet momentum. This will cause the τ mass constraint to be invalidated, since it it the tau system after FSR which has the mass m_τ. A significant FSR therefore

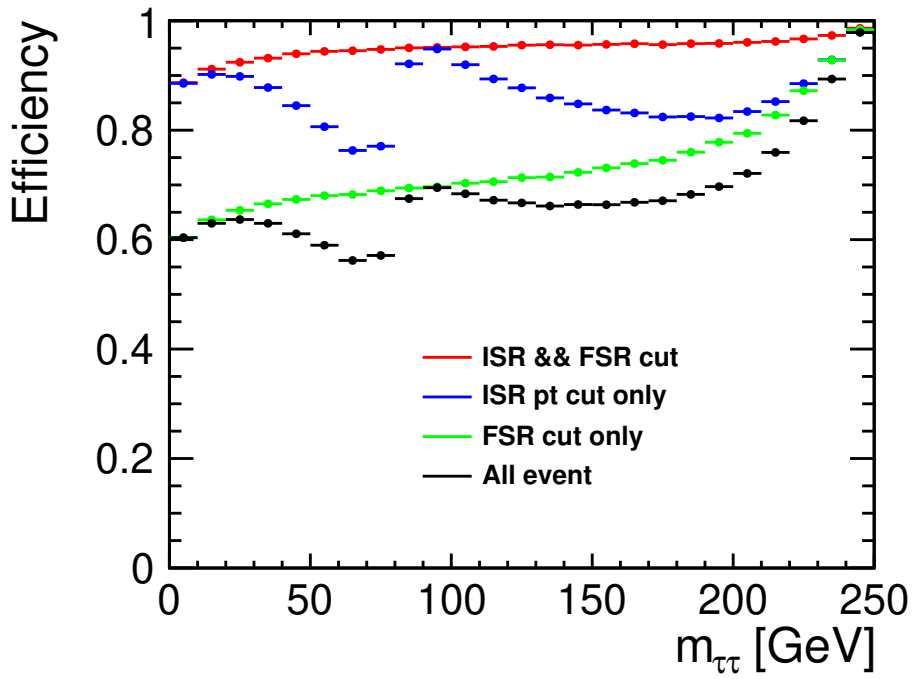

Figure 3.16: Impact parameter efficiency as a function of MC $m_{\tau\tau}$.

results in decreased efficiency. The structure around m_Z is due to the fact that FSR causes events to migrate to lower values of $m_{\tau\tau}$ (defined as the tau-tau mass *after* the emission of FSR). The range immediately below $m_{\tau\tau}$ contains no-FSR events with the addition of events originally at higher mass which have migrated to that $m_{\tau\tau}$ thanks to the emission of FSR. Since the Z peak contains so many events, even the small fraction of them which migrate to lower $m_{\tau\tau}$ due to FSR can make a significant contribution to lower masses, causing them to have a smaller average efficiency.

Applying both the ISR and FSR cuts, we obtain the red curve, which shows an efficiency above 95% for all $m_{\tau\tau}$ above ~ 50 GeV.

α method

In ϕ method, we search the $z_{IP} - \phi$ plane for local minima. The range of ϕ which contains reasonable solutions is often very narrow, and it can sometimes be difficult to discover good solutions in this very narrow range by brute-force methods. This gives rise to some inefficiency to find a good solution.

In a variation of the above method, using the same assumptions and constraints, we replace the ϕ free parameter by α of one the taus. α is the parameter defined in Eq. 3.5, the distance along the charged daughter trajectory from the point of closest approach (PCA) at which the tau decays. Choosing a particular value of α for the first tau, $r_1 = d_1 + \alpha_1 \hat{p}_1$, α_2 can be calculated by imposing

back-to-back-ness in the transverse plane:

$$\begin{aligned} \frac{r_{1,x}}{r_{1,y}} &= \frac{r_{2,x}}{r_{2,y}} \\ &= \frac{d_{2,x} + \alpha_2 \hat{p}_{2,x}}{d_{2,y} + \alpha_2 \hat{p}_{2,y}} \\ \alpha_2 &= \frac{r_{1,y} d_{2,x} - r_{1,x} d_{2,y}}{r_{1,x} \hat{p}_{2,y} - r_{1,y} \hat{p}_{2,x}} \end{aligned} \tag{3.12}$$

A choice of z_{IP} and α_1 thus defines both the azimuthal and polar angles of the two tau momenta, and we proceed as in the $z_{IP} - \phi$ method described above.

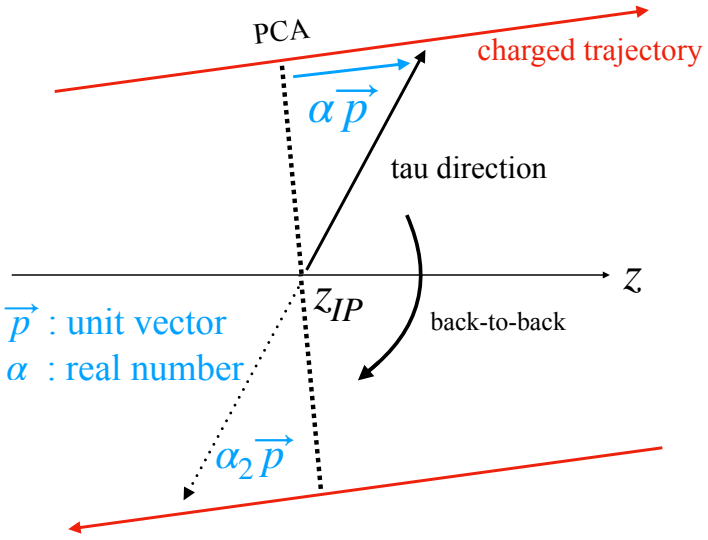

Figure 3.17: Alpha method

Polarimeter

Each event may have several solutions, which will result in different estimates of the polarimeter. In addition, each solution may result in two polarimeter measurements, one per tau, in the case that both taus decay into a decay mode we consider. Since the helicities of the two taus in an event are very strongly anti-correlated, we consider measurement from different taus to be estimators of the same quantity, the chirality of the tau lepton current. A single event therefore provides between 0 and 20 estimates of the tau chirality. As discussed above, it is not trivial to rank the solutions in a way that will not bias the results, so we treat each of them equally. For each event we fill a histogram with these estimators, which is then normalised to unity. It can be considered a probability density function for the polarimeter.

These single-event histograms are then summed over the whole sample. In this sample histogram, each event provides a weight of 1. Figure 3.18 shows the polarimeter distributions for taus of positive and negative helicity

The polarimeter distributions are close to the "triangular" distributions of the MC truth polarimeters in Fig. 3.2, however some small distortions are seen. These are due to the inclusion of the polarimeters calculated at the incorrect solutions.

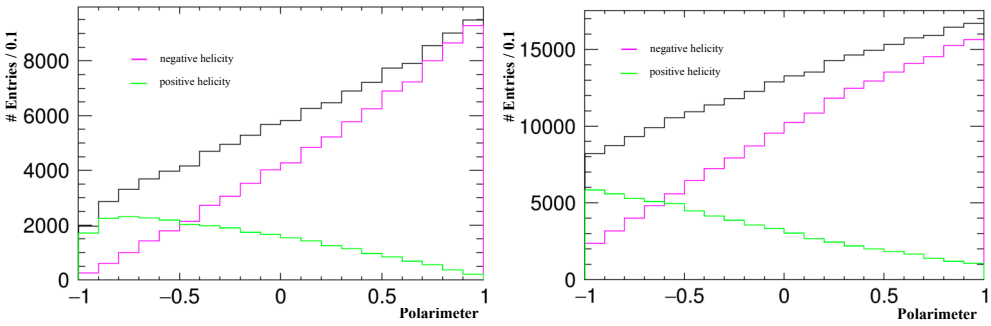

Figure 3.18: Impact parameter polarimeter as a function of MC $m_{\tau\tau}$ for $\tau \to \pi\nu$ decay (left) and $\tau \to \rho\nu$ decay (right).

Comparisons of the reconstructed polarimeter distribution with the MC-truth polarimeter is shown in Fig. 3.19. There is a sharp band with excellent agreement, and a broad region with no correlation due to the incorrect solutions.

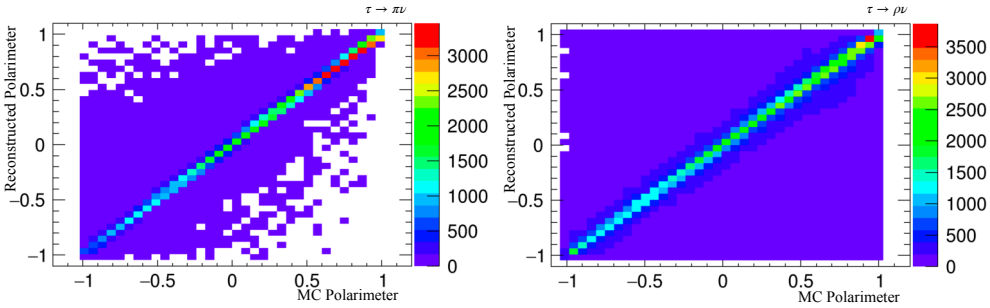

Figure 3.19: Polarimeter reconstructed using the impact parameter method compared to the MC-truth for $\tau \to \pi\nu$ (left) and $\tau \to \rho\nu$ decays (right).

3.3.5 Polarisation measurement

To measure the polarisation of a sample of events, we should fit distributions such as those in Fig. 3.20 to the sum of contributions from Left- and Right-handed taus. Each event contributes a weight of unity to the distribution, however this weight may be spread across several polarimeter values. The several polarimeters measured in a single event may well be statistically correlated, since they are based on the same experimental inputs. A simple fit of the distribution (e.g. by a χ^2 or likelihood method) will therefore not result in correct statistical uncertainties.

Jackknife method

To estimate the statistical uncertainties, we use a brute-force method known as the "Jack-knife" method. The basic idea of the Jackknife method is that the estimator, in this case tau polarisation, is calculated by sequentially deleting one event (which can correspond to several polarimeter measurements) from the sample, and estimating the polarisation in each of these sub-samples. For a sample of n events, let the estimated parameter using all events be $\hat{P}$. There are n sub-samples of $n-1$ events, in which the fitted parameter is $\hat{P}_i$. The

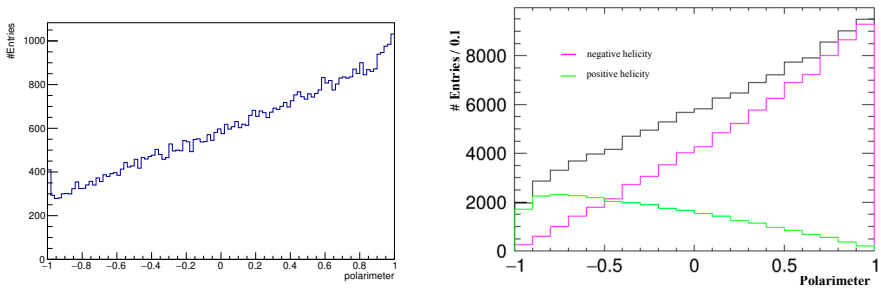

Figure 3.20: An example polarimeter distribution (left) and the expected distributions for negative and positive helicity taus (right).

Jack-knife method tells us that the variance on the extracted parameter P can be estimated as [29]

$$\mathrm{Var}(P) = \sigma_P^2 = \frac{n-1}{n}\sum_{i=1}^{n}(\hat{P}_i - \hat{P})^2 \tag{3.13}$$

3.3.6 Check of fitting method

Our aim is to measure the tau polarisation as a function of the scattering angle θ_{τ^-}. We run a number of toy-MC experiments to check the behaviour of the fit method outlined above, using events with $m_{\tau\tau}>$ 240 GeV and in which at least one τ decays to π or ρ.

Samples of 50k events with different "artificial" polarisation P_{in} were created in 10 bins of $\cos\theta_{\tau^-}$ by changing the ratio of right-handed N_R to left-handed N_L events $P_{in} = \frac{N_R - N_L}{N_R + N_L}$. Each sub-sample was fitted to extract the tau polarisaton, and the Jack-knife method was used to estimate its uncertainty.

Figures. 3.21 presents the fitted value of the polarisation as a function of the true value of the input polarisation $P_{in} = \frac{N_R - N_L}{N_R + N_L}$, in the 10 bins of $\cos\theta_{\tau^-}$. The fitted polarisaton depends linearly on the input polarisation, and the dependence $\cos\theta_{\tau^-}$ is seen to be very small. We note that a significant bias is observed, with the fitted polarisation always having a smaller magnitude than the input: e.g. for an input polarisation of ± 1.0, the fitted polarisation is $\pm \sim 0.85$. This can be understood as the effect of wrong event solutions, which will on average tend to dilute the polarisation measurement, resulting in a smaller extracted value.

The polarisation uncertainty obtained from the Jack-knife method is presented in Fig. 3.22 for the same samples. For the 50k events per sample assumed in this toy-MC, the absolute uncertainty on the polarisation is in the range $0.004 \rightarrow 0.007$. It depends on the true value of the polarisation (the uncertainty is largest for zero polarisation), but seems rather insensitive to $\cos\theta_{\tau^-}$.

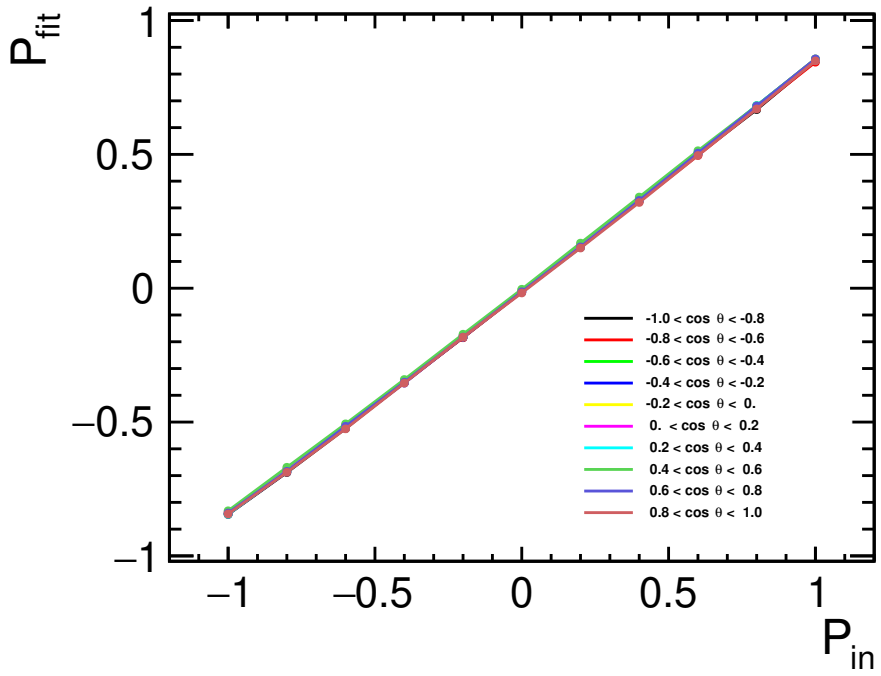

Figure 3.21: Jackknife method result of the tau polarisation: The y-axis represents the tau polarisation obtained by fitting and x-axis is an artificial input polarisation for each $\cos\theta_{\tau^-}$ region.

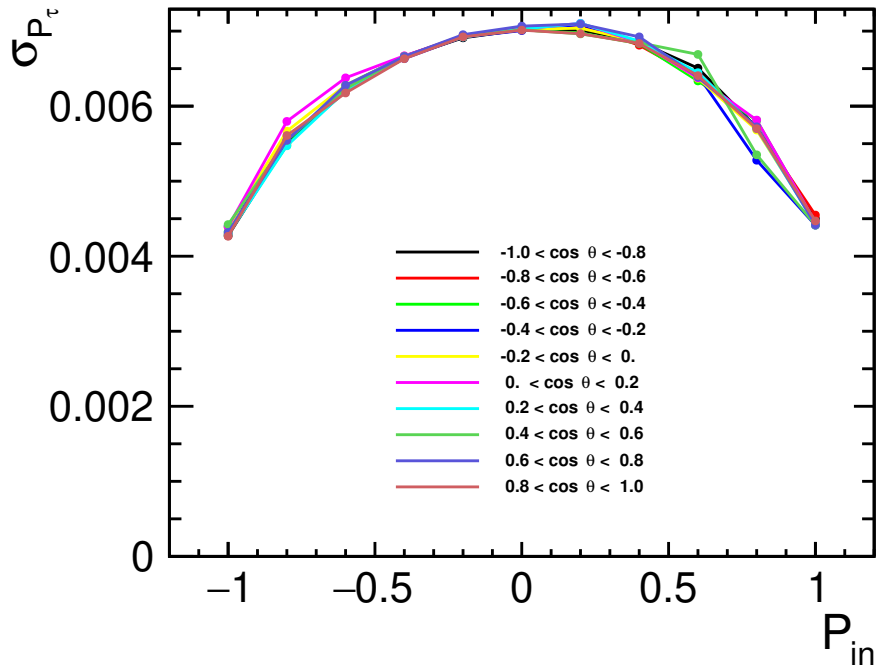

Figure 3.22: Jackknife method result of the tau polarisation error: The y-axis represents the tau polarisation error obtained by Jackknife method and x-axis is an artificial input polarisation for each $\cos\theta_{\tau^-}$ region.

3.3.7 Extrapolation to ILC-250

Next, the sensitivity of the tau polarisation was investigated assuming the beam polarisation datasets for 2.0 ab^{-1} of data forseen for ILC-250 using this Jackknife method. The electron beam is 80% polarised and the positron beam is 30% polarised. The 2.0 ab^{-1} of integrated luminosity forseen at ILC-250 is split as follows: ($e^-_{L80}e^+_{R30}$, $e^-_{R80}e^+_{L30}$,$e^-_{L80}e^+_{L30}$,$e^-_{R80}e^+_{R30}$) as (45%,45%,5%,5%).

Figure. 3.23 shows that the invariant mass of tau pair for $e^-_{L80}e^+_{R30}$ sample (eLpR) and $e^-_{R80}e^+_{L30}$ sample (eRpL). For radiative return to Z pole events ($m_{\tau\tau}$ = 91± GeV), the expected number of taus is $N = 6.8 \times 10^6$ and for high mass tau-tau events ($m_{\tau\tau} = 245 \pm 5$ GeV), the expected number of taus is $N = 4.9 \times 10^6$. Jackknife method was performed for high mass tau-tau event with $N = 4.9{\times}10^4$ taus and Z pole event with $N = 6.8{\times}10^6$ taus, respectively, and tau polarisation precision estimation was performed. Figures. 3.24 and 3.25 show that the polarimeter distributions for at least 1 τ decays to π or ρ (for example, in the event 1 $\tau \to \pi\nu$ and 1 $\tau \to e\nu\nu$, the measurement is still performed using the τ decayed to π.) with left-handed and right-handed polarised beam sample. As a result of tau polarisation precision measurement, tau polarisation error for the high mass tau-tau event are 0.0618% and 0.0614% for the left- and right-handed polarised samples, respectively. For Z pole events, the results were 0.0566% and 0.0579%, for the left- and right-handed polarised samples, respectively.

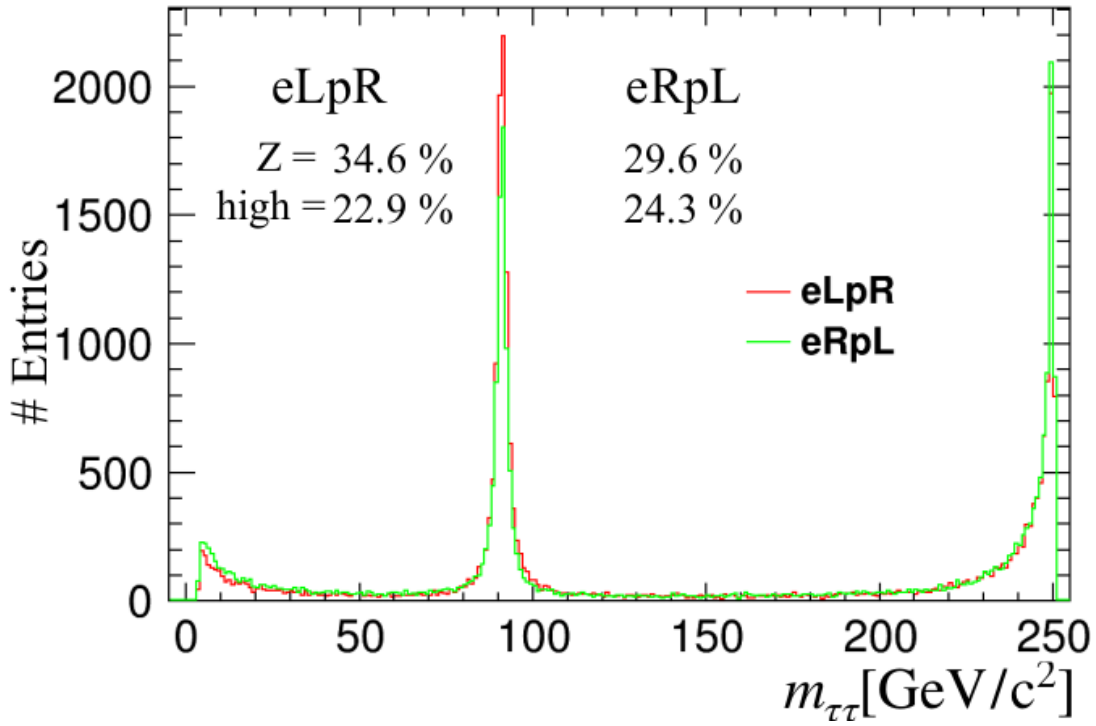

Figure 3.23: The invariant mass of tau-tau $m_{\tau\tau}$ for two types of samples: $e^-_{L80}e^+_{R30}$ sample (red) and $e^-_{R80}e^+_{L30}$ sample (green).

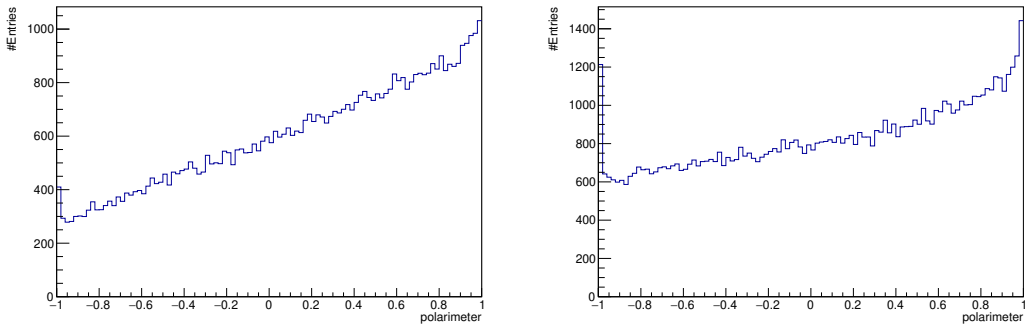

Figure 3.24: Polarimeter distributions for at least 1 $\tau \to \pi/\rho$ decay with eLpR sample. For events with radiative return to Z pole event (left) and high mass tau-tau (right).

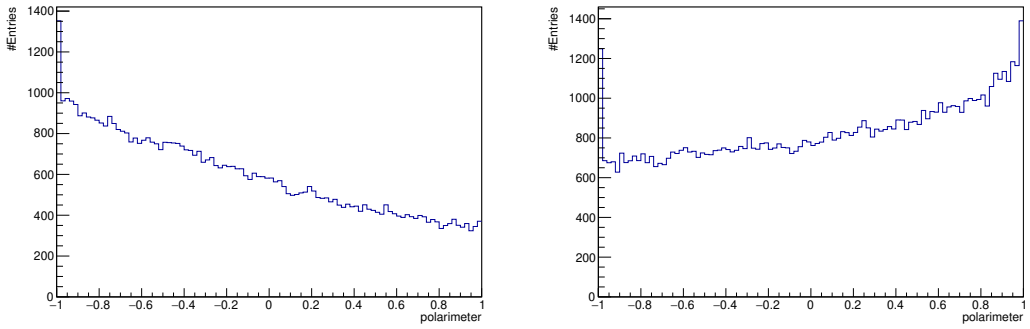

Figure 3.25: Polarimeter distributions for at least 1 $\tau \to \pi/\rho$ decay with eRpL sample. For events with radiative return to Z pole event (left) and high mass tau-tau (right).

3.4 Constraining physics beyond the SM using the tau polarisation

In this section, we evaluate the performance of the ILC at 250 GeV in the search for new physics by comparing it with the Z' model (SSM, E6,, ALR, GHU) using tau polarisation and the possibility of searching for a new physical model based on the accuracy of the tau polarisation obtained in this study.

First, we evaluate the performance of the Z' model; the coupling constants of Z' differ from model to model, and in this section we use the Sequential Standard Model (SSM) and the Alternative Left-Right symmetric model (ALR), and the $E6$ model.

Figures. 3.26 and 3.29 show the cross-section and the tau polarisation predicted by each Z' models and SM, and its deviations from SM as a function of the centre-of-mass energy and the the $\cos\theta_{\tau^-}$ with left-handed and right-handed polarised beams.

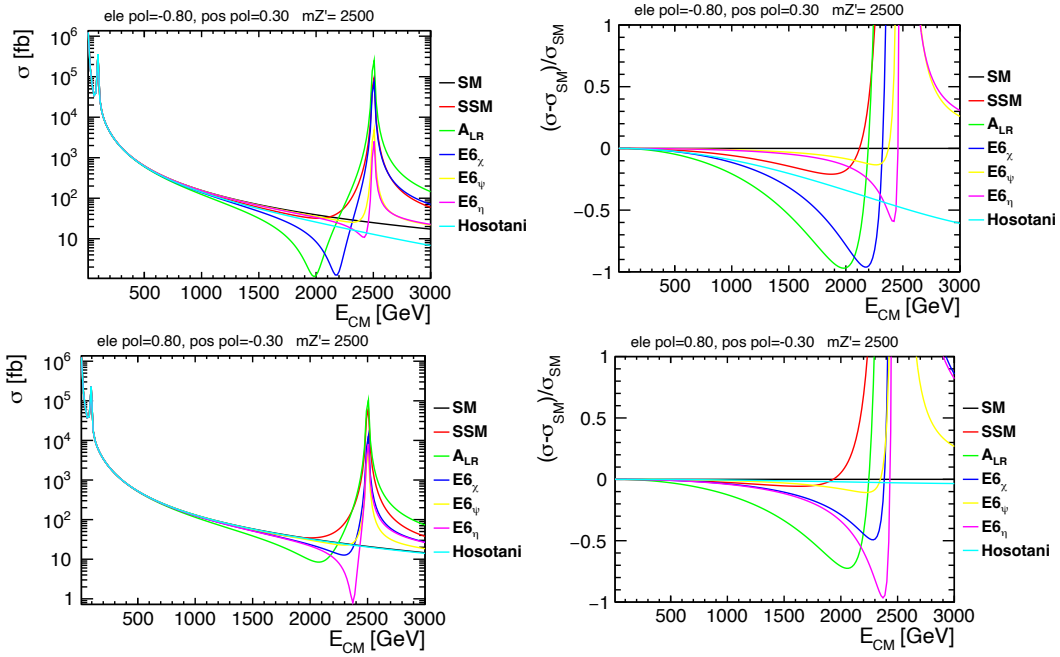

Figure 3.26: The cross-section (Left) and its deviations from SM as a function of the centre-of-mass energy for each Z' models with left-handed (Top) and right-handed (Bottom) polarised beams.

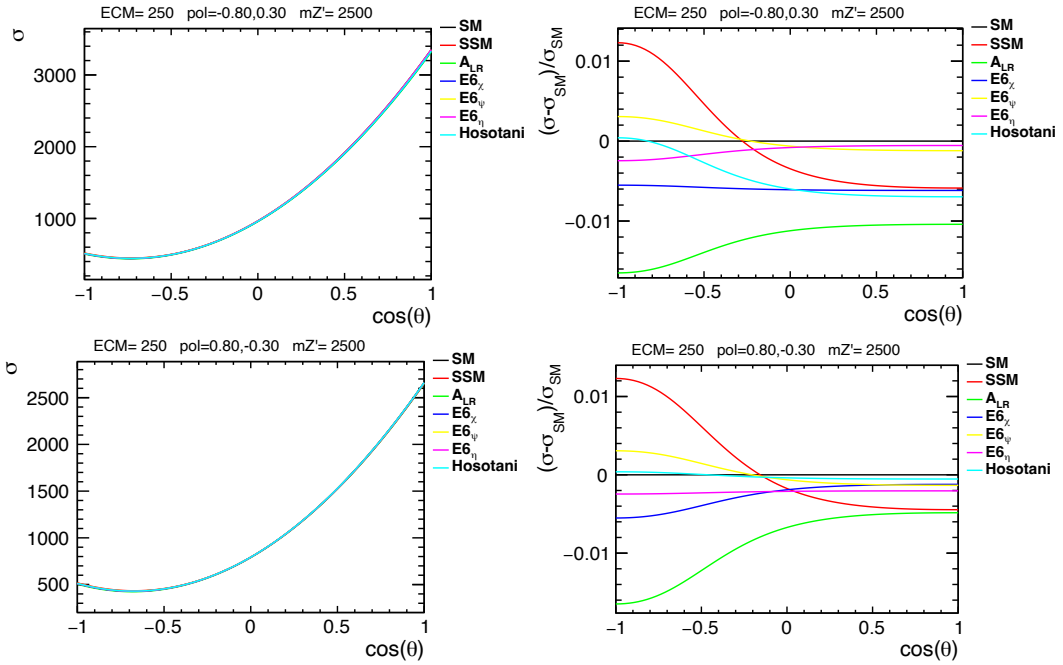

Figure 3.27: The cross-section (Left) and its deviations from SM (Right) as a function of the $\cos\theta_{\tau^-}$ for each Z' models with left-handed (Top) and right-handed (Bottom) polarised beams.

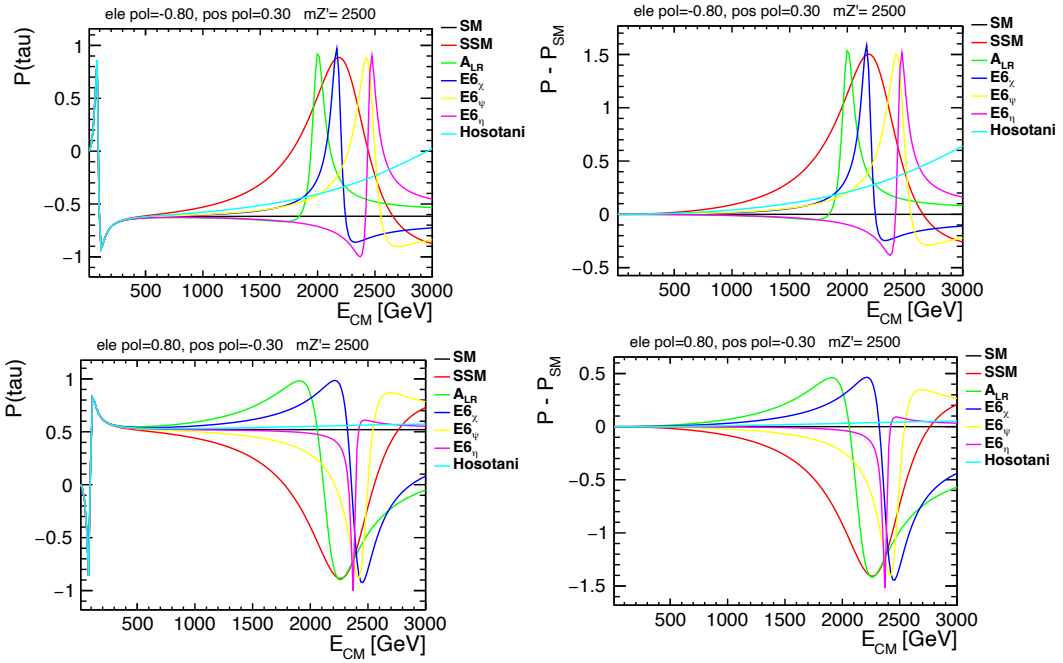

Figure 3.28: The average tau polarisation (Left) and its deviations from SM (Right) as a function of the centre-of-mass energy for each Z' models with left-handed (Top) and right-handed (Bottom) polarised beams.

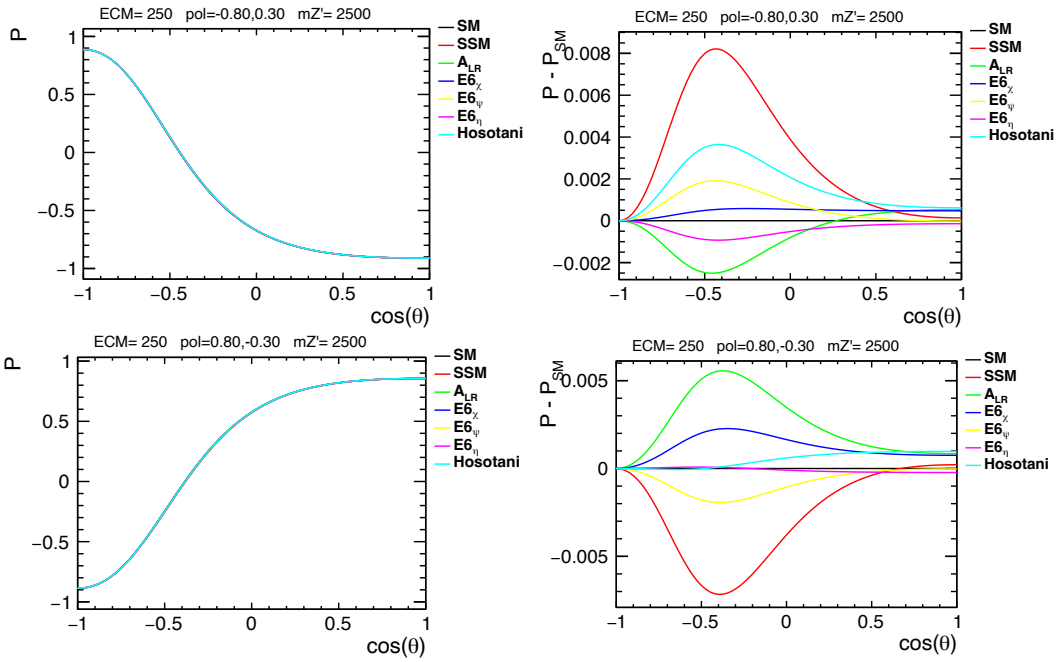

Figure 3.29: The tau polarisation (Left) and its deviations from SM (Right) as a function of the $\cos\theta_{\tau^-}$ for each Z' models with left-handed (Top) and right-handed (Bottom) polarised beams at 250 GeV.

3.4.1 Results of analysis

For the differential cross-section and the tau polarisation, the entire angular range of $\cos\theta_{\tau^-}$ is divided into bins, and for each bin the deviation from SM of them predicted from each model of the i-th bin is determined. Then, the corresponding χ^2 can be expressed as [30]:

$$\chi^2 = \sum_{bins} \sum_{\{\sigma,P_\tau\}} \sum_{L,R} \frac{[\mathcal{O}(\mathrm{SM}+Z') - \mathcal{O}(\mathrm{SM})]^2_{bin}}{\delta\mathcal{O}^2_{bin}} \tag{3.14}$$

where $\mathcal{O} = \frac{dP_\tau}{d\cos\theta}, \frac{d\sigma}{d\cos\theta}$ in each bin for the tau polarisation and the differential cross-section, respectively. Then, the probabilities that the Z' model deviation are consistent with the SM are calculated by using these χ^2. Figure. 3.30 and 3.31 show the χ^2 distributions and the probabilities by using MC-truth and reconstructed results, respectively. The lower this probability is, the easier it is to find the Z' bosons for that mass and new physics model. Table. 3.1 shows the upper limit of Z' masses that can be found at 95% C.L. for each model.

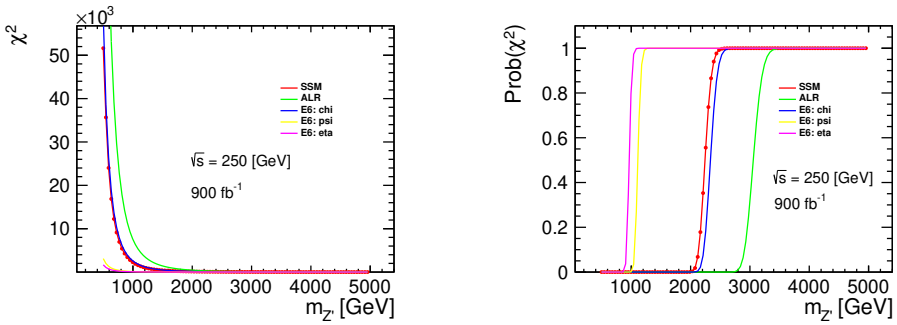

Figure 3.30: Chi-squared distributions as a function of the mass of Z' for each Z' models at ILC-250 with polarised beams and the expected integrated luminosity of 900 fb^{-1} using MC-truth and the probabilites of the χ^2 that the deviation of Z' model are consistent with the SM prediction at ILC-250 using the expected error from MC-truth. The results of the cross-section and the tau polarisation and the tau polarisation with left- and right-handed samples are combined to calculate the χ^2.

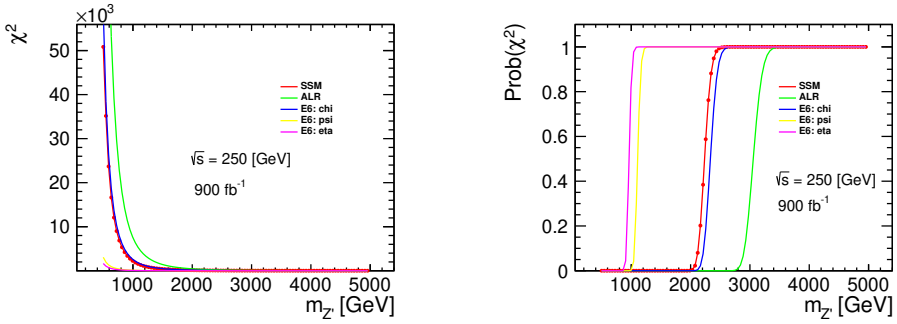

Figure 3.31: Chi-squared distributions as a function of the mass of Z' for each Z' models at ILC-250 with polarised beams and the expected integrated luminosity of 900 fb^{-1} using reconstructed results and the probabilites of the χ^2 that the deviation of Z' model are consistent with the SM prediction at ILC-250 using the expected error from MC-truth. The results of the cross-section and the tau polarisation and the tau polarisation with left- and right-handed samples are combined to calculate the χ^2.

Table 3.1: Upper limit on the mass of Z' in unit of GeV detectable $e^+e^- \to \tau^+\tau^-$ measurement of the ILC at 250 GeV centre-of-mass energy at 95% C.L. for each model

Z' model	MC	PFO
SSM	2103.92	2038.46
ALR	2868.72	2795.89
$E6_\chi$	2189.57	2131.97
$E6_\psi$	1043.01	1005.24
$E6_\eta$	906.951	872.219

In this analysis, three values of $\theta_H = 0.09, 0.10, 0.11$ are assumed to determine whether the GHU model deviations from SM can be seen at ILC-250. Figures. 3.32 and 3.33 show the deviations from SM of the cross-secion and the tau polarisation in the GHU model with different θ_H values and the expected error at ILC-250. For all values of θ_H, sufficient deviations from SM can be observed. The probabilities of them being consistent with SM is almost zero, and if the GHU model is correct within the range of possible values of θ_H, the analysis of the tau channel alone is sufficient to new physics search at ILC.

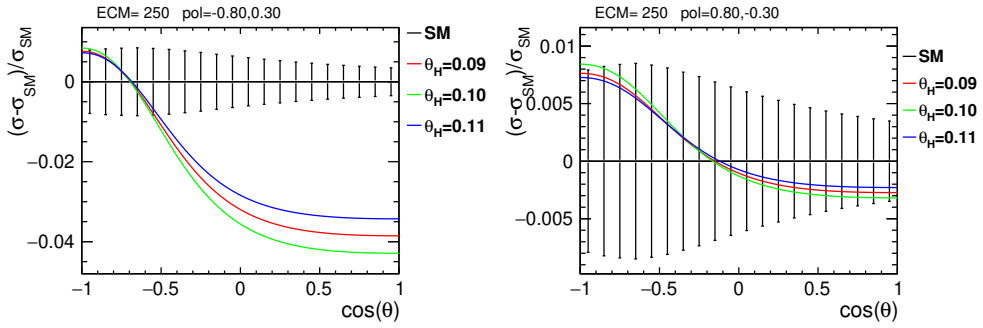

Figure 3.32: The deviations from SM $e^+e^- \to \tau^+\tau^-$ cross-section in the GHU model of Z' for left-handed (Left) and the right-handed (Right) polarised beams with the different values of $\theta_H = 0.09, 0.10, 0.11$. The error bars represent the expected accuracy of this analysis.

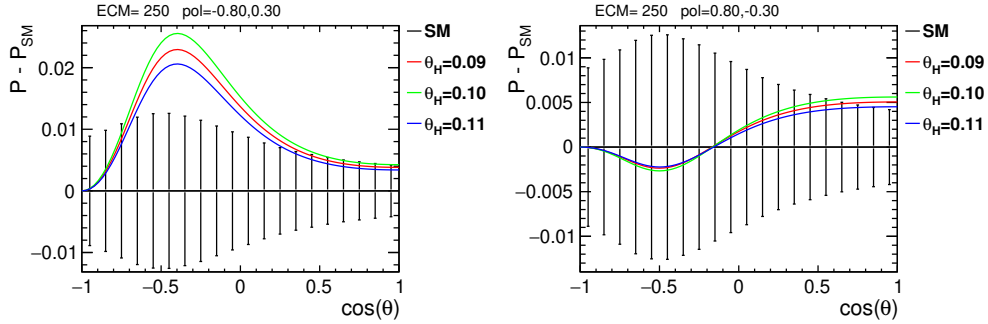

Figure 3.33: The deviations of the tau polarisation from SM $e^+e^- \to \tau^+\tau^-$ process in the GHU model of Z' for left-handed (Left) and the right-handed (Right) polarised beams with the different values of $\theta_H = 0.09, 0.10, 0.11$. The error bars represent the expected accuracy of this analysis.

3.5 Conclusion

The reconstruction of tau polarisation at ILC-250 was investigated. For events with $m_{\tau\tau}>$ 240 GeV, "Cone method" works for 70% of taus and "Impact parameter method" efficiency is $>$ 90%. "Midpoint method" was used if "Cone method" fails. Polarimeters were reconstructed in the $\tau \to \pi\nu$ and $\tau \to \rho\nu$ decay modes, and used to estimate the tau polarisation and its error.

Reasonable agreement between MC truth polarimeter value and the one from each method for both $\tau \to \pi\nu$ and $\tau \to \rho\nu$ decay were found.

Jackknife method was used to estimate tau polarisation errors and check its bias. There is no $\cos\theta_\tau$ dependence and the tau polarisation obtained from fit as a function of an artificial input polarisation can be used for the calibration of tau polarisation measurement using Jackknife method.

The experimental sensitivities to the tau polarisation of impact parameter method are about 0.06% for events with $m_{\tau\tau}>$ 240 GeV and also radiative return to Z pole event around $m_{\tau\tau}\sim$ 91 GeV , assuming 900 fb^{-1} of $e^-_{L80}e^+_{R30}$ and $e^-_{R80}e^+_{L30}$ beam polarisation.

A new physics model search for Z' was performed using the tau polarisation error obtained by the newly developed reconstruction method. Using both tau polarisation and cross-sections, the new physics model was found to be sensitive to Z' with masses up to 820 GeV to 2.8 TeV.

Part 2

CHAPTER 4

OPTIMISATION STUDY OF THE ASIAN GEM MODULE FOR TPC READOUT

4.1 Introduction

4.1.1 Tracking requirements at a Higgs Factory

The physics program at collider experiments past, present, and future require essentially perfect efficiency to reconstruct charged particles produced in collisions, to measure their direction, their origin with respect to the interaction vertex to identify displaced vertices, and to estimate their momentum.

At experiments for future lepton Higgs Factory colliders, requirements on the tracking system come from

- momentum resolution to allow reconstruction of the Higgs mass recoiling against a Z boson decaying into muons; the experimental smearing due to momentum resolution should not dominate over that induced by the collider's beam energy spread.
- impact parameter resolution to allow the efficient reconstruction of tau lepton decays and heavy flavour quark jets

The efficiency and resolution for charged particle reconstruction should cover as much of the solid angle as possible, given the constraints from the machine-detector interface, and should cover a range of momentum from $\mathcal{O}(100)$ GeV to $\mathcal{O}(100)$ MeV to reconstruct all produced particles.

Tracks produced by the decays of long-lived particles, whether photon conversions, K-short decays, or BSM particles, should also be detected with very high efficiency to fully reconstruct events and to search for unexpected signatures. The ability of the tracking system to distinguish particle types, particularly charged hadrons, by means of their specific energy loss as described by the Bethe-Bloch formula, provides an additional lever with which to analyse events.

The analysis of tau leptons, as discussed in the first part of this thesis, relies on the good performance of the charged particle tracking system. The charged decay products of the tau must be reconstructed with high efficiency, and their momentum measured with good precision. The measurement of the particle trajectories in the vicinity of the interaction region is a central element of the

analysis. In addition to the tracking system, the reconstruction of a majority of tau decays also depends on information from both the calorimeter systems, to measure neutral pion decays to photons and to distinguish charged leptons and hadrons.

Since the energy resolution of calorimeters is intrinsically less precise than that of tracking detectors, experimental precision on tau lepton reconstruction is not dominated by the tracking detector precision.

For these reasons, the performance requirements on the tracking detectors coming from tau lepton reconstruction are less stringent than those coming from other measurements, largely coming from the Higgs physics program, in part due to the very small natural width of the Higgs boson. A particular aspect of taus is the reconstruction of very nearby tracks from multi-prong decays of highly boosted taus.

4.1.2 Tracking technologies

Several technologies can be considered for the tracker. Leading examples are a full silicon tracker or gas-based detectors, such as a drift or time projection chamber. These options present different advantages and challenges, which depend on the experimental environment in which it is to be operated.

A silicon tracker provides a relatively small number of very precise measurements of particles' trajectories, while a gas-based detector typically provides a larger number of less precise measurements. Gas-based detectors contain only a very small amount of material within the active tracking volume, leading to reduced multiple scattering and therefore better resolution for low momentum particles, and can also typically provide better measurement of the specific energy loss dE/dx than a silicon tracker. A time projection chamber in particular involves the drift of charge over metre-scale distances, which introduces sensitivity to a build-up of ions within the tracking region.

The ILD has selected a hybrid tracking system, with a large TPC complemented by a small number of silicon detector layers, placed before and after the gas volume. The TPC allows quasi-continuous reconstruction of charged particle trajectories, providing excellent efficiency at all relevant momenta, also for highly displaced tracks. Inner and outer silicon layers provide high-precision points on tracks which, when combined with the TPC measurement, meet the momentum resolution requirement. The small mass of the main tracker provides good resolution also at low momenta, while its measurement of dE/dx provides good statistical separation of pions from kaons (and protons) up to several 10s of GeV. The large number of measurements of each track results in a robust system with built-in redundancy. The beam structure of the ILC, with its 200 ms–long "quiet" periods between bunch trains, permits the use of a gating system to block the majority of secondary amplification ions from the drift volume, minimising the concentration of ions in the drift region.

TPCs have been operated successfully at several collider experiments (e.g. ALEPH and DELPHI at LEP, ALICE at the LHC), and liquid-based TPCs are also increasingly being used in neutrino experiments (MicroBoone, T2K near detector, DUNE). They offer a very complete picture of the charged particles produced in particle interactions.

4.1.3 Operation Principle of TPC

The TPC can reconstruct the three-dimensional trajectory of charged particles. A schematic image of ILD's TPC is shown in Fig. 4.1. The TPC has a cylindrical shape with an outer radius of 1.8 m. It is divided into two volumes, each approximately 2.2 m long, separated by a HV cathode positioned at $z = 0$ (i.e. normal to the ILC beampipe, and aligned with the nominal interaction point). Each volume is closed by an end-plate instrumented with readout modules. The purpose of the TPC is to measure the trajectory and momentum of the charged particles, as well as to identify particle type by mans of their specific energy loss dE/dx. Charged particles entering the TPC ionise the gas molecules within it. The ionisation electrons drift along the electric field (xx V/m aligned with the detector axis) towards the readout end-plates; a HV cathode is positioned at $z = 0$. The solenoidal 3.5 T B-field of the experiment allows the TPC to act as a magnetic spectrometer to measure particle momenta, and also reduces the transverse diffusion of ionisation electrons as they drift towards the readout anode.

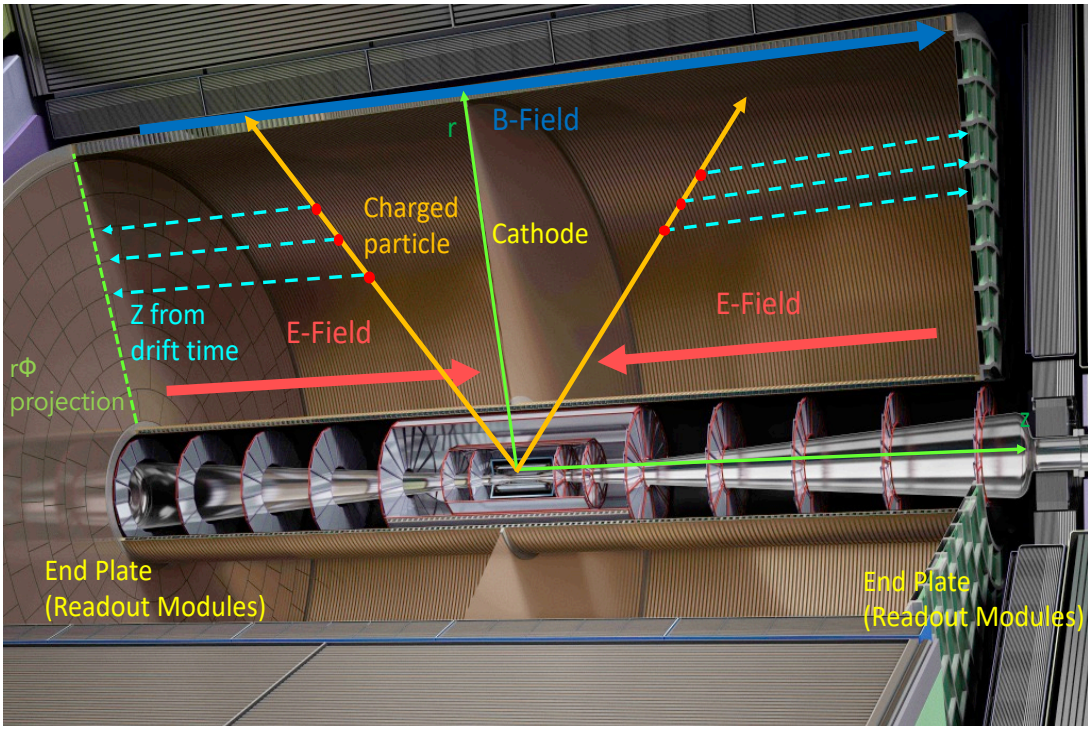

Figure 4.1: Schematic image of a TPC.

The TPC end-plates are each instrumented with around 240 readout modules of size 17×21 cm, arranged in 8 rings. Each module is segmented into $\sim 1{\times}6mm^2$ readout pads in the $r-\phi$ and r directions, for a total of around 1 M channels per end-plate. This corresponds to 220 individual measurements for a central track which passes through the TPC volume.

As the signal current generated by the ionisation electrons is too weak to be measured directly, the signal is gas amplified and read out within the end-plate readout module. A number of gas amplification technologies are being considered for the readout of the ILD TPC: Gas Electron Multiplier (GEM),

resistive Micromegas, and silicon readout based on the TimePix sensor.

4.2 Gas amplification

We make a brief survey of these gas amplification technologies, before discussing the GEM in more detail.

4.2.1 MicroMEGAS

Micro-Mesh Gaseous Structure (MicroMEGAS) is a MPGD detector developed by Y. Giomataris in 1996, whose structure is shown in the Fig. 4.2 [31]. The MicroMEGAS consists of a drift region of several mm separated by a microscopic mesh from an amplification region of about 100 μm width. The mesh is supported by pillars, and strip electrodes are used for signal readout.

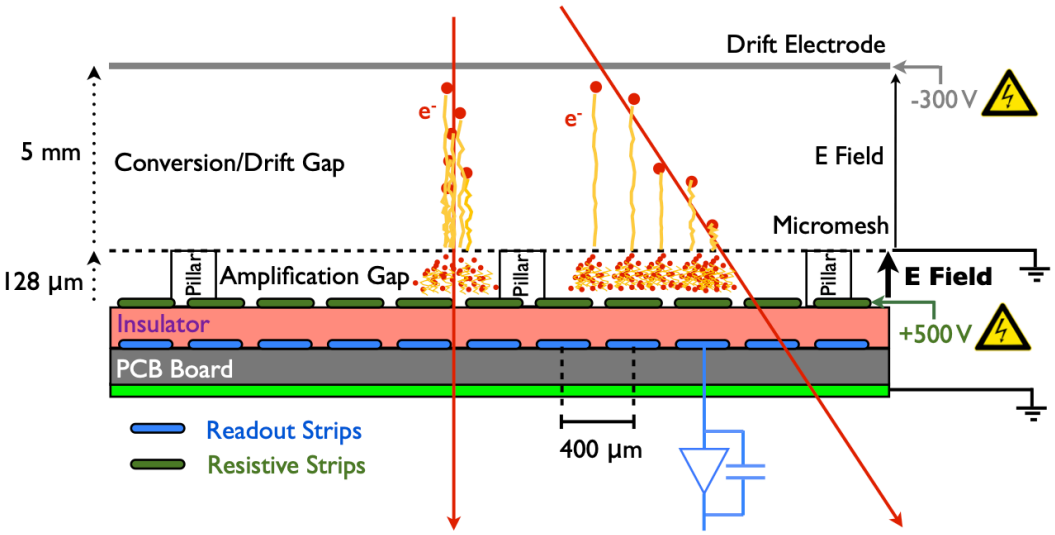

Figure 4.2: The structure of the MicroMEGAS.

By applying a negative high voltage to the mesh and a positive high voltage to the drift electrode, an electric field can be formed in the drift region (between mesh and drift electrode). Figure. 4.3 shows the electric field structure of MicroMEGAS [32]. This electric field causes the seed electrons produced by the incident particles to move in the direction of the anode strip.

These electrons are then amplified in the amplification region (between the strip electrode and the mesh) and can be detected as a signal. The electric field in the drift region is of the order of several hundred V/cm, whereas the electric field in the amplification region is of the order of tens of kV/cm, so that most electrons can pass through the mesh. Positive ions produced in the electron avalanche process are quickly absorbed by the mesh, making MicroMEGAS suitable for use in environments with high particle incidence.

Figure. 4.4 shows the calculated gas gain as a function of the MicroMEGAS gap width when using a He/isobutane 94/6 gas mixture [32]. The gas gain

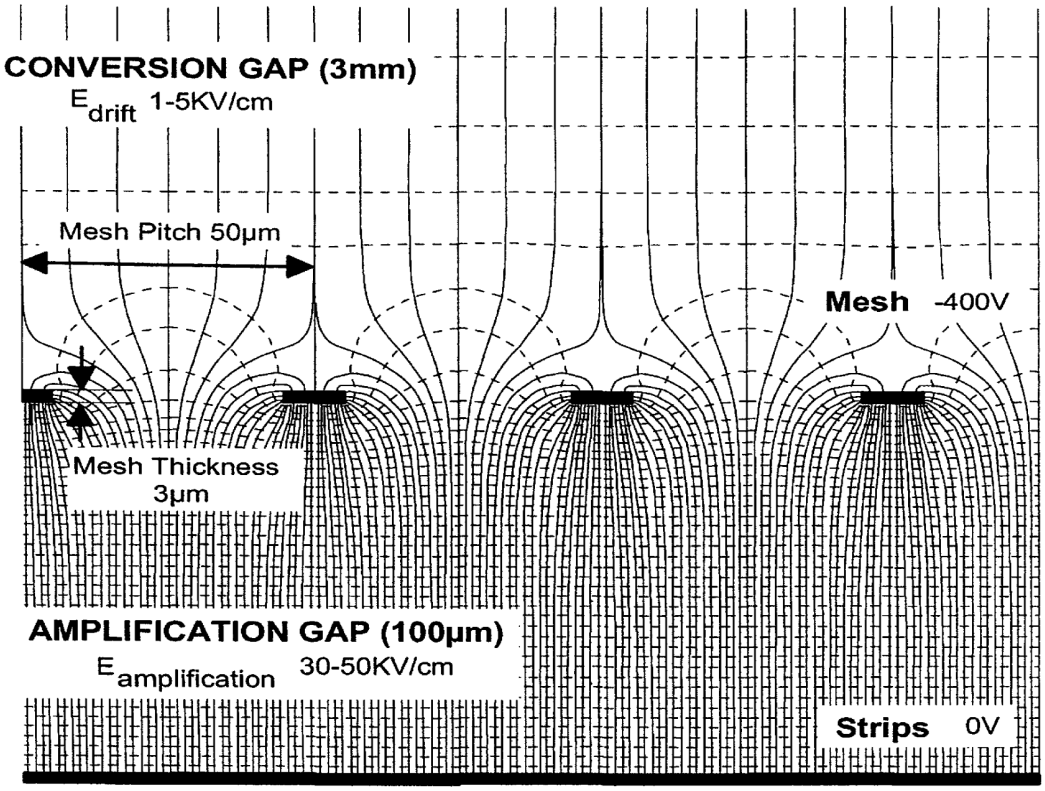

Figure 4.3: Electric field structure in the vicinity of the MicroMEGAS mesh.

reaches a maximum for gaps in the range between 30 to 100 μm. This is the range currently used by the MicroMEGAS detectors.

4.2.2 Gas Electron Multiplier (GEM)

The GEM was invented by F.Sauli in 1997 [33]. The GEM is a sheet of insulating polyimide sandwiched between copper electrodes, approximately 100 μm thick, which amplifies electrons to a readable charge amplitude. Figure. 4.5 shows the photograph of the surface of GEM [34]. By applying a high voltage of a few 100 V between the two copper electrodes of the GEM, a high electric field is created in the GEM hole, which amplifies the seed electrons by causing an electron avalanche in the hole. The ionisation electrons are further accelerated and collide with other molecules, causing a chain reaction in which further electrons are generated. This avalanche phenomenon is also known as a Townsend discharge. An example of a electric field configuration in a GEM hole and electron avalanche are shown in Figures. 4.6 [34].

Ion Back Flow

In this electron avalanche process, positive ions are produced together with the ionisation electrons. Since ions have the opposite charge and much larger mass than the electrons, they slowly drift backwards in the drift volume, with a drift velocity O(1000) times smaller than that of electrons.

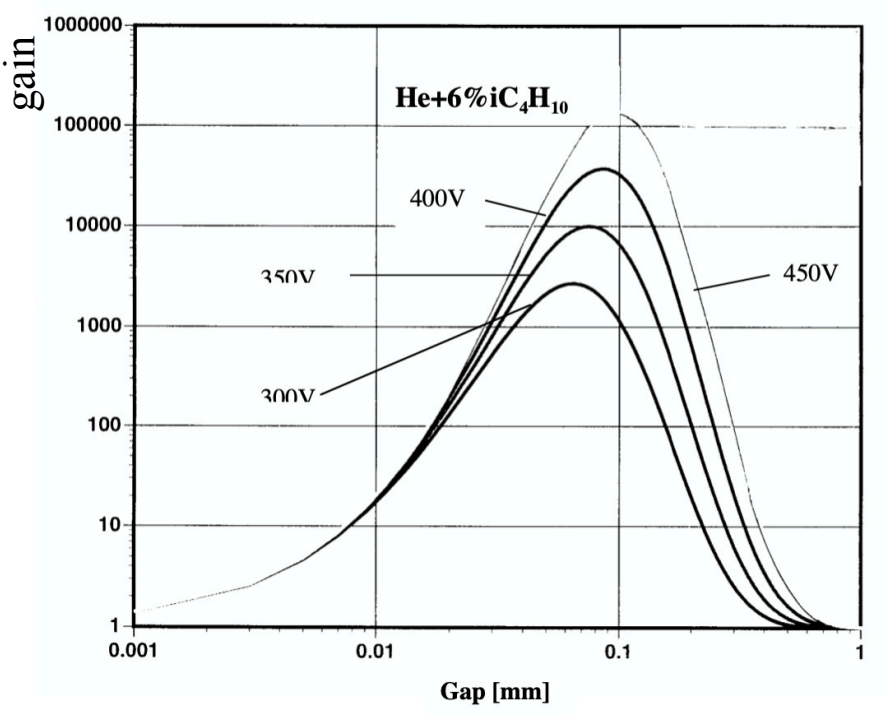

Figure 4.4: Calculated gas gain in the MicroMEGAS geometry.

The bunch structure of the ILC is shown in Fig. 4.7. A bunch train consists of 1312 bunches spaced over less than a ms, repeated at 5 Hz. The tracks produced within a single train will give rise to a disk of secondary ions produced in the gas amplifier, which slowly drift through the whole TPC volume. Given the 5 Hz repetition rate and the ion drift velocity, three such ion disks are present within the TPC volume. These positive ion disks distort the electric field in the TPC,

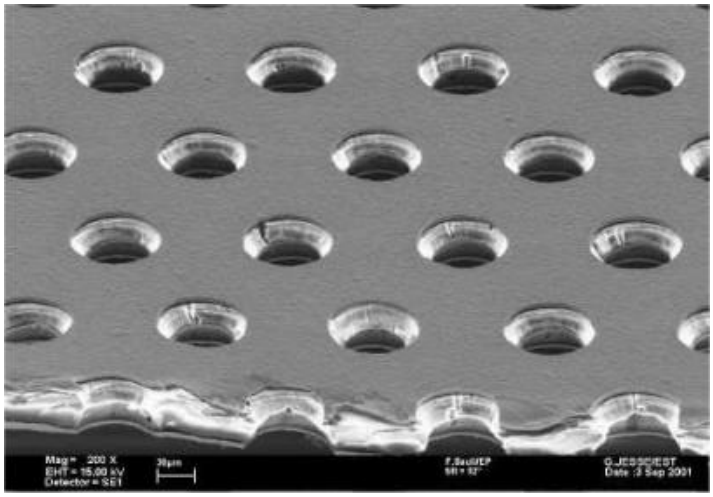

Figure 4.5: Photograph of the GEM surface.

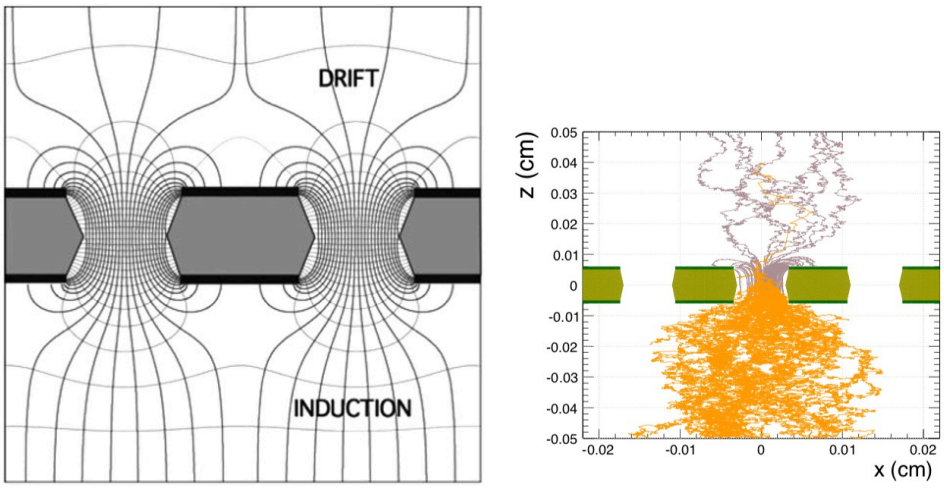

Figure 4.6: The electric field structure in the GEM hole (left) and a simulated electron avalanche in a GEM geometry using Garfield++ (right).

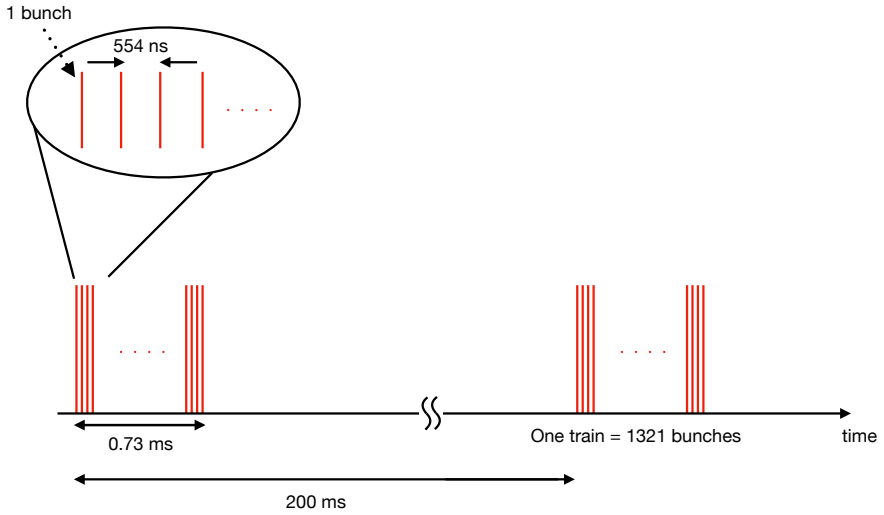

Figure 4.7: ILC bunch structure.

deviate the path of drifting ionisation electrons, and thus deteriorate the spatial resolution. A gating device can be used to block the majority of these secondary ions from the drift volume, minimising the size of these distortions.

The distortion of the electric field inside TPC due to the three ion disks is estimated to be 60 μm, so this effect cannot be neglected in order to achieve the required spatial resolution of 100 μm in $r\phi$. Therefore these positive ions have to be neutralised during the 200 ms between crossings. Simulation study have shown that a gating system is necessary to achieve the momentum resolution requirements at the nominal operating conditions of the ILC.

Gating system

To solve the Ion back flow problem, a large aperture gating device with a GEM-like structure has been developed [35]. Unlike a GEM, this gating device functions as an electron transmission film without the function of gas amplification. It is about 25 μm thick and has a honeycomb structure of about 300 μm wide

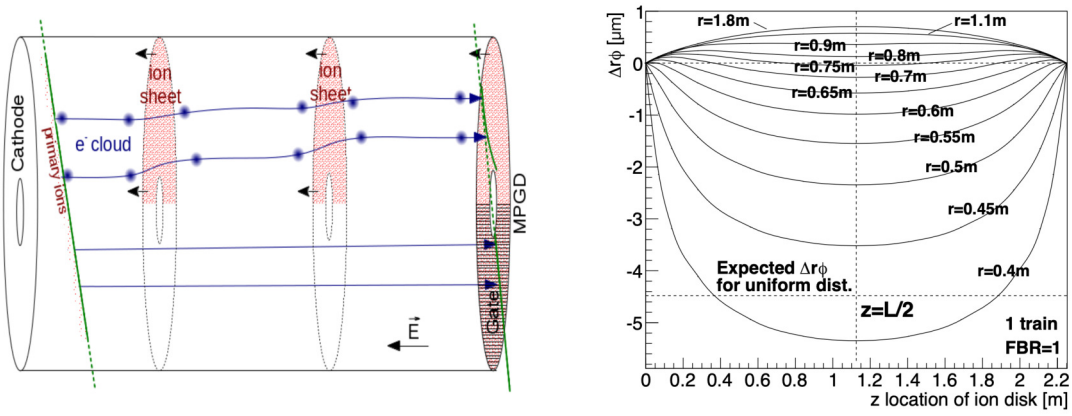

Figure 4.8: (Left) Distortion of electric field lines. (Right) Estimated deterioration in $r\phi$ resolution.

holes. The optical aperture of the gating device is about 80 %, which corresponds to a spatial resolution degradation O(10%) in the ILD-TPC nominal electric field configuration. In ILD-TPC, motion of electrons is strongly restricted in the direction of the magnetic field of 3.5 T and the operation in a gas with a high mean free time (τ) of drift electrons due to collisions with gas molecules. High optical transparency is therefore required for the gating device to ensure high electron transmission rate. By inverting the electric field it can easily be used as a closed gate. Figures. 4.9 and 4.10 show the electric field lines when the gating device is open and closed.

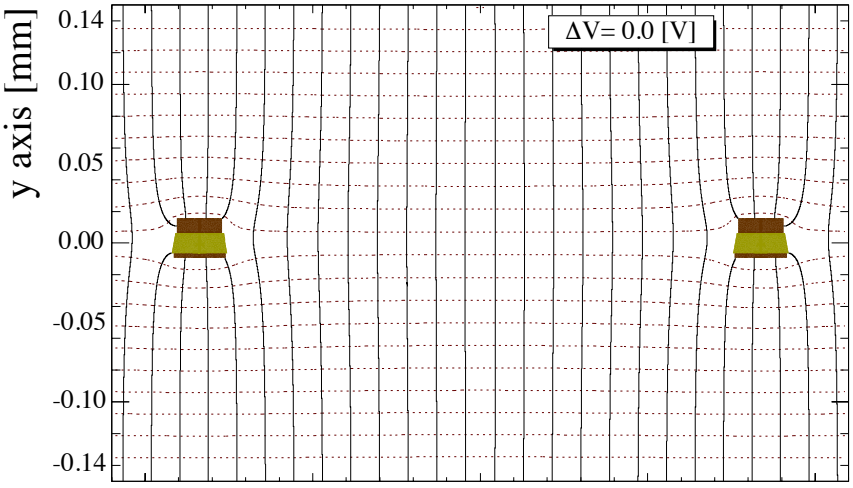

Figure 4.9: electric field: Open gate

Asian GEM readout module

Research groups in Japan are developing a GEM-based module for TPC readout, known as "Asian GEM", in the context of the international LC-TPC collaboration. The Asian GEM is a 100 μm thick sheet of polyimide and it has 70 μm diameter holes with 140 μm pitch. Figure. 4.11 shows the photograph of our Asian GEM sheet.

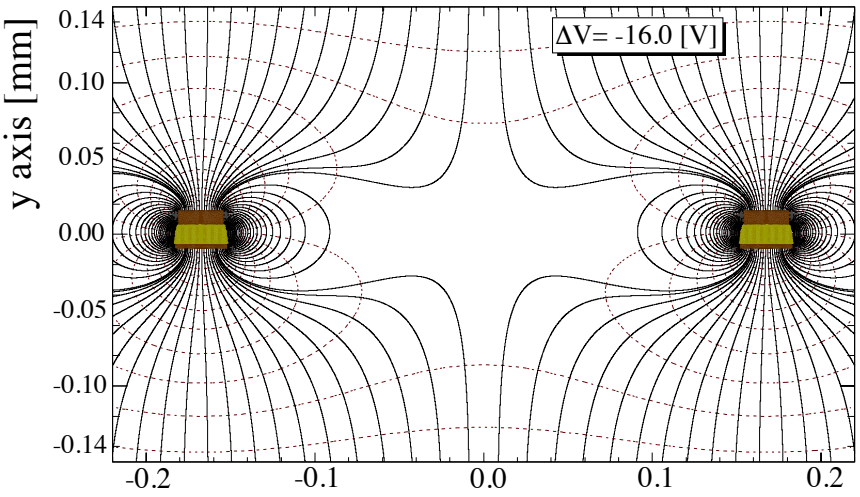

Figure 4.10: electric field: Closed gate

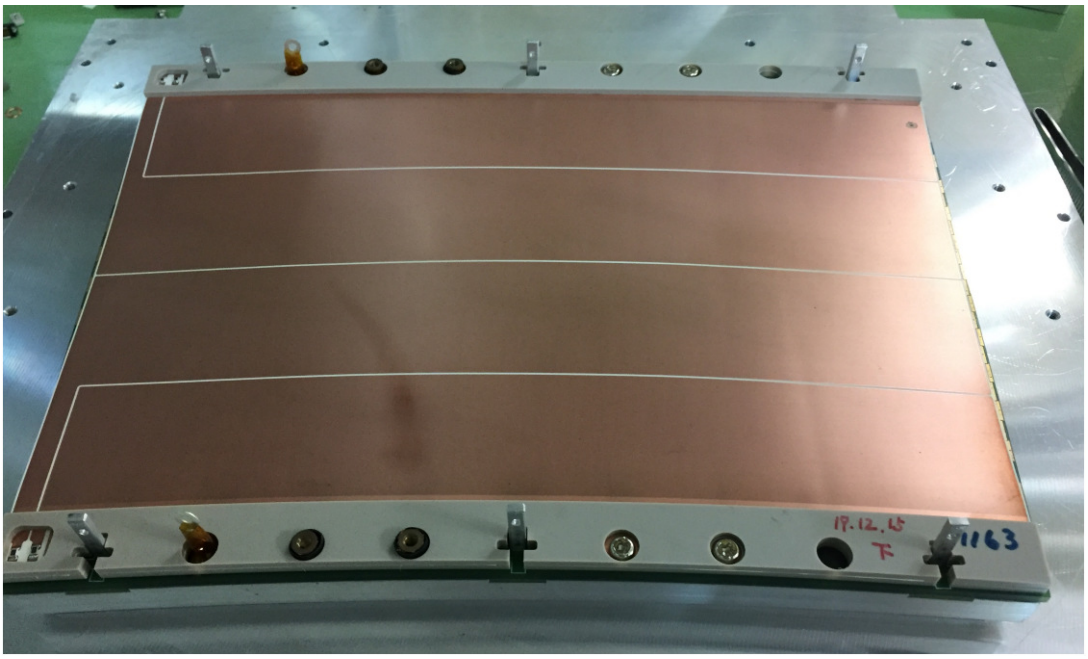

Figure 4.11: The photograph of our Asian GEM sheet.

Tests of the Asian GEM module have highlighted several points which should be improved in order to achieve an efficient, stable and robust detector. The gas gain across a module shows a significant non-uniformity, and spontaneous discharge of the GEM is observed.

Gas gain uniformity

Gas gain measurements have previously been performed across the entire surface of an Asian GEM prototype module using a ^{55}Fe source in long-term tests of the module [36]. As gas gain measurements are strongly dependent on environment conditions (temperature, pressure, humidity, etc.), care was taken to account for such variations by comparing the gain to a continuously monitored fixed

reference point. a single point on the GEM sheet was set as a reference point, measurements were performed over a long period of time and if the gas gain at this reference point varied with time, this value was used to correct the overall gain value. The results are shown in Figure. 4.12 [36]. A large gas gain non-uniformity was observed over the GEM sheet area, with variations of several 10s of percent.

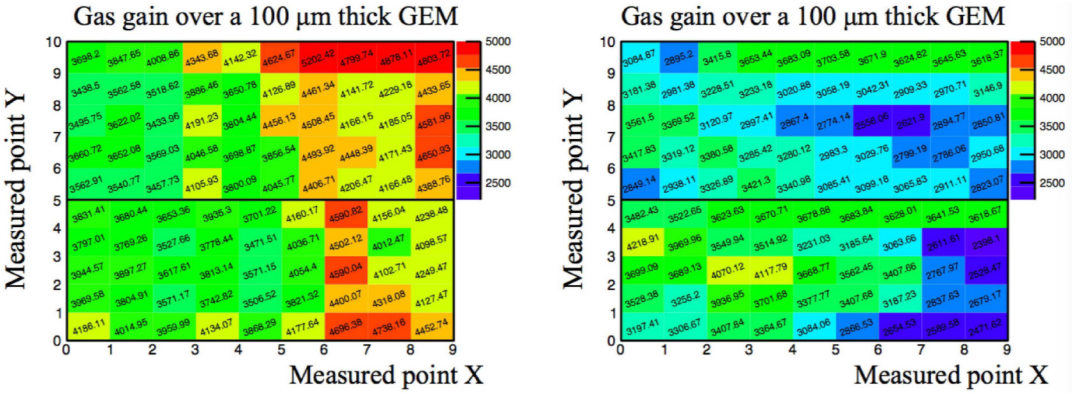

Figure 4.12: Gas gain uniformity for 2 kinds of samples of 100 μm thick GEM.

Such a significant variation in gain can be a problem. If the gas gain depends on the location within a module, a rather high voltage must be applied to obtain a sufficiently large signal in the regions with low gas gain region (e.g. the area to the left of the Figure. 4.13). On the other hand, locations with high gas gain (such as the area to the right of the Figure. 4.13), the avalanche will become very large, increasing the possibility of discharge as well as increasing the number of positive ions. To achieve a GEM readout module with limited discharge rate and sufficient gain over the whole surface, we should reduce such variations in gas gain. GEM modules with uniform characteristics will be easier to operate, calibrate and analyse in the context of a physics experiment, leading to improved performance and reduced danger of systematic effects.

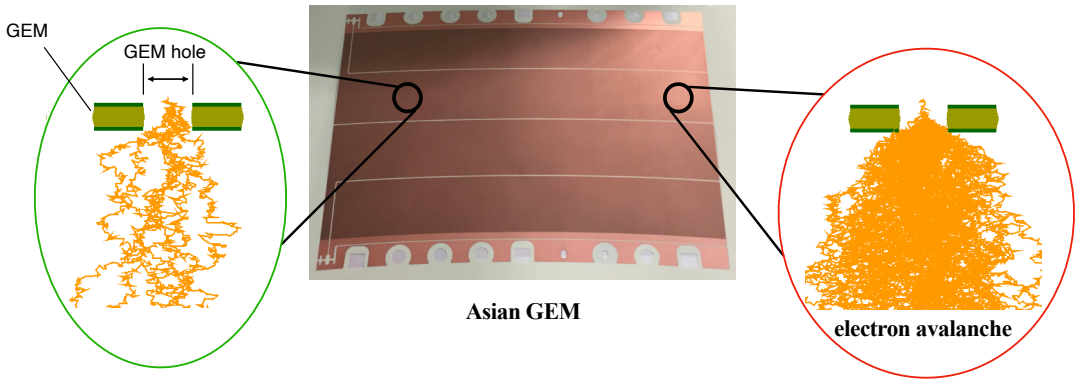

Figure 4.13: An example image of the problem with thickness dependence of GEM.

Why does the gas gain vary across the GEM surface? Several potential

contributions can be listed: foil thickness, gas circulation, HV supply, hole geometry, and so on. The major contribution to gas gain variations is likely due to variations in the thickness of the GEM foil.

We have already seen in Fig. 4.4 that small variations in micromegas gap thickness can give rise to large changes in gain, but also that there exists a range of gap widths, around the gain maximum, at which the dependence on gain on small gap variations becomes small.

4.3 Theoretical description of GEM amplification

The work presented in this thesis is an attempt to understand whether there exists a configuration for GEM devices for which the dependence on GEM thickness is zero to first order. We first survey the theoretical description of the processes which occur in the gas amplification process.

4.3.1 Gas amplification

In this section we derive the dependence of gas gain in an ideal parallel plate geometry on variations in pressure and electric field.

Consider an electron in a strong electric field. The electron is accelerated by the field, increasing its energy. The electron may collide with and ionise a gas molecule, producing additional ionisation electrons. The probability that this process occurs in unit length is called the "first Townsend coefficient", α.

Defining σ, ds and ρ as respectively the collision cross section between electrons and gas molecules, an infinitesimal element of length, and the ion number density, the increase of the number of electrons dN in a path of length ds can be expressed as

$$dN = N\rho\sigma\ ds \tag{4.1}$$

$$= N\alpha\ ds \tag{4.2}$$

where we define $\alpha = \rho\sigma$. The dimension of the Townsend coefficient is inverse length.

From the Boltzmann equation, σ depends on the distribution of electron energy $\sigma([f(\epsilon)])$ and the distribution of electron energy is proportional to E/ρ. Therefore, the dependence of the Townsend coefficient on the value of the electric field E (V/cm^{-1}) and the density of the gas ρ (Torr) should have the form

$$\frac{\alpha}{p} = f(E/\rho) \tag{4.3}$$

The Townsend coefficient is determined by the cross section of ionisation and excitation collisions, which is a function of two scaling variables: the ratio of electric field to gas density E/ρ and the magnetic field strength to gas density B/ρ.

gain vs pressure

If the temperature T is constant, from the ideal gas law, the relationship of the form

$$\frac{p}{p_0} \propto \frac{\frac{1}{V}}{\frac{1}{V_0}} \propto \frac{\rho}{\rho_0} \tag{4.4}$$

Then collecting things together, the Townsend coefficient should be proportional to the gas density

$$\alpha = \alpha_0 \left(\frac{E}{\rho}, \frac{B}{\rho}\right) \cdot \frac{\rho}{\rho_0} \tag{4.5}$$

The average gas gain is defined as

$$\bar{G} \coloneqq \frac{N}{\bar{N}} = exp\left[\int_B^A ds\ \alpha(E(s))\right] \tag{4.6}$$

where $\bar{N}$ is the average increase of number of electrons. The average gas gain depends on the path along which the avalanche develops. If a magnetic field is applied parallel to the electric field, as is the case in the ILD TPC, it will not affect the longitudinal motion, and its effect on the Townsend coefficient can be ignored.
The Townsend coefficient can then be written

$$\alpha = \alpha_0 \left(\frac{E}{\rho}\right) \cdot \frac{\rho}{\rho_0} \tag{4.7}$$

rewrite this to

$$\alpha = \alpha_0 \left(\hat{\mathbf{E}}_{\mathbf{0}}(\mathbf{x}) \cdot \frac{\mathbf{E}(\mathbf{x})}{\rho}\right) \cdot \frac{\rho}{\rho_0} \tag{4.8}$$

where $\hat{\mathbf{E}}_{\mathbf{0}} = \frac{\mathbf{E_0(x)}}{|\mathbf{E_0(x)}|}$ is a unit vector of reference electric field of $\mathbf{E_0}$.
Let's assume the change of the applied high voltage causes the variation of the electric field which satisfies

$$\frac{\mathrm{E(x)}}{\mathrm{E_0(x)}} = \frac{V}{V_0} \tag{4.9}$$

If we change the applied high voltage, the electric field uniformly will be scaled up/down. Then, Eq. 4.8 will be the form of

$$\alpha = \alpha_0 \left(\frac{\mathrm{E_0(x)}}{V_0} \cdot \frac{V}{\rho}\right) \cdot \frac{\rho}{\rho_0} \tag{4.10}$$

Define the scaling variable of $X \coloneqq \frac{V}{\rho}$ and rewrite the above formula

$$\alpha = \alpha_0 \left(\frac{\mathrm{E_0(x)}}{V_0} \cdot X\right) \cdot \frac{\rho}{\rho_0} \tag{4.11}$$

Putting Eq. 4.11 into Eq. 4.6, we have

$$\bar{G} = exp\left[\int_B^A ds\ \alpha_0 \left(\frac{\mathrm{E_0(x)}}{V_0} \cdot X\right) \cdot \frac{\rho}{\rho_0}\right] \tag{4.12}$$

Take the logarithm of both sides of above equation, we find

$$\ln \bar{G} = \int_B^A ds\ \alpha_0 \left(\frac{\mathrm{E_0(x)}}{V_0} \cdot X\right) \cdot \frac{\rho}{\rho_0} \tag{4.13}$$

By performing Taylor expansion around X_0, ρ_0, the change of gas gain with the variation of X, ρ will be form of

$$\begin{aligned}
\frac{\Delta\bar{G}}{G} &\simeq \left[\int_B^A ds\ \left\{\frac{\partial}{\partial X_0}\alpha_0 \left(\frac{\mathbf{E_0(x)}}{V_0} \cdot X_0\right)\right\} X_0\right] \cdot \Delta\left(\frac{X}{X_0}\right) \\
&\qquad + \left[\int_B^A ds\ \alpha_0 \left(\frac{\mathrm{E_0(x)}}{V_0} \cdot X_0\right)\right] \cdot \Delta\left(\frac{\rho}{\rho_0}\right) \\
&= \left[\int_B^A ds\ \left\{\frac{\partial}{\partial X_0}\alpha_0 \left(\frac{\mathrm{E_0(x)}}{V_0} \cdot X_0\right)\right\} X_0\right] \cdot \Delta\left(\frac{X}{X_0}\right) + \ln \bar{G}_0 \cdot \Delta\left(\frac{\rho}{\rho_0}\right),
\end{aligned}$$

where

$$\ln \bar{G}_0 \coloneqq \int_B^A ds\ \alpha_0 \left(\frac{\mathrm{E_0(x)}}{V_0} \cdot X_0 \right) \tag{4.14}$$

and

$$\left. \frac{\partial \ln \tilde{G}}{\partial (X/X_0)} \right|_{X=X_0} = \left[\int_B^A ds\ \left\{ \frac{\partial}{\partial X_0} \alpha_0 \left(\frac{\mathrm{E_0(x)}}{V_0} \cdot X_0 \right) \right\} X_0 \right] \tag{4.15}$$

By measuring the high voltage curve, $\ln \bar{G}_0$ can be experimentally determined. The scaling variable X depends on the high voltage V and the gas density ρ. Then if the high voltage is fixed, the dependence of X will be

$$\Delta \left(\frac{X}{X_0} \right) = -\Delta \left(\frac{\rho}{\rho_0} \right) \tag{4.16}$$

Therefore we have,

$$\frac{\Delta \tilde{G}}{\tilde{G}} \approx - \left[\left. \frac{\partial \ln \tilde{G}}{\partial (V/V_0)} \right|_{V=V_0} - \ln \tilde{G}_0 \right] \Delta \left(\frac{\rho}{\rho_0} \right) \tag{4.17}$$

4.3.2 Penning effect

An additional gas amplification effect we should pay particular attention to is the "Penning effect" [37], which can result in a gas gain which far exceeds that calculated using only the Townsend coefficient. The Penning effect occurs when a gas-B with a low ionisation potential is added to a gas-A that has an excited state energy higher than the ionisation energy of gas-B. De-excitation of gas-A can then ionise gas-B:

$$A^* + B \rightarrow A + B^+ + e^- \tag{4.18}$$

From the discussion above, the gas gain G has the form

$$G = exp \int dx\ \alpha(x) \tag{4.19}$$

Taking account of the Penning effect, the Townsend coefficient will be modified to

$$\alpha(x) = \alpha_0(x) \left(\frac{\Sigma_i r_{exc,i} + \Sigma_i r_{ion,i}}{\Sigma_i r_{ion,i}} \right) \tag{4.20}$$

where $r_{exc,i}$ is the rate at which the excitation energy of excited level i exceeds the ionization potential of the gas mixture, and $r_{ion,i}$ is the rate of an ionisation level i.
Then

$$\begin{aligned} \alpha(x) &= \alpha_0(x) \left(\frac{\Sigma_i r_{exc,i} + \Sigma_i r_{ion,i}}{\Sigma_i r_{ion,i}} \right) \\ &= \alpha_0(x)\,(1 + r) \end{aligned} \tag{4.21}$$

where $r \equiv \frac{\Sigma_i r_{exc,i}}{\Sigma_i r_{ion,i}}$ is called the Penning transfer rate. Putting Eq. 4.21 into Eq. 4.19, we obtain

$$G = exp \left[(1 + r) \int\ dx\ \alpha_0(x) \right] \tag{4.22}$$

and the additional gas gain is accounted for by this Penning transformation of the excitation energy.

4.3.3 Thickness dependence of Gas gain

The probability per unit length that a seed electron in a strong electric field produces an additional ionised electron is called the first Townsend coefficient α. The average increase in electrons dN on the pathway ds can be written as

$$dN = N\alpha ds \tag{4.23}$$

The Townsend coefficient is determined by the cross sections of ionisation and excitation collisions that lead to secondary ionisation. These cross sections are a function of the electron velocity, or energy, and then a function of two scaling variables: $E/$(gas density) and $B/$(gas density) as far as the t- and x-derivatives of the electron state density function on the left-hand side of the Boltzmann equation can be ignored.
The Townsend coefficient with inverse length dimension should then be proportional to the inverse of the mean free path and thus to the gas density:

$$\alpha = \alpha_0 \left(\frac{\boldsymbol{E}}{\rho}, \frac{\boldsymbol{B}}{\rho} \right) \cdot \frac{\rho}{\rho_0} \tag{4.24}$$

However, this is not the case for a strong electric field gradient, in which case $f(v; x)$ on the left-hand side of Boltzmann equation varies significantly over a few mean free paths. Assuming this condition, the average gas gain can be written as a line integral

$$\bar{G} := \frac{N}{N_0} = \exp\left[\int_A^B ds\alpha(E(s)) \right] \tag{4.25}$$

This generally depends on the possible path along which the avalanche develops.

This equation can be used to calculate the average gas gain if the first Townsend coefficient is given as a function of the electric field. When the electric fields and magnetic fields are parallel, the effect of the magnetic fields on the Townsend coefficient can be ignored, since longitudinal motion is not affected by the magnetic fields. Considering a uniform electric field E in an amplification gap of width Δ spanned by a voltage V, we can write the average gain as

$$\bar{G}(\Delta) = \exp\left[\alpha \left(\frac{V}{\Delta} \right) \Delta \right] \tag{4.26}$$

(assuming parallel electric magnetic fields). This should be a good approximation, in the case of GEM and MicroMEGAS. Note that the Townsend coefficient increases with the electric field. If the electric field strength is held constant, the gas gain increases with the gap width. However, as the gap increases, the electric field decreases. This indicates that the gas gain should be maximum at the appropriate gap value and be stable around that value with respect to gap variation. In this study, we call the condition in which the gas gain is maximum and constant with respect to the gap the "Stability condition". The purpose of this study is to theoretically verify whether this "Stability condition" exists in GEM, which are candidates for amplifiers used in ILD-TPC, and to identify GEM with an optimal geometry.

4.3.4 Alkhazov's Theory

In this section we provide an overview of Alkhazov's theory for avalanche formation [38]. There are various mechanisms for electron avalanche formation, such as collision ionisation and the Penning and Jesse processes [39]. Since MPGD detectors usually use electric field strengths at which ionisation collision is dominant, other mechanisms are ignored.
Furthermore, a uniform electric field is assumed in the amplification region, and if there is a magnetic field it should be parallel to the electric field. This suppresses the $E \times B$ effect, which causes drift electrons to be deflected.

Figure 4.14 shows a cartoon of the amplification process. If $P(N;x)$ is the probability of obtaining N electrons at point x from the beginning of the amplification region, then it must satisfy the following self-consistency equation:

$$P(N;x) = \int_0^x dl\ p_i(l) \sum_{N'=1}^{N-1} P(N';x-l)P(N-N';x-l) \tag{4.27}$$

where $p_i(l)$ is the probability of the first ionising collision occurring at a distance l from the origin of the seed electron.

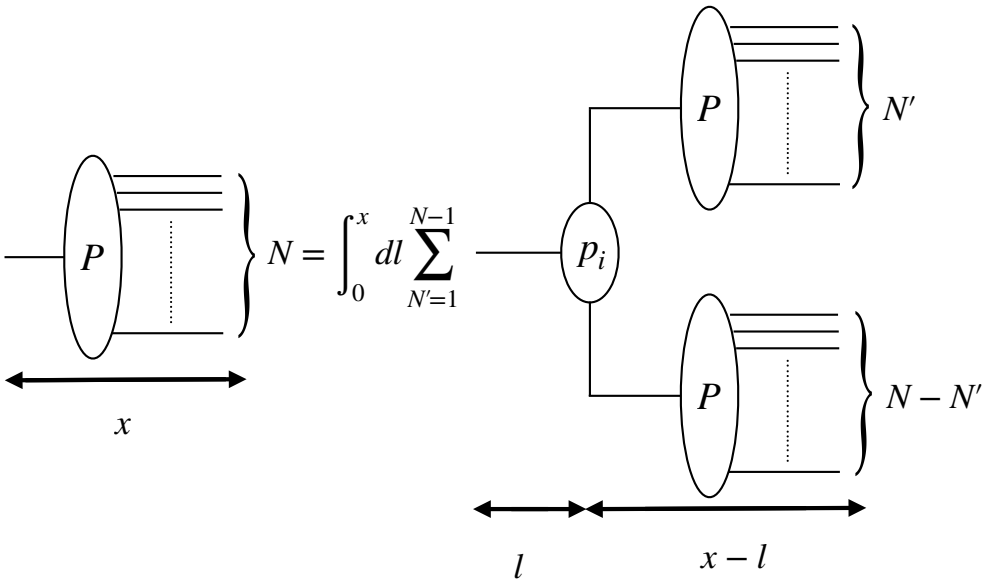

Figure 4.14: Schematic image of the amplification process

We now consider fluctuations which occur in the avalanche process. The avalanche fluctuation function is defined as

$$p(z,x) := \bar{N}(x)P(\bar{N}(x)z;x) \tag{4.28}$$

where $z = \frac{N}{\bar{N}(x)}$ and $\bar{N}(x)$ is the average number of electrons at distance x within the amplification region.
The n-th moment M_n of this fluctuation function can be written

$$\begin{aligned} M_n :&= \int_0^\infty dz\ z^n\ p(z,x) \\ &= \sum_{N=0}^{\infty} \frac{1}{\bar{N}(x)} \left(\frac{N}{\bar{N}(x)}\right)^n \bar{N}(x) P(N;x). \end{aligned} \tag{4.29}$$

Thanks to the central limit theorem, the avalanche fluctuation function and its moments are determined in the early stages of avalanche growth; at large x, $p(z,x)$ therefore no longer depends on x: $p(z,x) \to p(z)$, and $\bar{N}(x) \to e^{\alpha x}$.

Therefore, we can derive from Eq. 4.27, an equation for M_n can be expressed as follows (see Appendix 5.2 for its derivation):

$$M_n = \int_0^x dl\ p_i(l) e^{-n\alpha l} \sum_{k=0}^{n} \frac{n!}{k!(n-k)!} M_k M_{n-k} \tag{4.30}$$

which leads to the recursion

$$M_n = \sum_{k=1}^{n-1} \frac{n!}{k!(n-k)!} \frac{M_k M_{n-k} J(n)}{1 - 2J(n)} \tag{4.31}$$

where

$$J(n) := \int_0^\infty dl\ p_i(l) e^{-n\alpha l} \tag{4.32}$$

which is determined by the probability of the first ionising collision $p_i(l)$. From Eq. 4.30, we have

$$M_0 = M_1 = 1 \tag{4.33}$$

which leads to the following relation regarding the first Townsend coefficient:

$$2J(1) = 2 \int_0^\infty dl\ p_i(l)\ e^{-\alpha l} = 1. \tag{4.34}$$

From the self-consistency equation 4.27, we find

$$p(z) = \frac{1}{\alpha z} \int_z^\infty dz' \int_0^{z'} dz'' p(z'') p(z' - z'') p_i(\frac{1}{\alpha} \ln \frac{z'}{z}) \tag{4.35}$$

An approximate solution can be obtained by using an equation for $p(z)$ and repeating the substitution and this equation implies that the behaviour at large l in $p_i(l)$ controls the behaviour of $p(z)$ around $z = 0$. In the limit of large l, an exponential shape is assumed

$$p_i(l) \to C e^{-al} \tag{4.36}$$

where C is a constant. Then, we have

$$p(z) \simeq z^{\frac{a}{\alpha}-1} \int_0^\infty dz' \int_0^{z'} dz''\ p(z'') p(z' - z'') \frac{C}{\alpha} z'^{-\frac{a}{\alpha}} \tag{4.37}$$

around $z = 0$. No specific form of $p_i(l)$, the probability of the first ionising collision, is specified in Alkhazov's theory.

This self-consistency equation for $p(z)$ implies that the behaviour of $p_i(l)$ at large l controls the behaviour of $p(z)$ around $z = 0$. Assume an exponential shape in the limit of large l:

$$p_i(l) \to Ce^{-al} \quad \text{as} \quad l \to \infty \tag{4.38}$$

where C is constant. Therefore, near $z = 0$, we have,

$$p(z) \simeq z^{\frac{a}{\alpha}-1} \int_0^\infty dz' \int_0^{z'} dz'' p(z' - z'') \frac{C}{\alpha} z'^{-a/\alpha} \tag{4.39}$$

Defining $\theta := \frac{a}{\alpha} - 1$ we obtain

$$p(z) \simeq C' z^\theta \tag{4.40}$$

where C' is constant.

In Alkhazov's theory $p_i(l)$ can be chosen by the user; we consider Legler's model, which we describe next.

4.3.5 Legler's model

In this section we describe Legler's model for the form of $p_i(l)$.

In Legler's model, ionisation collisions are assumed to occur only after seed electrons have traveled a certain minimum distance x_0 to obtain sufficient energy from the electric field to ionisation the gas: $x_0 := U_0/E$, where U_0 is the ionisation potential of the gas, and E the electric field strength. In Legler's model, the cross-section is assumed to be constant after exceeding the energy threshold required for ionisation (like the step function) shown in the Fig. 4.15. The probability of the first ionisation collision is then given by

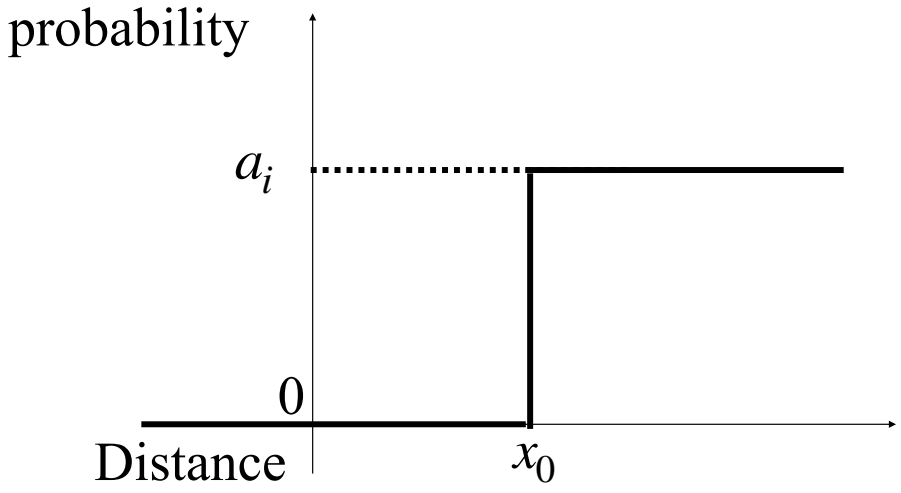

Figure 4.15: In Legler's model, any ionising collision is assumed to occur after the seed electron flying over a minimum distance x_0 sufficient to obtain from the electric field the energy required for ionisation. It is also assumed that the cross-section of ionising collision after the x_0 threshold is constant.

$$p_i(l) = a_i e^{-a_i(l-x_0)}\theta(l - x_0). \tag{4.41}$$

The relation $2J(1) = 1$ (Eqn. 4.34) leads to

$$a_i = \frac{\alpha}{2e^{-\alpha x_0} - 1}, \tag{4.42}$$

while from Eq. 4.30, the 2nd order moment is

$$M_2 = \frac{2J(2)}{1 - 2J(2)} \tag{4.43}$$

and its variance can be calculated as follows

$$\sigma^2 = M_2 - M_1 = M_2 - 1 = \frac{(2 - e^{\alpha x_0})^2}{2 - (2 - e^{\alpha x_0})^2} \tag{4.44}$$

From this Legler's model, we further assume that the electrons accelerate from rest to the first ionisation collision, so the probability of encountering the first ionisation collision at distance l is

$$p_i(l)dl = P\left(0,\ \int_0^l dl'\ n\sigma((V/\Delta)l')\right) \cdot P\left(1,\ \int_l^{l+dl} dl'\ n\sigma((V/\Delta)l')\right) \tag{4.45}$$

where the usual Poisson probability $P(k, \lambda) = \lambda^k e^{-\lambda}/k!$.

We evaluate these integrals as

$$\int_0^l dl'\ n\sigma((V/\Delta)l') = n\sigma_0(l - x_0)\theta(l - x_0) \tag{4.46}$$

and

$$\int_l^{(l+dl)} dl'\ n\sigma((V/\Delta)l') = n\sigma_0\theta(l - x_0)dl \tag{4.47}$$

with

$$x_0 := (U_0/V)\Delta. \tag{4.48}$$

Hence, we find

$$p_i(l) = e^{-n\sigma_0(l-x_0)} n\sigma_0\theta(l - x_0) \tag{4.49}$$

and comparing this equation with Eq. 4.42, a_i is expressed as

$$a_i = n\sigma_0 \tag{4.50}$$

and σ_0 is a kind of effective cross section, which generally depends on the distribution of electron energy or equivalently E/n, where n is the gas density.

By introducing the scaling variables

$$\eta := a_i x_0 = n\sigma_0 x_0 \tag{4.51}$$

$$\chi := \alpha x_0 \tag{4.52}$$

we rewrite Eq. 4.42 for the first Townsend coefficient as

$$\eta = \frac{\chi}{2e^{-\chi} - 1} \tag{4.53}$$

and the full gain as

$$\ln G = \alpha\Delta = \chi\delta, \tag{4.54}$$

where $\delta := \Delta/x_0 = V/U_0$ with $x_0 := (U_0/V)\Delta$.

By differentiating Eq. 4.54 with respect to some general variable X, we obtain

$$d\ln G = \frac{dG}{G} = \left[\left(\frac{\partial\chi}{\partial\eta}\right)\left(\frac{\partial\eta}{\partial X}\right)\delta + \chi\left(\frac{\partial\delta}{\partial X}\right)\right] X\left(\frac{dX}{X}\right) \tag{4.55}$$

$\frac{\partial\chi}{\partial\eta}$ is obtained by differentiating the logarithm of Eq. 4.53:

$$\begin{aligned}\frac{1}{\eta} &= \left[\frac{1}{\chi} + \frac{\eta}{\chi}2e^{-\chi}\right]\left(\frac{\partial\chi}{\partial\eta}\right)\\ &= \left[\frac{1}{\chi} + \frac{\eta}{\chi}\left(\frac{\chi}{\eta}+1\right)\right]\left(\frac{\partial\chi}{\partial\eta}\right)\\ &= \frac{1}{\chi}(1+\chi+\eta)\left(\frac{\partial\chi}{\partial\eta}\right)\end{aligned} \tag{4.56}$$

From Eq. 4.56, we find

$$\left(\frac{\partial\chi}{\partial\eta}\right) = \frac{\chi}{\eta(1+\chi+\eta)}, \tag{4.57}$$

which when inserted into Eq. 4.55 leads to

$$\frac{dG}{G} = \left[\left(\frac{1}{1+\chi+\eta}\right)\frac{1}{\eta}\left(\frac{\partial\eta}{\partial X}\right) + \frac{1}{\delta}\left(\frac{\partial\delta}{\partial X}\right)\right]\ \chi\delta X\left(\frac{dX}{X}\right) \tag{4.58}$$

with

$$\begin{aligned}\eta &= \sigma_0\left[\frac{V/\Delta}{n}\right]U_0\left(\frac{V/\Delta}{n}\right)^{-1}\\ \delta &= V/U_0\\ \chi &= \frac{\ln G}{\delta}.\end{aligned}$$

We can now use Eq. 4.58 to investigate the dependence of the gas gain G on different variables X. In the following we consider two cases, the gas density n and the gap width Δ.

Case 1: dependence on the gas density n

Start from

$$\begin{aligned}\eta &= n\sigma_0 x_0\\ &= n\sigma_0\frac{U_0}{V}\Delta\\ &= \sigma_0 U_0\frac{1}{\epsilon}\end{aligned} \tag{4.59}$$

with

$$\epsilon := \frac{E}{n} = \frac{V/\Delta}{n} \tag{4.60}$$

For some variables X is gas density n, we have

$$\frac{1}{\eta}\left(\frac{\partial\eta}{\partial n}\right) = \frac{1}{\eta}\left[\left(\frac{\partial\eta}{\partial n}\right) + \left(\frac{\partial\eta}{\partial\epsilon}\right)\left(\frac{\partial\epsilon}{\partial n}\right)\right] \tag{4.61}$$

Here, corresponding terms can be expressed as

$$\frac{1}{\eta}\frac{\partial\eta}{\partial n} = \frac{\sigma_0\frac{U_0}{V}\Delta}{n\sigma_0\frac{U_0}{V}\Delta} = \frac{1}{n}, \tag{4.62}$$

$$\frac{\partial\epsilon}{\partial n} = -\frac{V/\Delta}{n^2} = -\frac{\epsilon}{n}, \text{ and} \tag{4.63}$$

$$\frac{1}{\eta}\frac{\partial\eta}{\partial\epsilon} = \frac{1}{\eta}\left(\frac{\partial\eta}{\partial\sigma_0}\right)\left(\frac{\partial\sigma_0}{\partial\epsilon}\right). \tag{4.64}$$

In the Eq. 4.64, we find

$$\frac{1}{\eta}\left(\frac{\partial\eta}{\partial\sigma_0}\right) = \frac{\epsilon}{\sigma_0 U_0}\frac{U_0}{\epsilon} = \frac{1}{\sigma_0} \tag{4.65}$$

Therefore, putting them together, we arrive at

$$\begin{aligned}\frac{1}{\eta}\left(\frac{\partial\eta}{\partial n}\right) &= \left[\frac{1}{n} + \frac{1}{\sigma_0}\left(\frac{\partial\sigma_0}{\partial\epsilon}\right)\left(-\frac{\epsilon}{n}\right)\right] \\ &= \left[1 - \frac{\epsilon}{\sigma_0}\left(\frac{\partial\sigma_0}{\partial\epsilon}\right)\right]\frac{1}{n}\end{aligned} \tag{4.66}$$

and, hence, we obtain the gas density n dependence of gas gain G

$$\frac{dG}{G} = \left(\frac{1}{1+\chi+\eta}\right)\left[1 - \frac{\epsilon}{\sigma_0}\left(\frac{\partial\sigma_0}{\partial\epsilon}\right)\right]\chi\delta\left(\frac{dn}{n}\right). \tag{4.67}$$

Case 2: dependence on the gap width Δ

Similarly for $X = \Delta$,

$$\frac{1}{\eta}\left(\frac{\partial\eta}{\partial\Delta}\right) = \frac{1}{\sigma_0}\left(\frac{\partial\sigma_0}{\partial\epsilon}\right)\left(\frac{\partial\epsilon}{\partial\Delta}\right) + \frac{1}{\Delta} \tag{4.68}$$

and the gap Δ dependence of gas gain G is

$$\frac{dG}{G} = \left(\frac{1}{1+\chi+\eta}\right)\left[1 - \frac{\epsilon}{\sigma_0}\left(\frac{\partial\sigma_0}{\partial\epsilon}\right)\right]\chi\delta\left(\frac{d\Delta}{\Delta}\right). \tag{4.69}$$

We can see that gas gain is constant $\frac{dG}{G} = 0$ in both the above cases when

$$1 - \frac{\epsilon}{\sigma_0}\left(\frac{\partial\sigma_0}{\partial\epsilon}\right) = 0 \tag{4.70}$$

from which we obtain the "Stability condition'

$$\left(\frac{\partial\sigma_0}{\partial\epsilon}\right) = \frac{\sigma_0}{\epsilon}. \tag{4.71}$$

If this condition is satisfied the gas gain is insensitive to small changes of both the gap Δ and gas density n. Comparing the Eq. 4.58 and Eq. 4.69, we see that the gas gain is stabilised against changes in gap Δ if it is stabilised against changes in gas density n, and vice versa.

4.4 Simulation setup

The validity of the theory discussed in the previous section was the verified using the simulation software Garfield++. Although it is possible to simulate gas amplification process using Garfield++ alone, simulations can also be performed by loading the electric field calculated by an external programme. The latter method is recommended when simulating detectors with complex electric field structures such as exist in a GEM. In this study, Gmsh was used to create the mesh and Elmer software was used to calculate the electric field, and the resulting field was loaded into Garfield++ for simulation. We here give a brief description of the software tools used.

4.4.1 Garfield++

Garfield++ is a toolkit for the detailed simulation of gas detectors, and consisting of components including Heed [40]. The drift of electrons and ions in gases under the influence of electric and magnetic fields is simulated. From a microscopic point of view, the macroscopic transport parameters of these electrons (drift velocity, diffusion coefficient, Townsend coefficient, attachment coefficient, etc.) are determined by the cross sections of electron scattering by atoms and molecules. Garfield++ interfaces with Magboltz and uses its cross–section library to calculate accurate transport parameters. The main phenomena that can occur in the charge transport process include elastic and inelastic scattering, ionisation, attachment, and excitation.

4.4.2 Magboltz

Magboltz is a software tool widely used for modeling electron motion in gas detectors [41]. For Garfield++ simulations, macroscopic parameters such as the Townsend coefficient, electron/ion attachment coefficient, drift velocity and diffusion constant in a gas under certain electric and magnetic fields are calculated by Magboltz. Magboltz calculates electron swarm parameters by solving the Boltzmann equation (transport equation) on the basis of elastic scattering, ionisation and excitation cross sections of electrons and gas molecules.

4.4.3 Gmsh

Gmsh is a software for the finite element method [42] which allows pre-processing, such as the creation of two- or three-dimensional meshes, and post-processing, such as the visualisation of the analysis data. Gmsh was used to describe the geometry of the GEM and parallel plate and to create the mesh. The mesh file created here was loaded into Elmer.

4.4.4 Elmer

Elmer is a finite element software for solving partial differential equations [43]. Its ability to handle a very large variety of equations and to couple equations in a general form makes it a versatile tool for multiphysical simulations. Using this software, the potential of the surface and the dielectric constant of the solid

were set and the electric field created in the GEM geometry was calculated. The electric field calculated here was loaded into Garfield++ for simulation.

4.5 Comparison with experimental data

First, in order to investigate whether Garfield++ can reproduce the experimental data, the experimental gas gain results of the Glass GEM and the MicroMEGAS with P10 gas (a mixture of Argon, CH4 in the 90/10 concentrations) and T2K gas were compared with the simulation results.

4.5.1 Glass GEM

Figure. 4.16 shows the measured gas gain curves for the P10 gas from the previous study [44]. The red line corresponds to the P10 gas. The geometry and the photograph of Glass GEM are shown in Table. 4.1 and Fig. 4.17.

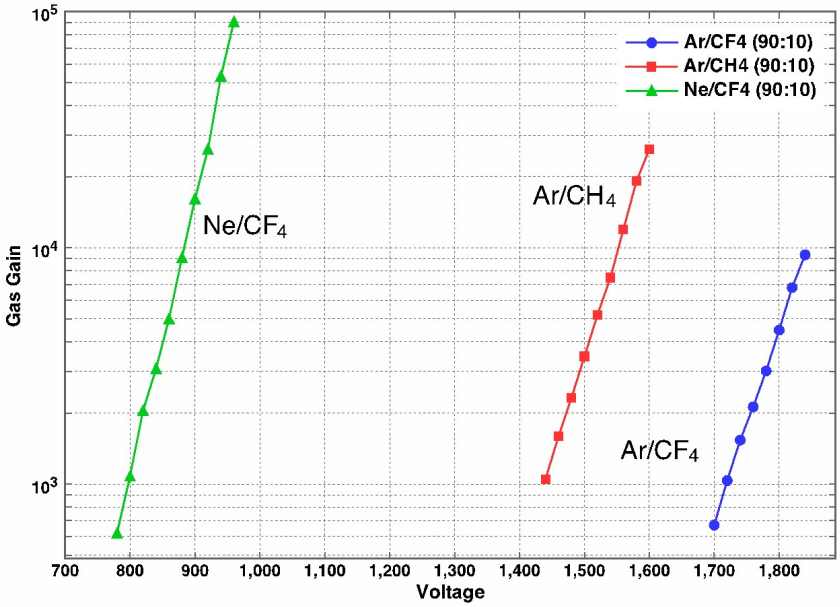

Figure 4.16: Measured gas gain curves of Glass GEM.

Table 4.1: Geometry of Glass GEM

Hole diameter	170 μm
Pitch	280 μm
Thickness	680 μm
Sensitive area	100 mm $\times$ 100 mm

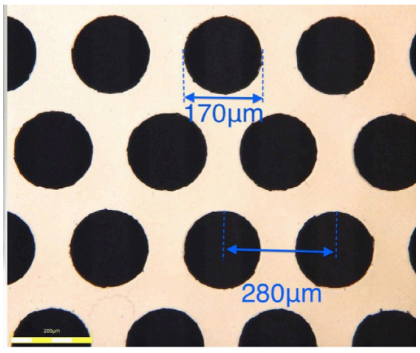

Figure 4.17: Photograph of Glass GEM

Then, we performed the simulations with applied high voltages of 1400, 1450, 1500, and 1550 V at 750 Torr. Figure. 4.18 shows the comparison of the gas gain curve between Garfield++ simulation result and the measured gas gain. In

order to adjust to reproduce the experimental data, the Penning transfer rate of $r = 0.18$ was used and its measured value is is $r = 0.212 \pm 0.002$ at 760 Torr [45]. The result of Garfield++ simulation and the measured gas gain is in good agreement considering the pressure difference.

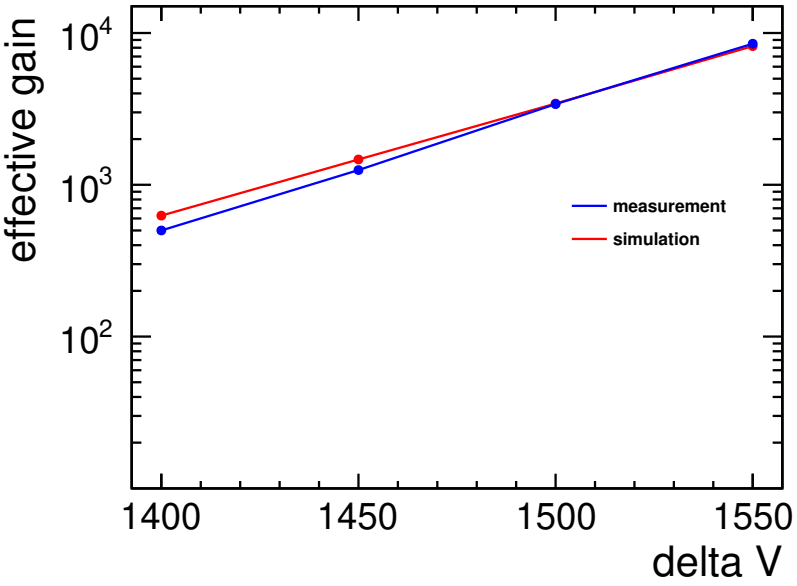

Figure 4.18: Comparison of gas gain curve of Glass GEM for the P10 gas. The blue line is the result of the previous study and the red line is the result of Garfield++ simulation. The Penning transfer rate of $r = 0.18$ was used to reproduce the result of the previous measurement.

4.5.2 MicroMEGAS

Figure. 4.19 shows the measured gas gain curves of the MicroMEGAS for the T2K gas from the previous study [46]. The geometry of MicroMEGAS is the wire pitch of 59 μm, the amplification gap of 128 μm, and the 12 pillars per pad with a diameter of 0.5 mm.

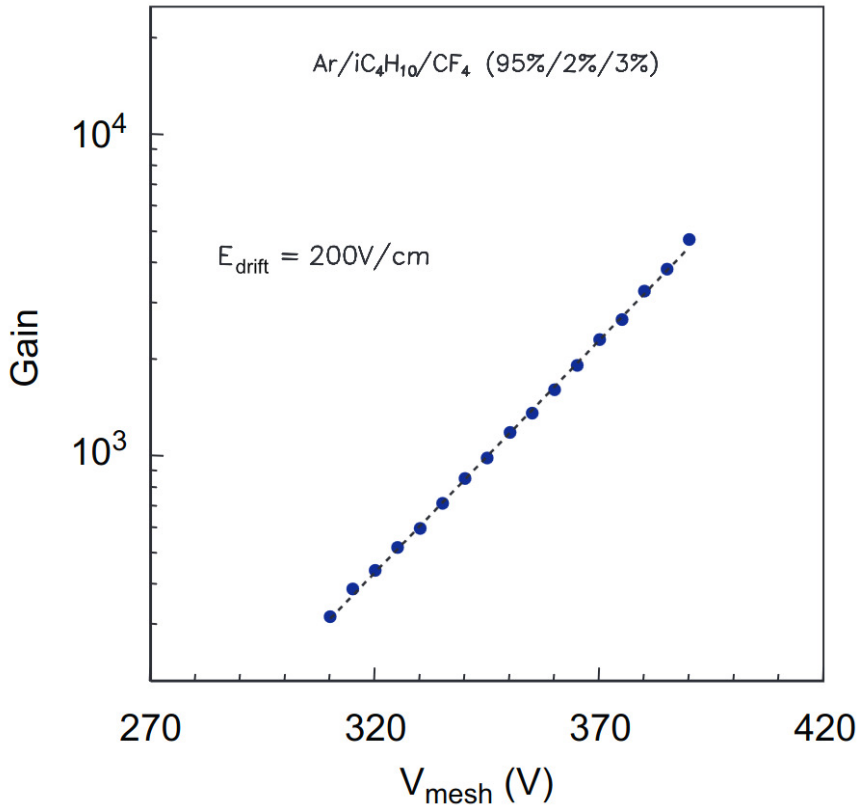

Figure 4.19: Measured gas gain curves of MicroMEGAS.

We performed the simulations with applied high voltages of 310 to 390 V at 760 Torr. Figure. 4.20 shows the comparison of the gas gain curve between Garfield++ simulation result and the measured gas gain. The Penning transfer rate of $r = 0.34$ was used. The corresponding measured value is $r = 0.40 \pm 0.01$ at 760 Torr [45]. This value is not exactly the same as T2K, but is considered approximately equal as it is a mixture of iso-butane and Ar gases that contribute to penning effect. The result of Garfield++ simulation and the measured gas gain is in good agreement considering this difference.

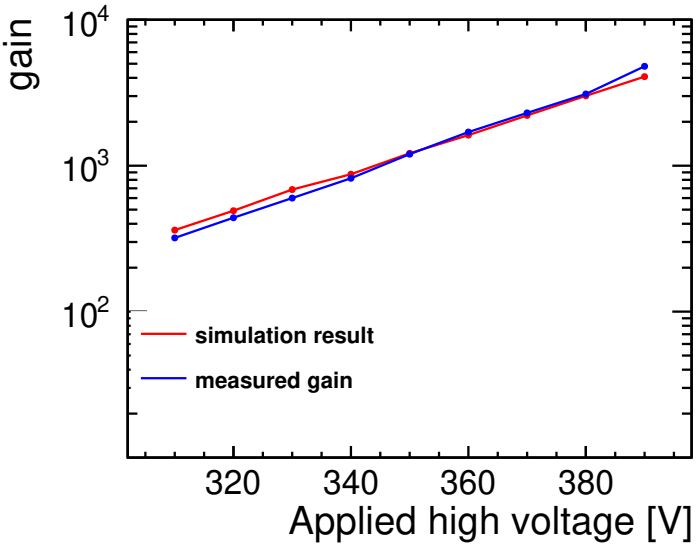

Figure 4.20: Comparison of gas gain curve of MicroMEGAS for the T2K gas. The blue line is the result of the previous study and the red line is the result of Garfield++ simulation. The Penning transfer rate of $r = 0.34$ was used to reproduce the result of the previous measurement.

Comparison of measured data with Garfield++ using the Glass GEM and the MicroMEGAS confirms that Garfield++ reproduces the experimental data very well. Therefore, verification of theory will be performed in the following section using Garfield++.

4.6 Verification of theory

In this section we describe simulations performed using the above tools to investigate the stability condition theoretically predicted in Sec. 4.3. All simulations were carried out at a pressure of 1 atm (760 bar), a temperature of 273.15 K and zero magnetic field.

4.6.1 Parallel plate geometry

First, it was verified whether a stability point (a region where the gas gain is almost constant with respect to changes in the gap) can be found in the dependence of the gas gain on the gap size in a simple parallel plate geometry, and whether the stability condition derived from Alkhazov's theory–Legler's model is consistent with this stability point.

The simulated gas gain when the parallel plate gap was changed from 10 μm to 100 μm is shown in Fig. 4.21 with voltage of 350 V. A stability region can be seen around 20 μm, the area corresponding to an electric field strength of about ~ 175 kV/cm.

Eq. 4.71 predicts that the function describing the dependence of the cross-section σ_0 on the scaled electric field strength $\frac{E}{n}$ should intersect with its own first derivative function at the stability point.
Garfield++ was used to calculate the mean free path l of electrons within the

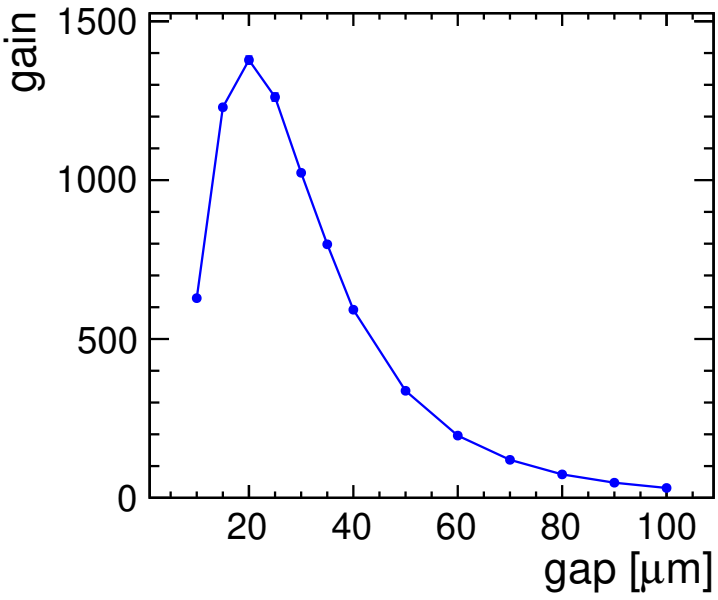

Figure 4.21: Gap dependence of gas gain in the case of a parallel plate geometry, T2K gas, and voltage of 350 V.

gas as a function of the electric field strength E, which was the used to derive the corresponding cross–section $\sigma_0 = 1/(nl)$. Figure. 4.22 shows the dependence of the inverse free–path $1/l$ on the electric field strength E, in the assumption $n = 1$.

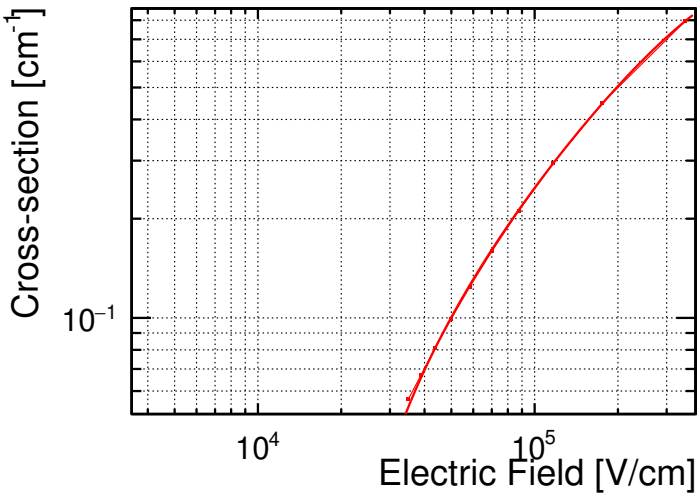

Figure 4.22: The cross-section σ_0 as a function of ϵ in the case of parallel plate geometry and voltage of 350 V. This figure actually shows how the inverse mean free-path in μm depends on the E-field in the case $n = 1$.

In Fig. 4.23, the black line shows the ratio σ_0/ϵ, and the red line its differential.The intersection point occurs at around 158 kV/cm, which corresponds to the gap of parallel plate of about 22 μm. We found that consistent within 10% in this relatively low electric field case where electrons would be thermal

after ionisation. The slight difference could be attributed to Legler's model's over-simplified cross-section shape.

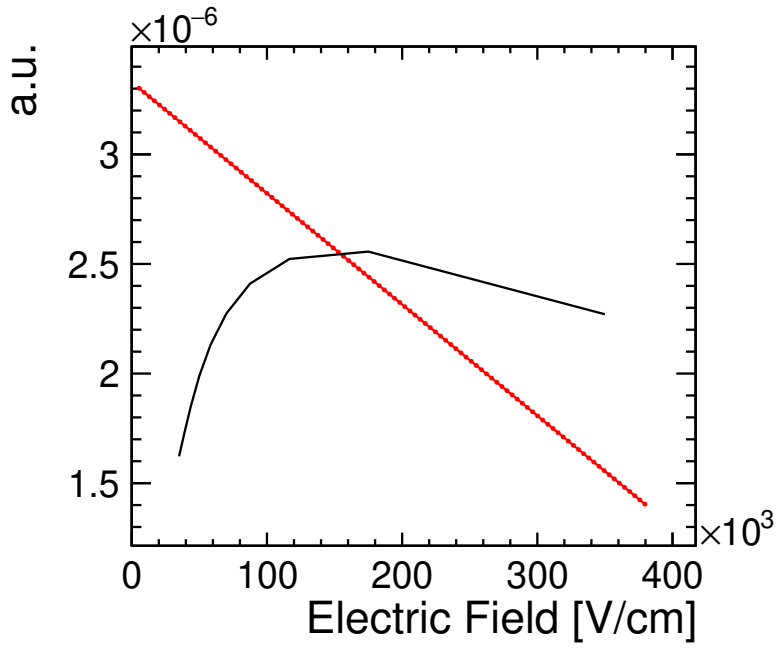

Figure 4.23: Theoretical prediction of the stability condition in the case of parallel plate geometry. The black line shows the ratio σ_0/ϵ, and the red line its differential. The intersection point corresponds to the gap of parallel plate of about 40 μm.

Then, we also performed Garfield++ simulation with a parallel plate geometry in relatively high electric field case (applied high voltage of 500 V). Figure. 4.24 shows the gap dependence of gas gain in the case of a parallel plate geometry with a voltage of 500 V. A stability region can be seen in the range from 25 μm to 30 μm, the area corresponding to an electric field strength of about 160 $\sim$ 200 kV/cm.

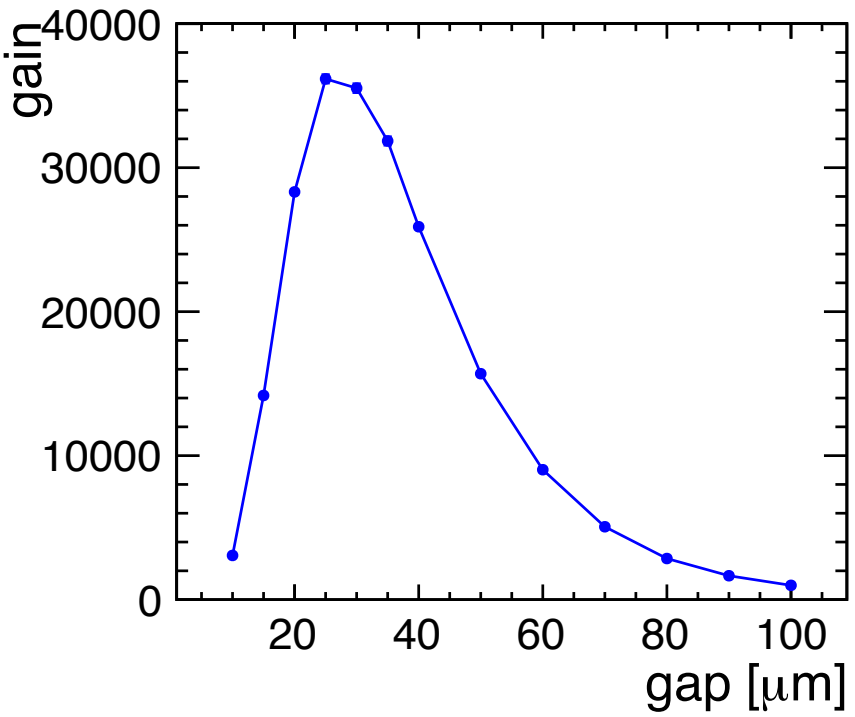

Figure 4.24: Gap dependence of gas gain in the case of a parallel plate geometry, T2K gas, and voltage of 500 V.

Figure. 4.25 shows the dependence of the inverse free–path $1/l$ on the electric field strength E, in the assumption $n = 1$ and the intersection point was found at around 100 kV/cm which corresponds to the gap of parallel plate of about 50 μm.

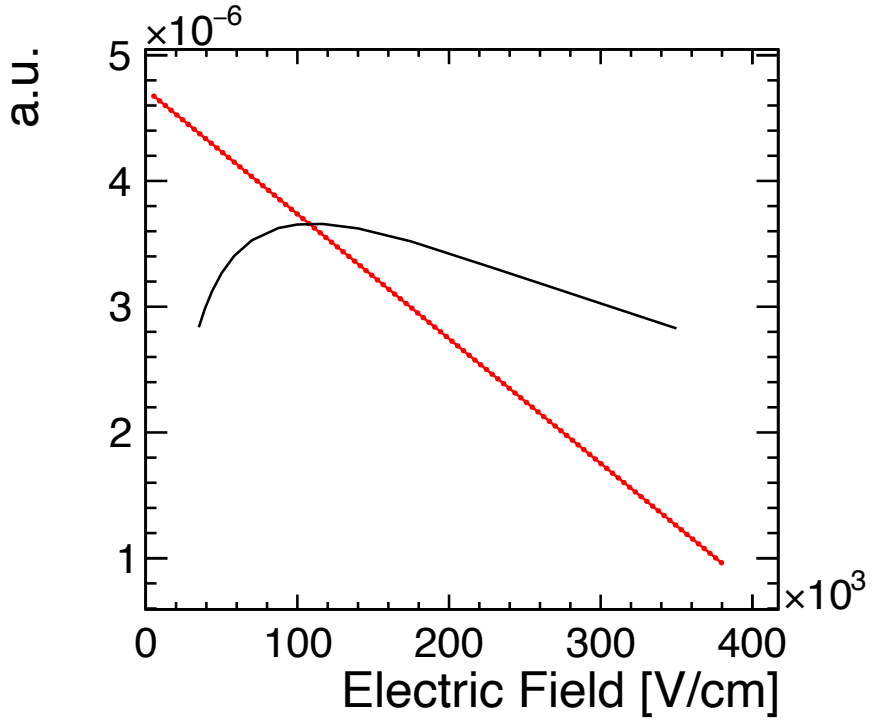

Figure 4.25: The cross-section σ_0 as a function of ϵ in the case of parallel plate geometry with a voltage of 500 V. This figure actually shows how the inverse mean free-path in μm depends on the E-field in the case $n = 1$.

Compared to the relatively low electric field case, the intersection point resulted in a more distance from the stable region. Possible reason is that after ionisation collision, electrons have enough energy for further ionisation, electrons being non-thermal, then this is inconsistent with Alkhazov's assumptions.

Therefore, under a uniform electric field by parallel plate geometry, the stability condition derived from our theory is not found to be in good agreement with the stability point of the gas gain found in a detailed simulation especially in relatively high electric field case.

4.6.2 GEM geometry

We also investigated whether a gas gain stability condition could be found in the more complex GEM geometry. Figure. 4.26 shows the simulated gas gain dependence on the GEM thickness. A stable region can be seen around 10 $\sim$ 40 μm, corresponding to an electric field strength of 350 $\sim$ 87 kV/cm.

As in the case of parallel plate geometry, the theory was tested in the case of GEM geometry by estimating the cross-section σ_0 from the mean free path calculated by Garfield++ at different electric field strengths, and identifying the point at which $\frac{\sigma_0}{\epsilon} = \frac{\partial \sigma_0}{\partial \epsilon}$. Fig. 4.27 shows how the inverse mean free path depends on the electric field strength, and 4.28 overlays $\frac{\sigma_0}{\epsilon}$ and its derivative $\frac{\partial \sigma_0}{\partial \epsilon}$ as a function of the field.

Fig. 4.28 shows an intersection between the curves at around $40 kV/cm$, corresponding to a gap of 90 μm, again far from the predicted stability condition. This is due to the complex electric field structure in the GEM hole.

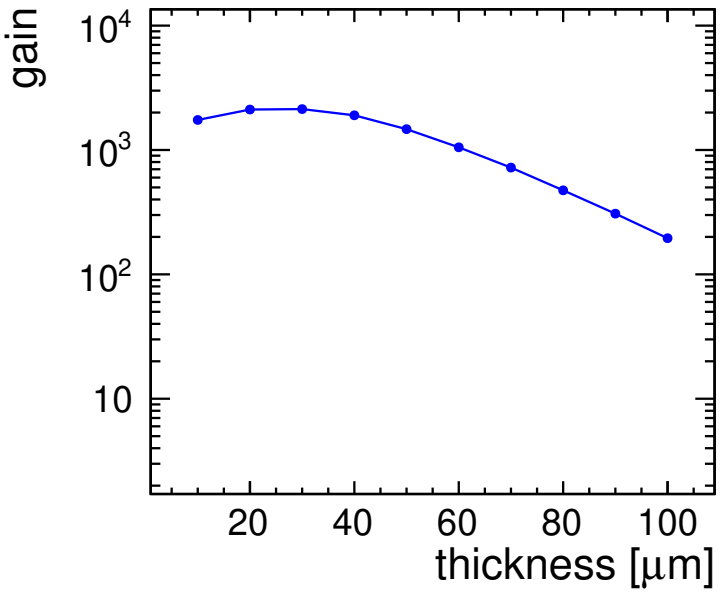

Figure 4.26: GEM thickness dependence of gas gain.

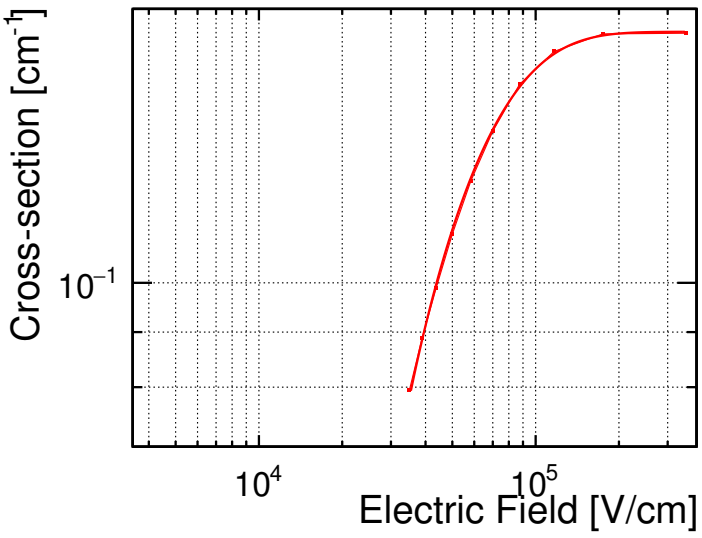

Figure 4.27: The cross-section σ_0 as a function of ϵ in the case of GEM geometry. Dependence of the inverse mean free path (μm^{-1}) on the applied electric field strength, as calculated by Garfield++ for the GEM geometry.

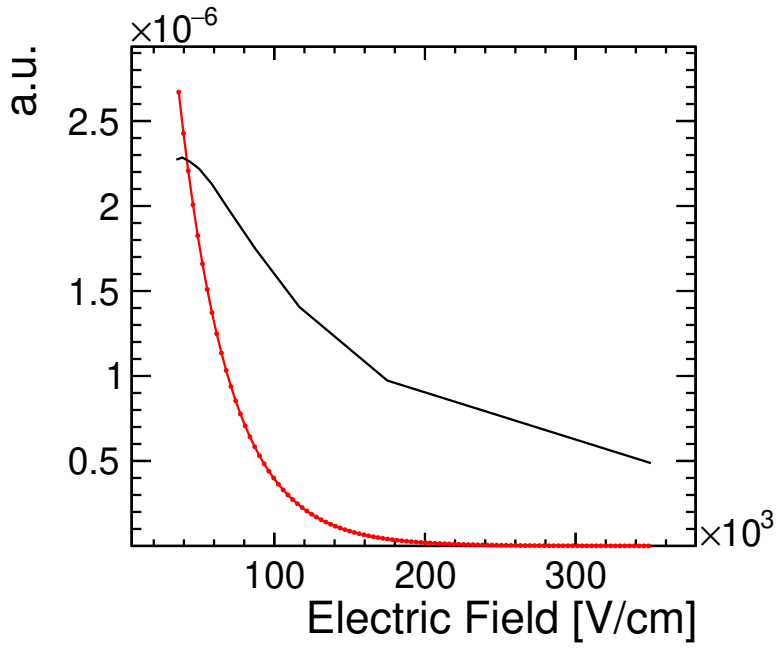

Figure 4.28: Theoretical prediction of the stability condition in the case of GEM geometry. The black line shows the ratio σ_0/ϵ, and the red line its differential.

4.7 Townsend coefficient

The Townsend coefficient is a rather fundamental quantity, which does not depend on the exact field geometry. The coefficient can be calculated in the simple case of a uniform field produced by a parallel plate geometry under different field strengths, and then applied to a more complex field configuration, such as that found in a GEM. This can then be used to identify and understand the stability condition of the complex detector.

Equation 4.34, derived from Alkhazov's theory, shows that the Townsend coefficient α can be obtained as a functional of $p_i(l)$. Specifically, by setting $J(1) = \frac{1}{2}$ using $p_i(l)$ obtained in a certain electric field, one can obtain the Townsend coefficient α at that electric field strength.

Figure. 4.29 shows the results of calculation of α using this approach, assuming Legler's model for $p_i(l)$. Compared to the Townsend coefficient used in Magboltz, the overall dependence on the field strength is similar, however the absolute values of the Townsend coefficient are around twice higher.

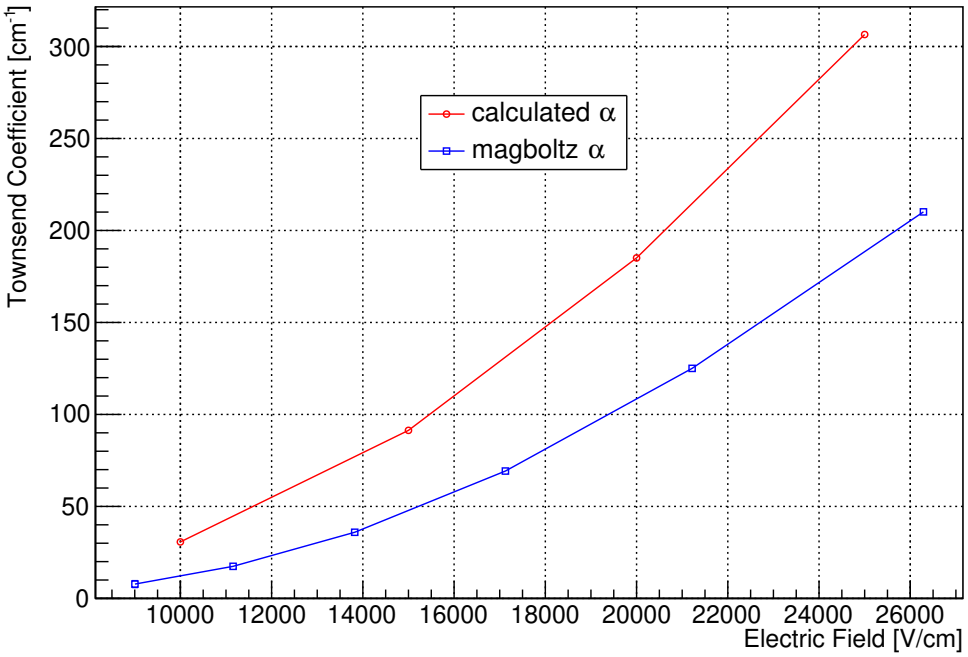

Figure 4.29: The results of the calculation of α. The red and blue line correspond to the calculated α and Magboltz α, respectively.

Using these two sets of Townsend coefficients, we calculate the gas gain. When considering the electron drift between points r_1 and r_2, the gas gain along that path is calculated as $\exp(\int_{r_1}^{r_2} \alpha(r)dr)$. The gas gain depends strongly on the value of the Townsend coefficient, resulting in large gas gain differences between the two sets of coefficients. The calculated gains are shown in Fig. 4.30, indeed showing that the gas gain calculated on the basis of our theory is much higher

that that calculated using the Townsend coefficients implemented in Magboltz.

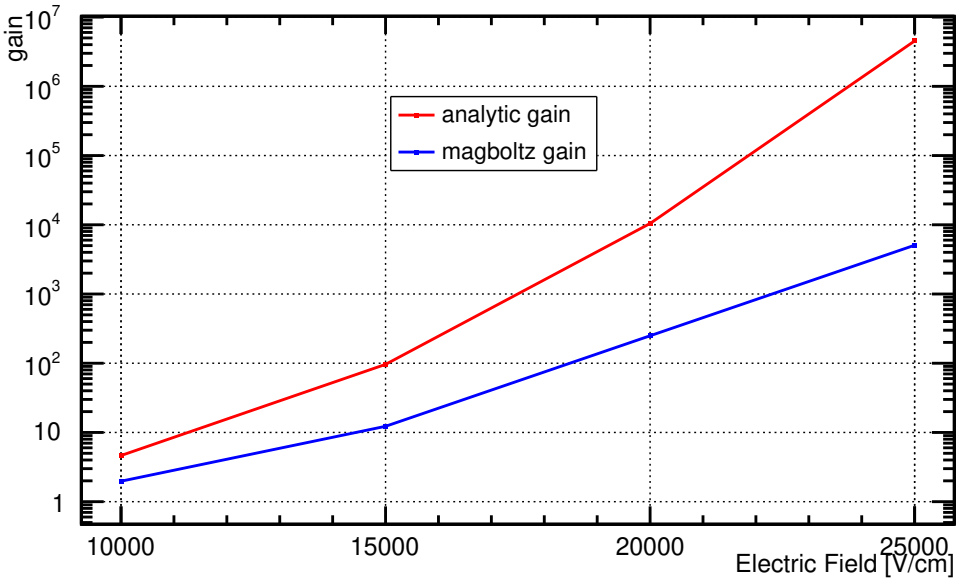

Figure 4.30: analytic gain

In summary, we used Alkhazov's theory to calculate the development of an avalanche in a high electric field, as found in a GEM, with the aim to identify a geometry in which the gain is insensitive to the GEM thickness. The calculated stability point was not in good agreement to the result of simulations using Garfield++, neither in the case of a parallel plate geometry, nor in a more detailed GEM-like model. Considering the more fundamental Townsend coefficient, the values calculated from the theory were significantly higher than those used in Magboltz, leading to the larger predicted gas gain.

To investigate the cause of these discrepancies, I developed a simple microscopic avalanche simulator code and used it to investigate the roles of various factors on avalanche formation.

4.8 Simple Microscopic Avalanche Simulator

We developed a code to simulate the avalanche process based on the cross-sections used in Magboltz Fig. 4.31, implementing a simple parallel plate geometry.

In this simple microscopic avalanche simulator, the following procedure was used:

- Setup the parameters of the system: the voltage applied across the plates; the (uniform) magnetic field; the gap width; and the gas mixture.
- Set the initial energy of the seed electron.

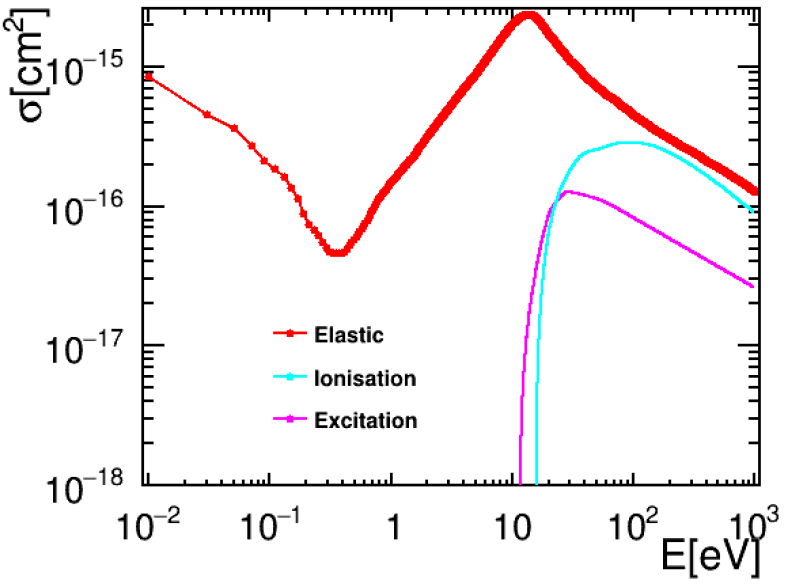

Figure 4.31: Cross-section used in Magboltz

- Calculate the electron's mean free path $l = 1/n\sigma$, using the total cross-section from Magboltz corresponding to the electron's energy.

- Advance the electron by a small step, approximately one tenth of the calculated mean free path, taking into account its acceleration in the electric and magnetic fields.
- For each step, randomly decide whether it undergoes a collision, based on the Magboltz cross-sections.
- If the electron undergoes an ionisation collision, trigger the creation of a new seed electron.
- If the electron reaches one of the parallel plates, kill it.
- Repeat until all electrons killed.

4.8.1 Comparison with Garfield++

We performed the simulations with applied high voltages of 310 to 390 V at 760 Torr with 128 μm gap parallel plate geometry . Figure. 4.32 shows the comparison of the gas gain curve between Garfield++ simulation result and the Simple simulator result. The Penning transfer is not considered, in other word the penning rate of $r = 0$ was used. The result of Garfield++ simulation and the Simple simulator gas gain is in good agreement.

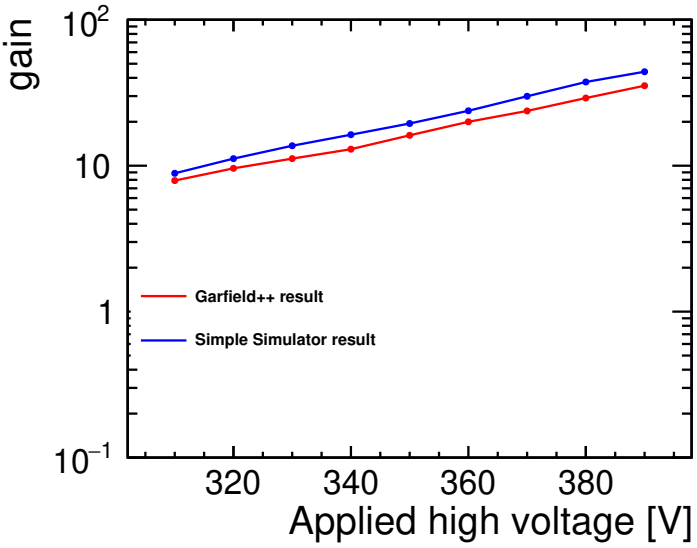

Figure 4.32: Comparison of gas gain curve of 128 μm gap parallel plate geometry for the T2K gas. The blue line is the result of the Simple simulator and the red line is the result of Garfield++ simulation. The Penning transfer is not taken into acount.

Comparison of measured data with Garfield++ using the parallel plate geometry confirms that the Simple simulator reproduces the Garfield++ result very well. Therefore, some simulations will be performed in the following section using Garfield++ and Simple simulator.

4.8.2 P/T correction

Equation. 4.17 predicts the gas density dependence of the gas gain G, as a function of both the absolute value and the high voltage dependence of the gas gain. Once the high voltage dependence of the gas gain and its absolute value are obtained, the gas density dependence of the gas gain can be predicted. If the temperature T (pressure P) is fixed, the gas density depends on the gas pressure (temperature).
If the ratio of the temperature and pressure are kept constant, the right-hand-side of Eq.4.17 indicates the gas gain is also kept constant. We have verified this theory by using both our simple MC simulator and Garfield++.

First, consider the case where the temperature T is changed while the pressure P of the gas is kept constant. When the temperature of gas is increased under constant pressure, the gas molecules are easily excited due to their high energy, and the gas gain is predicted to increase. Figure. 4.33 shows the change in gas gain when temperature T is changed from 250 K to 300 K while pressure P is kept constant at 760 Torr(1 atm), using both Garfield++ and our simple simulator.

In a similar way, the results of changing the pressure from 700 760Torr at a constant temperature $T = 273.15$ K are shown in Fig. 4.34. When the pressure is increased at a constant temperature, the electrons collide with gas

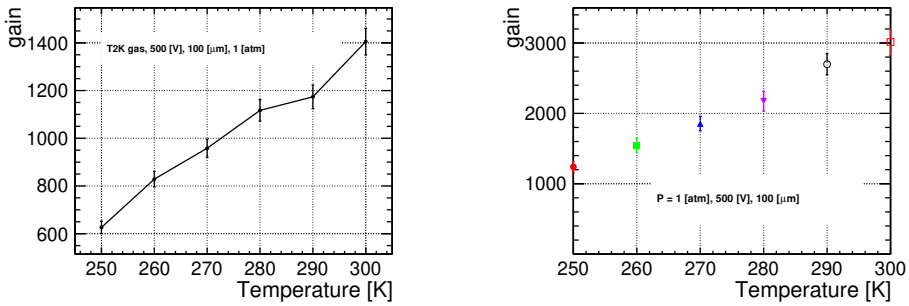

Figure 4.33: Change in gas gain when the temperature is changed from 250 to 300 K while the pressure P is kept constant at 1 atm. Results from Garfield++ (left) and our Simple Simulator (right).

molecules before they can obtain sufficient energy from the electric field to ionise the molecules, and the gas gain tends to decrease.

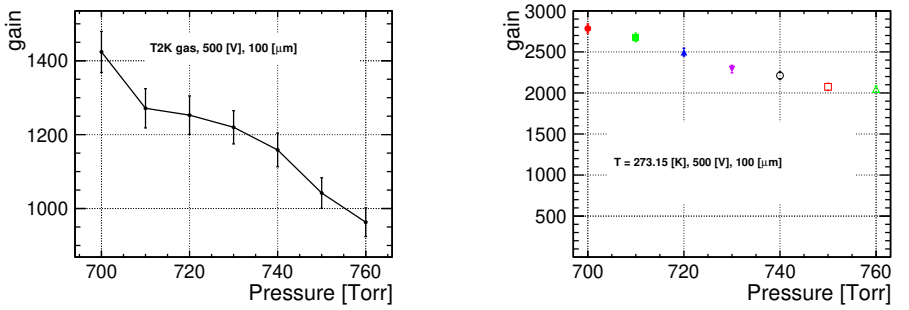

Figure 4.34: Change in gas gain when the pressure is changed from 700 to 760 Torr while the temperature T is kept constant $T = 273.15$ K. Results from Garfield++ (left) and our Simple Simulator (right).

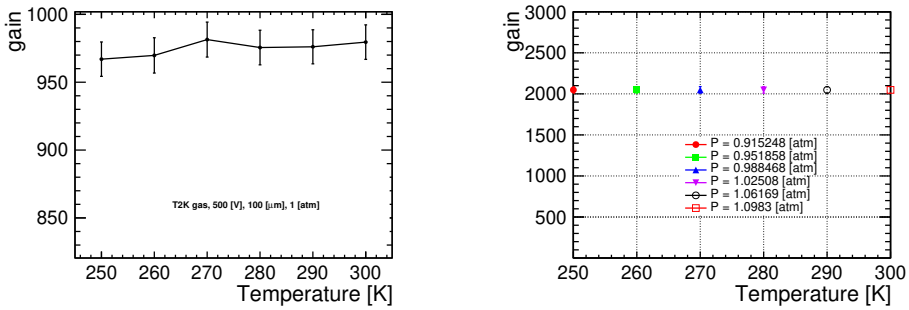

Figure 4.35: Change in gas gain when the temperature is changed from 250 to 300 K while keeping the ratio of pressure P to temperature constant. Results from Garfield++ (left) and our Simple Simulator (right).

The change in gas gain as temperature is varied while keeping the P/T ratio constant is shown in Figure. 4.35. In both Garfield++ and simple simulator, keeping the P/T ratio constant, also results in a constant gas gain. This is consistent with the behaviour predicted by the equations derived from the theory.

4.8.3 Gas gain

To check the performance of this simulator, it was used to simulate the gas gain under different conditions. The dependence of the gas gain on the gap width when using different argon-based gases and applied voltages was investigated, while keeping other conditions constant (temperature 273.15 K, pressure 1 atm, 1 T magnetic field parallel to the E-field).

Figure. 4.36 shows the gas gain in pure Argon, for gas gaps between 5 μm and 150 μm and applied voltages of 350, 375 and 400 V. The gain increases with increasing applied voltage, and a stability region is clearly seen at gaps around 20 μm

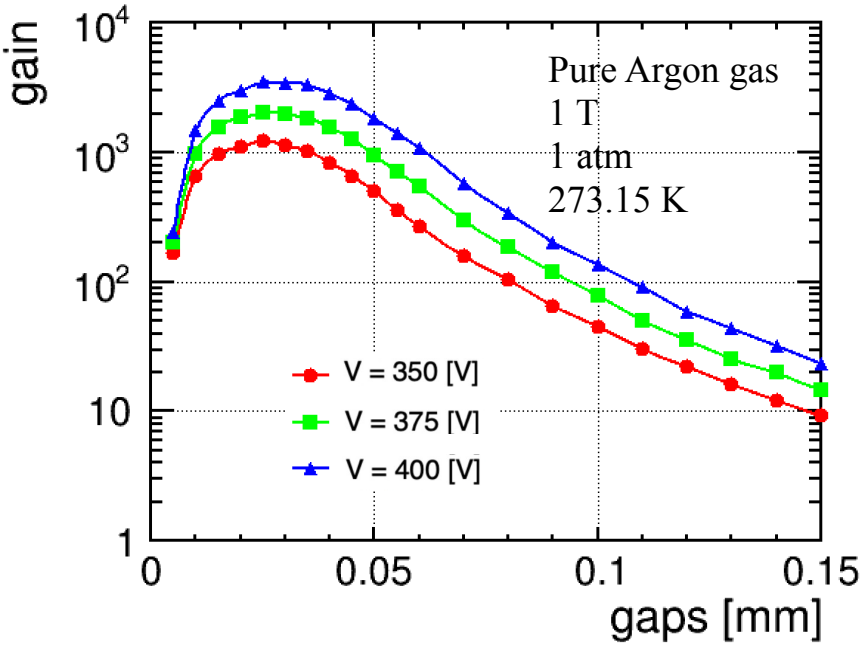

Figure 4.36: Gas gain as a function of gap width in pure Argon, with applied high voltage $350, 375, 400$ V.

To investigate the effect of the gas mixture, Fig. 4.37 shows how the gain dependence changes when 1, 5, or 10% of CF_4 is added to the argon. The addition of these fractions of CF_4 to the argon result in only rather small changes in the gas gain.

Next, the simulation was using the T2K gas we plan to use in ILD's TPC.The results are shown in Figure. 4.38. A stable region is seen in the gap range 10 μm to 40 μm. This result is in rather good agreement with results of the full Garfield++ simulation presented earlier in Figure. 4.26.

The effect of adding CF4 or isobutane to pure argon showed only small changes in gas gain. This is probably due to the fact that only fundamental reactions are taken into account in this simulator, ignoring effects such as the penning effect, and thus the contribution from argon is dominant.

Next, the electric and magnetic field dependence of the drift velocity and diffusion constant for each gas mixture was investigated.

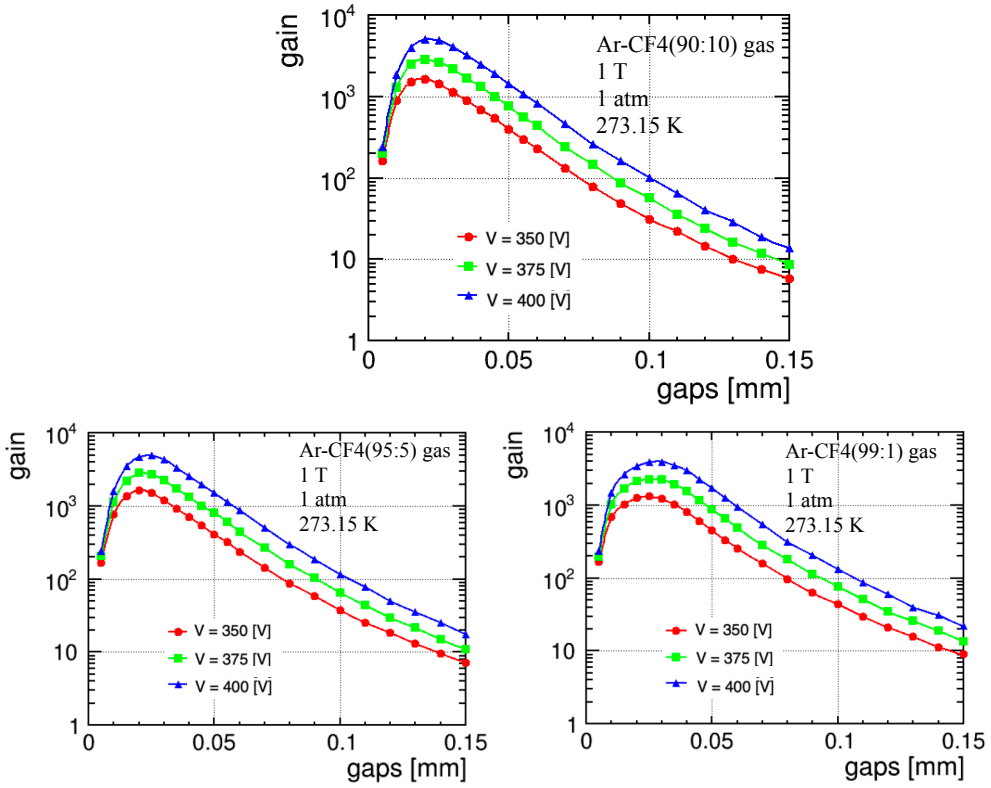

Figure 4.37: Gas gain in ArCF4 in the (90/10, 95/5, 99/1) concentrations with the applied high voltage of $350, 375, 400$ V.

Figure. 4.39 shows the electric field dependence of the drift velocity and diffusion constant for argon, ArCF4 and T2K gases under a magnetic field of 1 T. For both drift velocity and diffusion constant, the addition of a small amount of CF4 to pure Argon is found to produce dramatic changes.

Figure. 4.40 shows the electric field dependence of the drift velocity and diffusion constant in the T2K gas for different magnetic fields 1, 2, and 4 T applied parallel to the electric field. The drift velocity is not affected by the magnetic field, since particle velocities are largely aligned with the magnetic field. On the other hand, the magnetic field has a dramatic effect on the diffusion constant. The diffusion constant can be expressed as

$$C_d(B, E) = \frac{1}{\sqrt{1 + (\omega\tau)^2}} C_d(0, E) \tag{4.72}$$

where τ is the mean free time, ω the cyclotron frequency, and $C_d(0, E)$ the diffusion constant at 0 T. Since this cyclotron frequency ω depends linearly on the magnetic field, the diffusion constant is strongly affected.

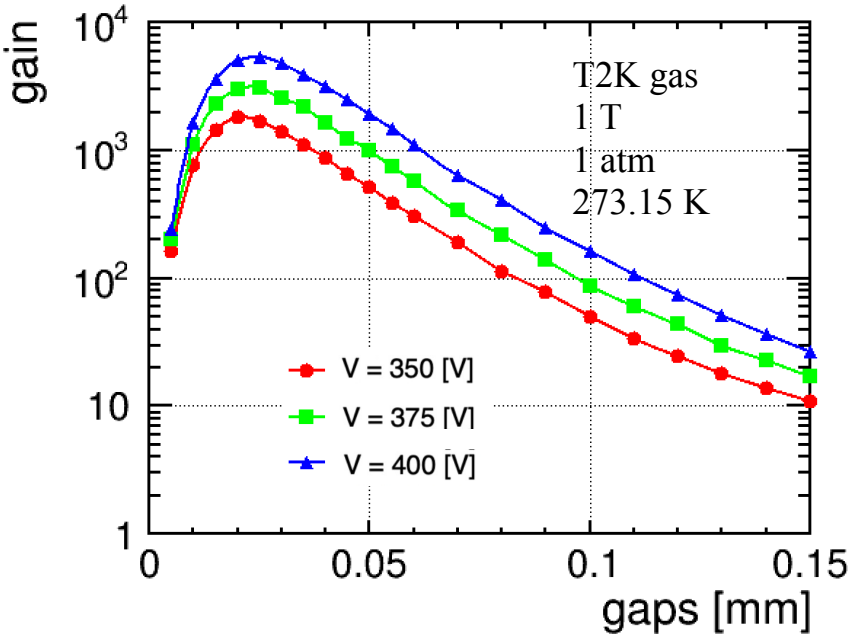

Figure 4.38: Gas gain in T2K gas with the applied high voltage of 350, 375, 400 V.

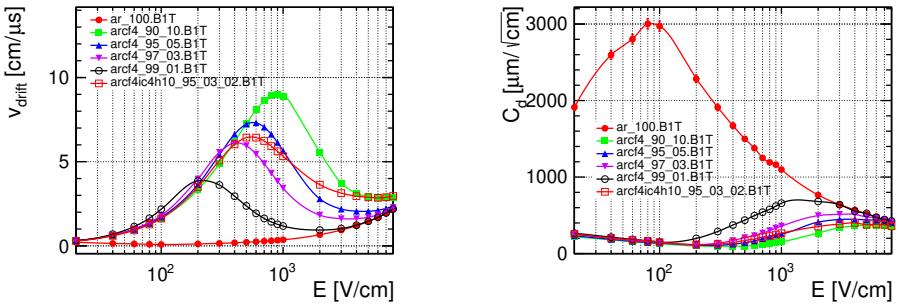

Figure 4.39: The electric field dependence of the drift velocity (left) and the diffusion constant (right) at 1 T for different gas mixtures.

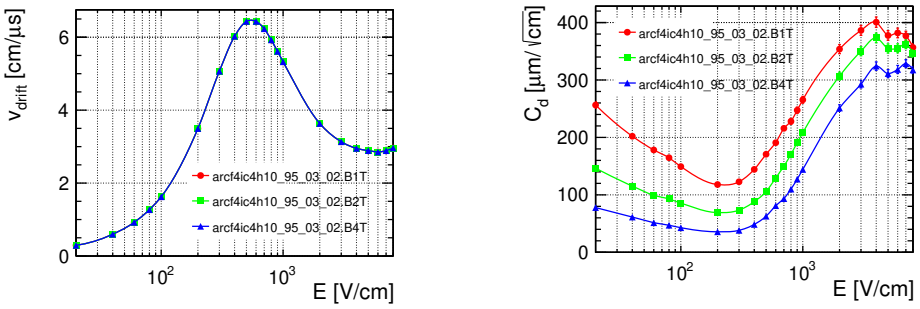

Figure 4.40: The electric field dependence of the drift velocity (left) and the diffusion constant (right) in T2K gas at magnetic field strengths 1, 2, 4 T.

4.8.4 Effect of z dependence of p_i

This simple simulator was used to simulate the avalanche process to and extract the function $p_i(l)$ for the case of a 25μm gap filled with T2K gas, at an applied voltage of 350 V and 400 V. Figure. 4.41 shows the distribution of all electron paths between ionisation collisions within the avalanche at an applied voltage of 350 V, as a function of their length projected onto the axis normal to the plates ($l = z_i - z_{lic}$, where z_i is the ending position of the step, and z_{lic} the position at which the particle last underwent an ionisation collision) and the initial z position of the path with respect to the upstream electrode ($z_{lic} - z_0$).

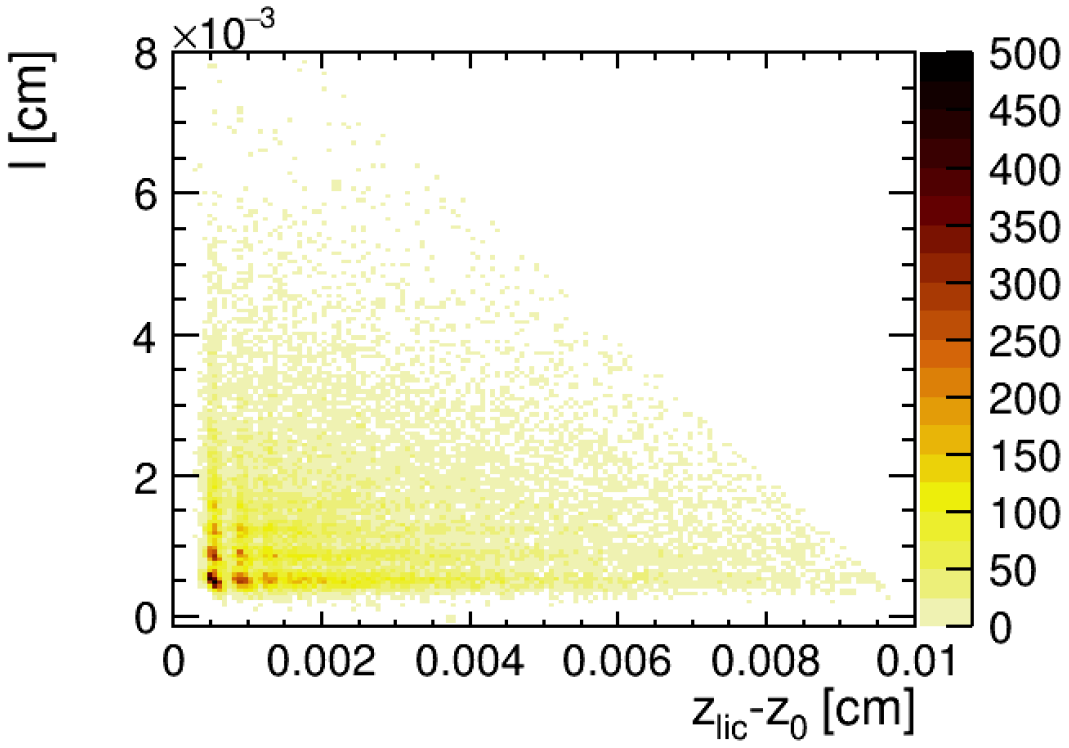

Figure 4.41: The free path l distribution as a function of the last ionisation position z_{lic} from original electron position x_0 and z-axis represents the probability of first ionising collision at an applied high voltage of 350 V.

The variable $z_{lic} - z_0$ is constrained to be between 0 and 100 μm, corresponding to the gap between electrodes. The l can have only positive values, corresponding to electrons moving against the direction of the electric field as shown in Fig. 4.42. The projection of this distribution onto the l axis, shown in Fig. 4.41, yields the probability density function for a particular path length, in other words $p_i(l)$.

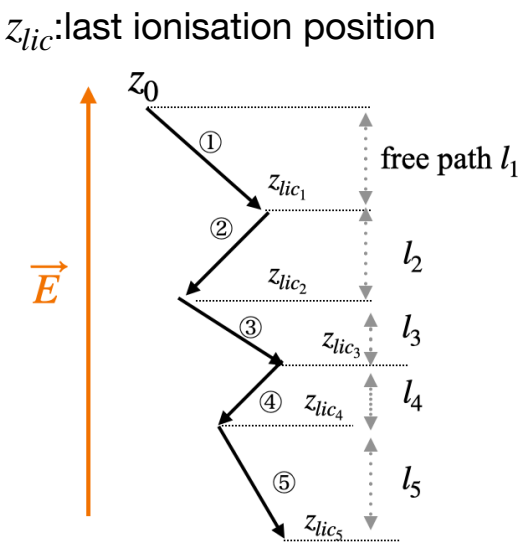

Figure 4.42: The schematic image of electrons moving against the direction of the electric field at an high voltage of 350 V. The l is always positive values in this relatively low electric field case.

Figure. 4.43 shows the projection onto the l axis for every 2.5 μm and Fig. 4.44 shows them all overlaid. Therefore, for this relatively low electric field case, p_i has no $z_{lic} - z_0$ dependence at all and this is consistent with Alkhazov's assumption: p_i does not depend on electron's position.

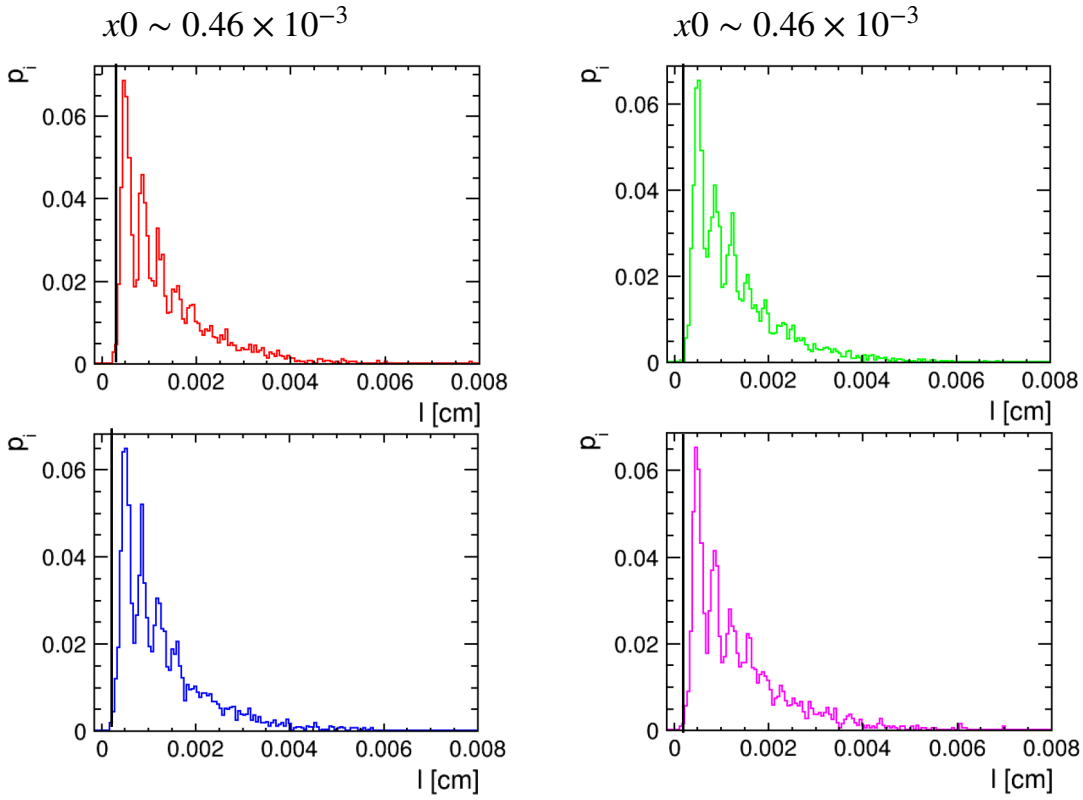

Figure 4.43: The projection onto the l axis for every 2.5 μm; The top left is for 2.5 μm, the top right is for 5 μm, the bottom left is for 7.5 μm, and the bottom right is for 10 μm. p_i does not depend on electron's position. The black line corresponds to the threshold $x_0 = 0.46 \times 10^{-3}$ cm.

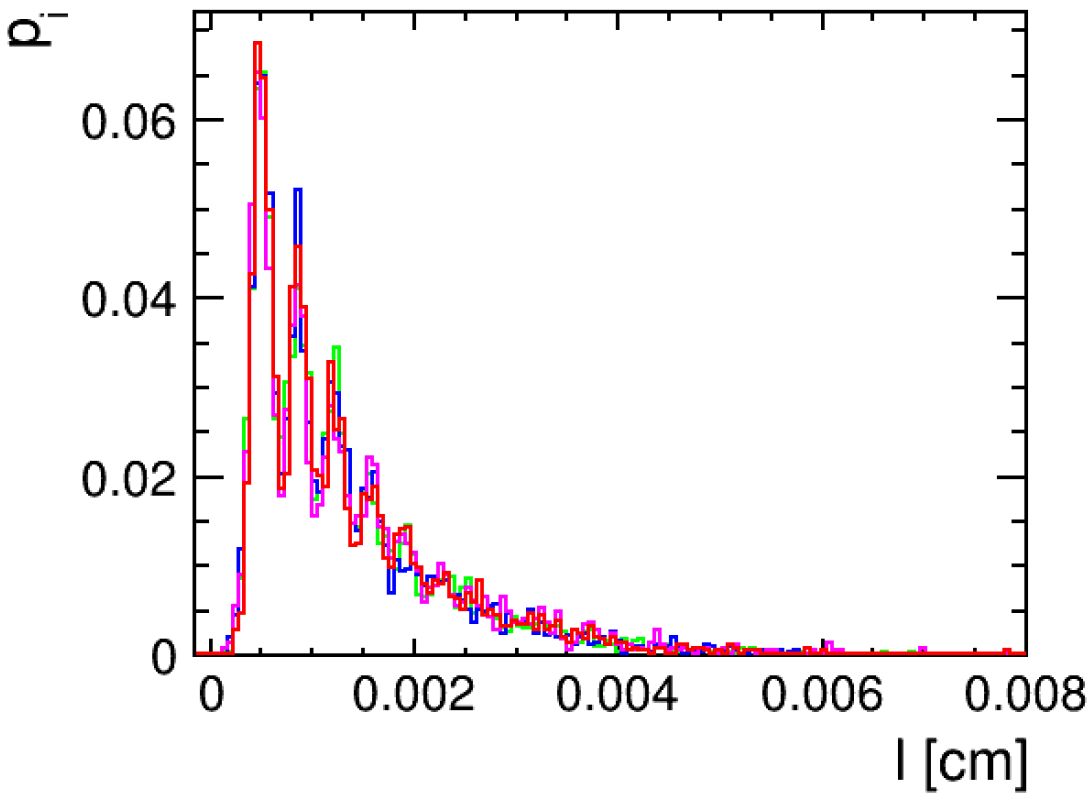

Figure 4.44: The overlaid plot of the projection plot shown in Fig. 4.43. The shapes of p_i are all identical for each region. Therefore p_i has no $z_{lic} - z_0$ dependence at all.

Next, we performed simulation with relatively high electric field case (an applied high voltage of 400 V). Figure. 4.45 shows the distribution of all electron paths between ionisation collisions within the avalanche at an applied voltage of 400 V, as a function of their length projected onto the axis normal to the plates ($l = z_i - z_{lic}$.

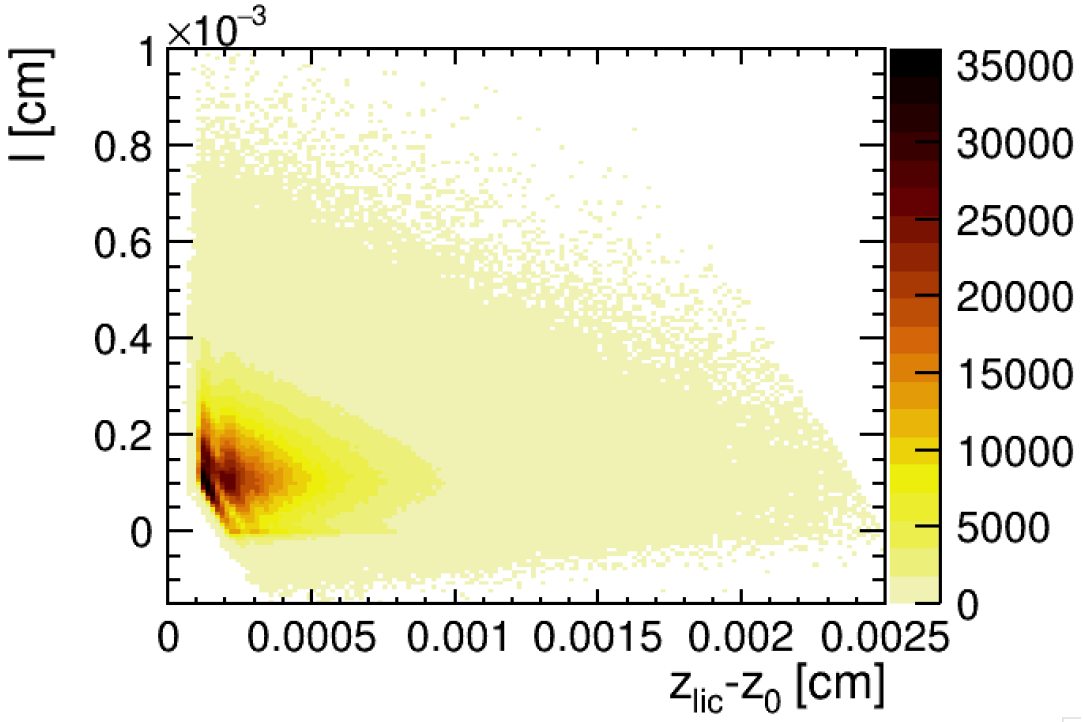

Figure 4.45: The free path l distribution as a function of the last ionisation position z_{lic} from original electron position x_0 and z-axis represents the probability of first ionising collision at an applied high voltage of 400 V.

The variable $z_{lic} - z_0$ is constrained to be between 0 and 25 μm, corresponding to the gap between electrodes. The l can have either positive or negative values, corresponding to electrons moving against or with the direction of the electric field as shown in Fig. 4.46. In other words, paths with a negative value of l are travelling against the prevailing avalanche direction; such paths are typically an order of magnitude shorter than those travelled in the "correct" direction.

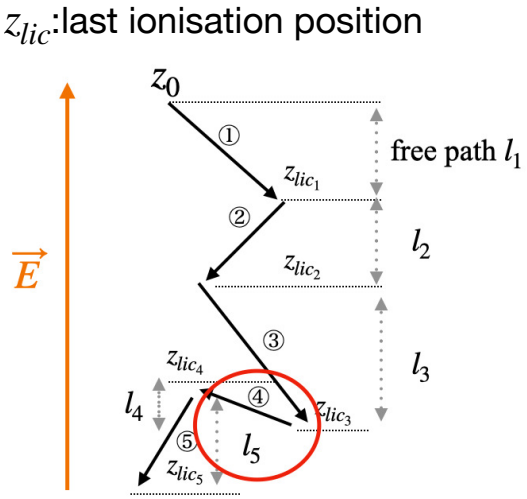

Figure 4.46: The schematic image of electrons moving against the direction of the electric field at an high voltage of 400 V. The l is always positive values in this relatively high electric field case.

The linear cut-off visible above $z_{lic} - z_0 \sim 21\mu$m is due to the proximity to the downstream electrode, which electrons hit before undergoing an ionisation collision. A second cut-off is seen at small values of $z_{lic} - z_0$ below around 3 μm.

Figure. 4.47 shows the projection onto the l axis for every 1 μm and Fig. 4.48 shows them all overlaid. Therefore, for this relatively high electric field case, p_i below $l = x_0 = 0.1 \times 10^{-3}$ cm develops with $z_{lic} - z_0$; p_i does depend on electron's position and this is inconsistent with Alkhazov's assumption.

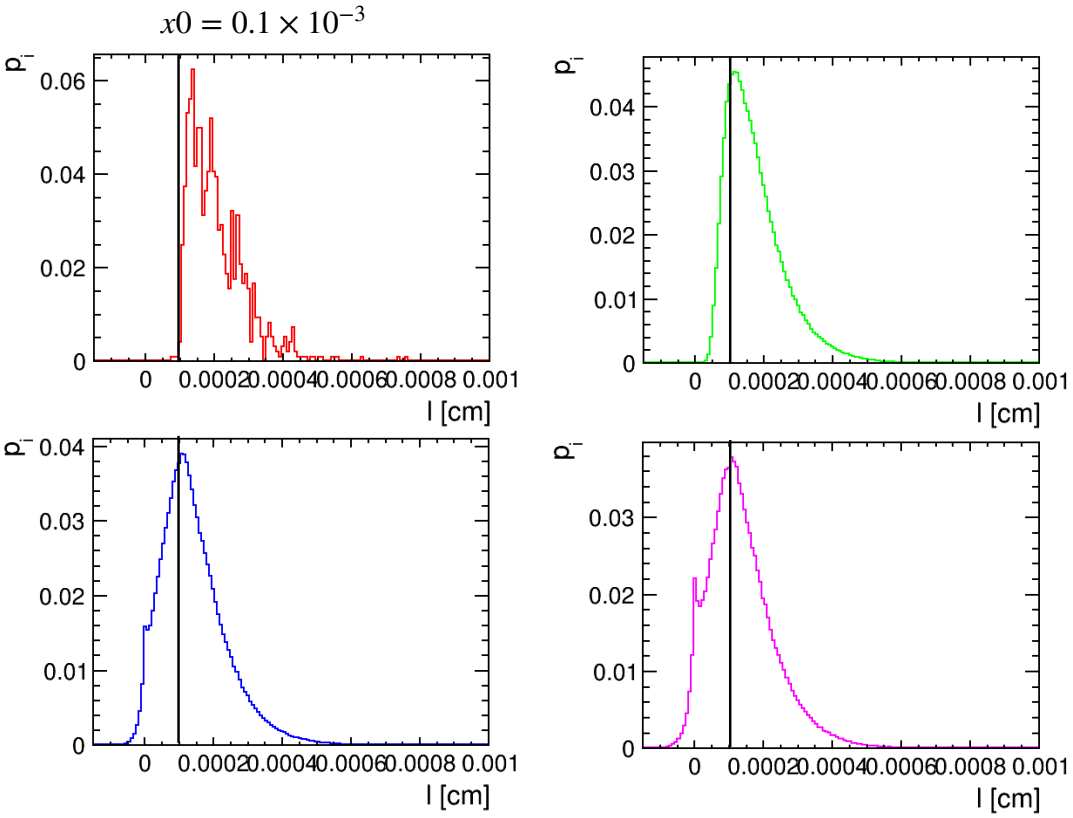

Figure 4.47: The projection onto the l axis for every 1 μm; The top left is for 1 μm, the top right is for 2 μm, the bottom left is for 3 μm, and the bottom right is for 4 μm. p_i does not depend on electron's position. The black line corresponds to the threshold $x_0 = 0.46 \times 10^{-3}$ cm and p_i can have either positive or negative values even for the region below this threshold.

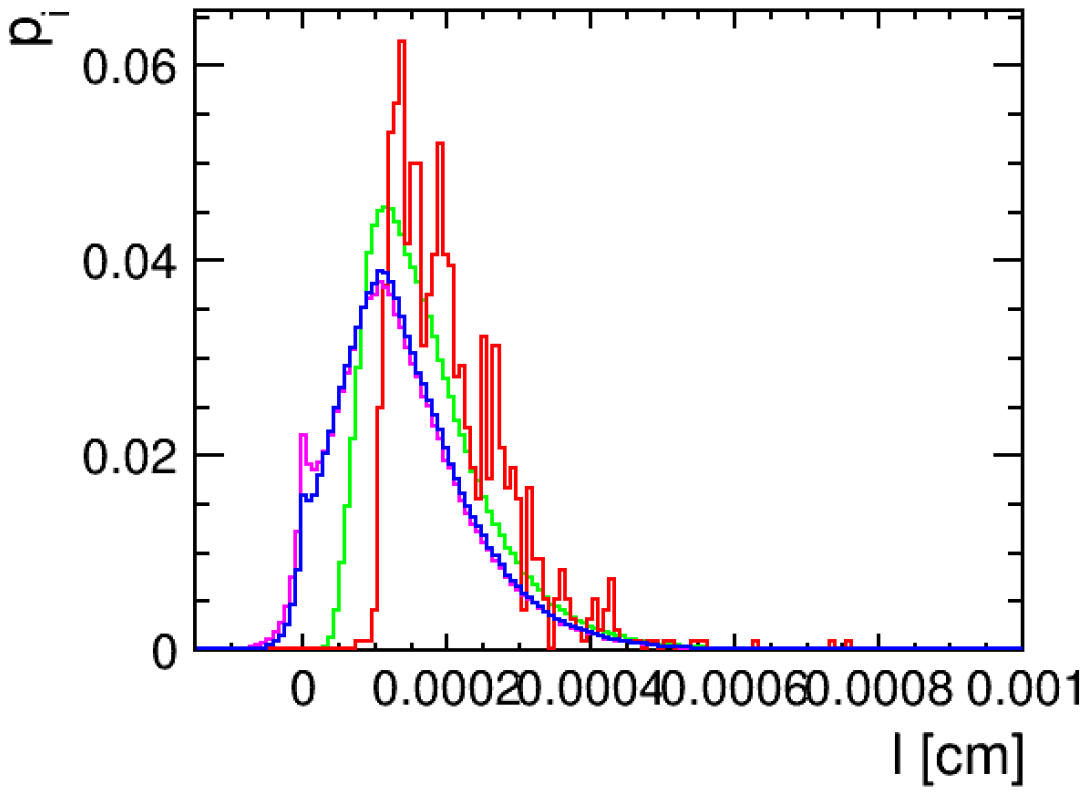

Figure 4.48: The overlaid plot of the projection plot shown in Fig. 4.47. The shapes of p_i changes for each region. Therefore p_i dependent on $z_{lic} - z_0$ and this is inconsistent with Alkhazov's assumption.

In the Fig. 4.45, projection onto the y-axis (l) yields $p_i(l)$. The result is shown in the Fig. 4.49 and the distributions of the gas gain from Simple Simulator is shown in the Fig. 4.50 with the mean value of gas gain of 5416.

Then, we performed toyMC simulation based on the $p_i(l)$ and the result of gas gain distribution is shown in the Fig. 4.51. The mean value of this gas gain is 44230.

The Townsend coefficient α calculated using this $p_i(l)$ is about 4353, resulting in a gain of 34454. However, the resultant gas gain from toyMC simulation based on this $p_i(l)$ is 44230. Therefore, by comparing the gas gain of 5416 from Simple Simulator, it is significant overestimate ($\sim$800%) so the gas gain is too large if MC p_i is used as it is.

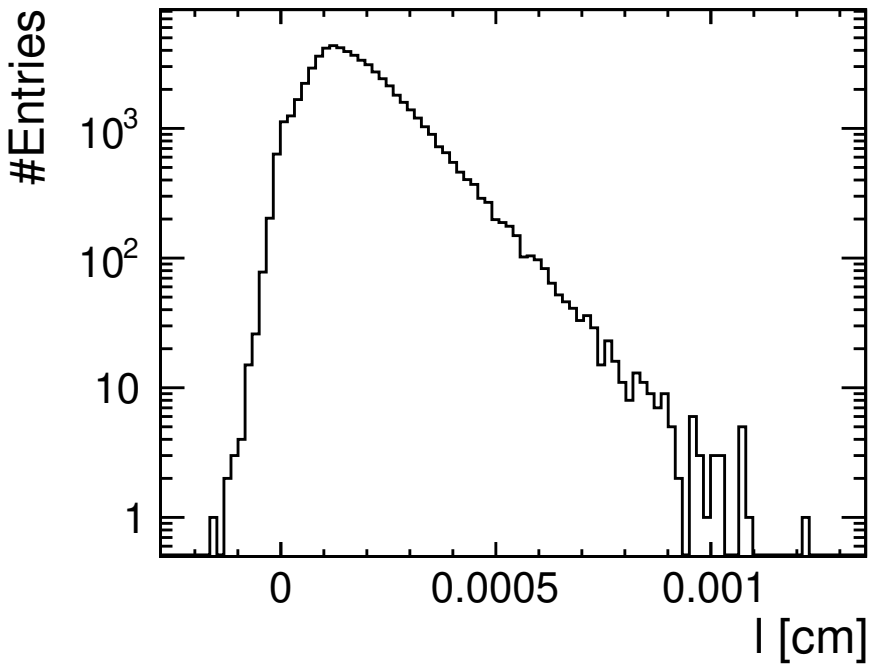

Figure 4.49: The probability of first ionising collision p_i distributions as a function of the free path l.

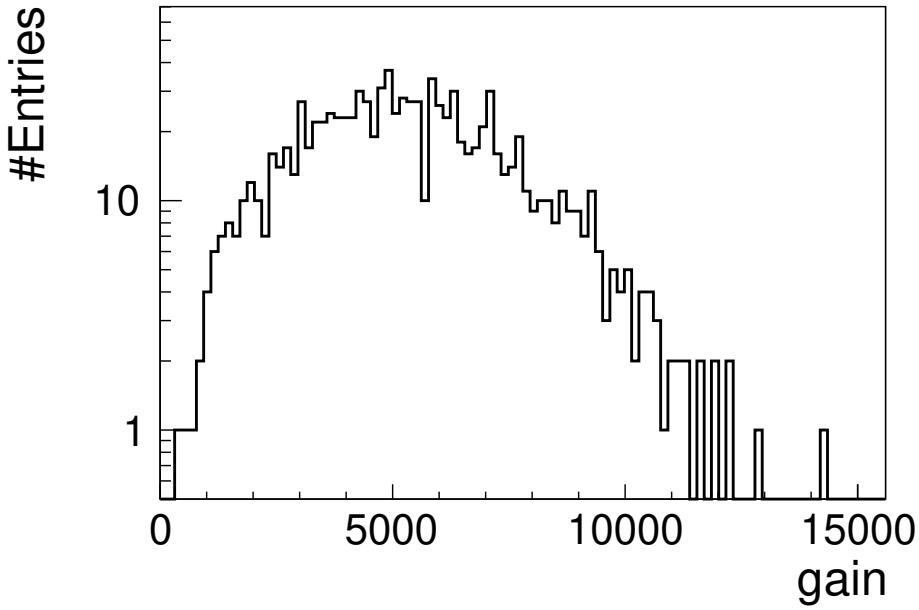

Figure 4.50: The resultant gas gain distributions from Simple MC Simulator.

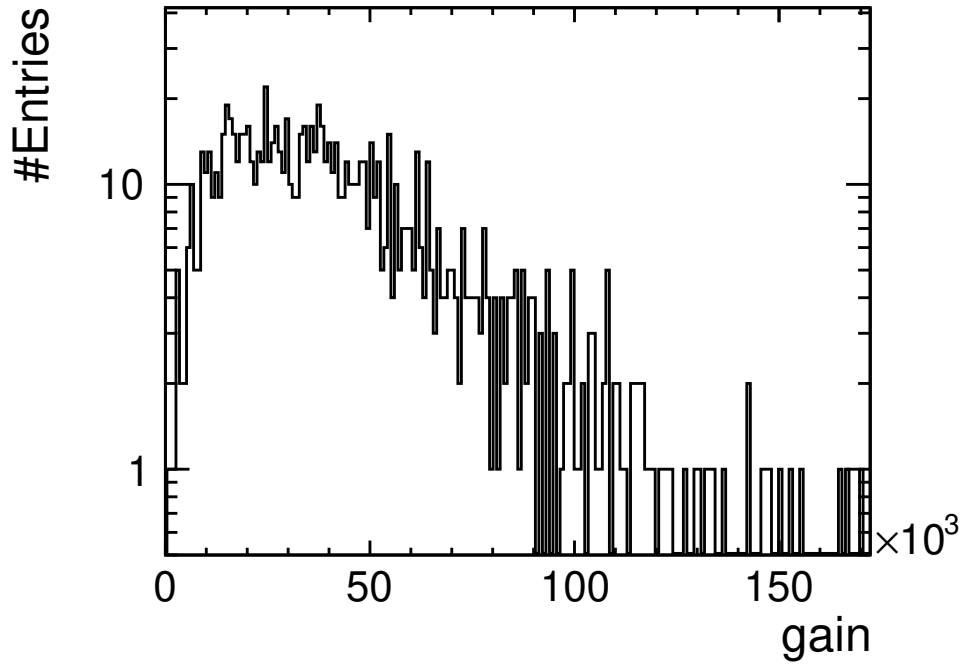

Figure 4.51: The resultant gas gain distributions from toyMC based on $p_i(l)$ from MC.

In the region $l < x_0$, $p_i(l)$ develops in dependence on z_{lic}, so the result of ignoring this development process, i.e. truncating $p_i(l)$ at x_0, is shown in Fig. 4.52. The Townsend coefficient α calculated using this $p_i(l)$ is about 3146, resulting in a gain of 1902. The resultant gas gain from toyMC simulation is 2030. Compared with the results before truncating at $l = x_0$, the difference between the gas gain calculated using the α at $p_i(l)$ with $J(1)$ as $\frac{1}{2}$ derived from theory and the gas gain obtained from the toyMC simulation results were in reasonable agreement, however, it is still significant underestimate ($\sim$40%) compared with the gas gain of 5416 from Simple Simulator.

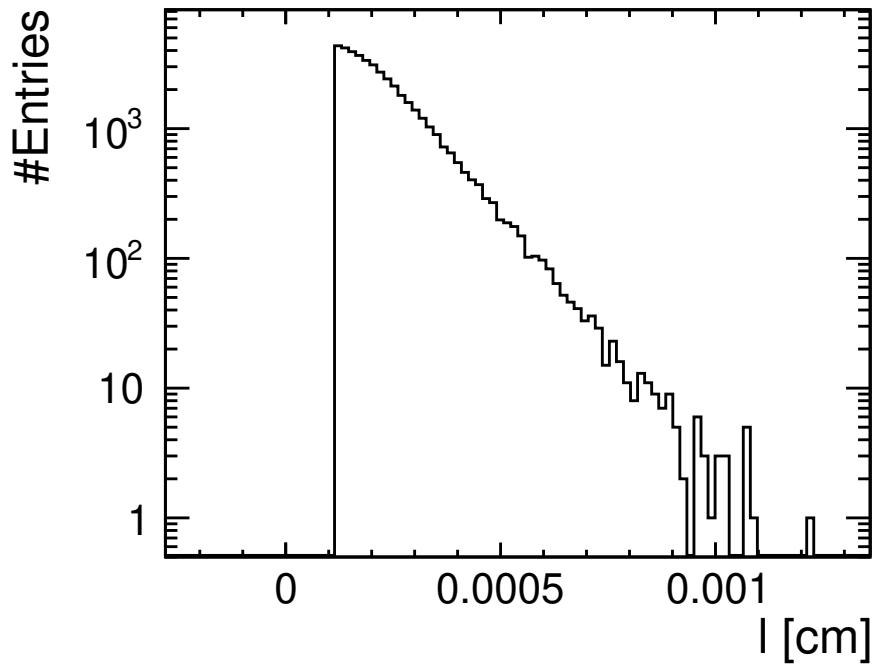

Figure 4.52: The probability of first ionising collision p_i distributions as a function of the free path l but truncated at $l = x_0 = 0.0001$ [cm].

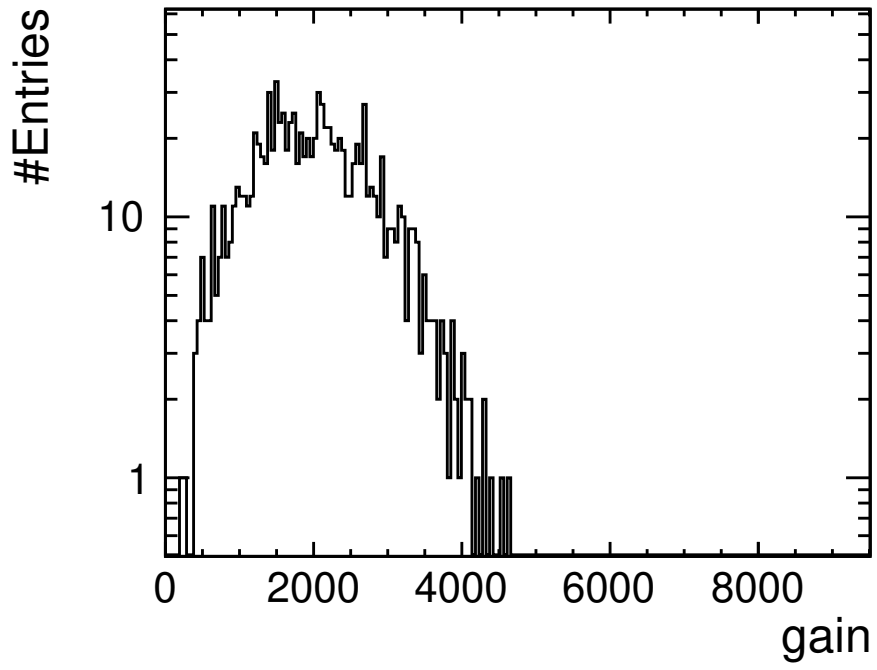

Figure 4.53: The resultant gas gain distributions from MC simulation based on $p_i(l)$ from MC but truncated at $l = x_0 = 0.0001$ [cm].

The problem is that the shape of $p_i(l)$ changes in the region up to the x_0 threshold, and when simulations were performed in Garfield++, the gas gain were calculated using $p_i(l)$ obtained by projection without considering this region. In the region after the evolution of $p_i(l)$ due to this $z_{lic} - z_0$ dependence, the shape of $p_i(l)$ is almost constant and the Townsend coefficient α and gas gain calculated based on Alkhazov's theory agree with the MC simulation results.

Then, we have checked this the effect of this $z_{lic} - z_0$ dependence of $p_i(l)$ by using $z_{lic} - z_0$-dependent $p_i(l, z_{lic} - z_0)$ instead of $p_i(l)$. The result of gas gain distribution is shown in Fig. 4.54. The resultant gas gain from toyMC simulation in simple simulator is 3918 by using $z_{lic} - z_0$-dependent $p_i(l, z_{lic} - z_0)$. Compared with the gas gain of 5416 from Simple Simulator, it is still underestimate (∼80%), however, much better than toyMC result of overestimated gas gain of 44230 (∼800%) with MC p_i is used as it is and the underestimated gain of 2030 (∼40%) with $p_i(l)$ truncated at $l = x_0$.

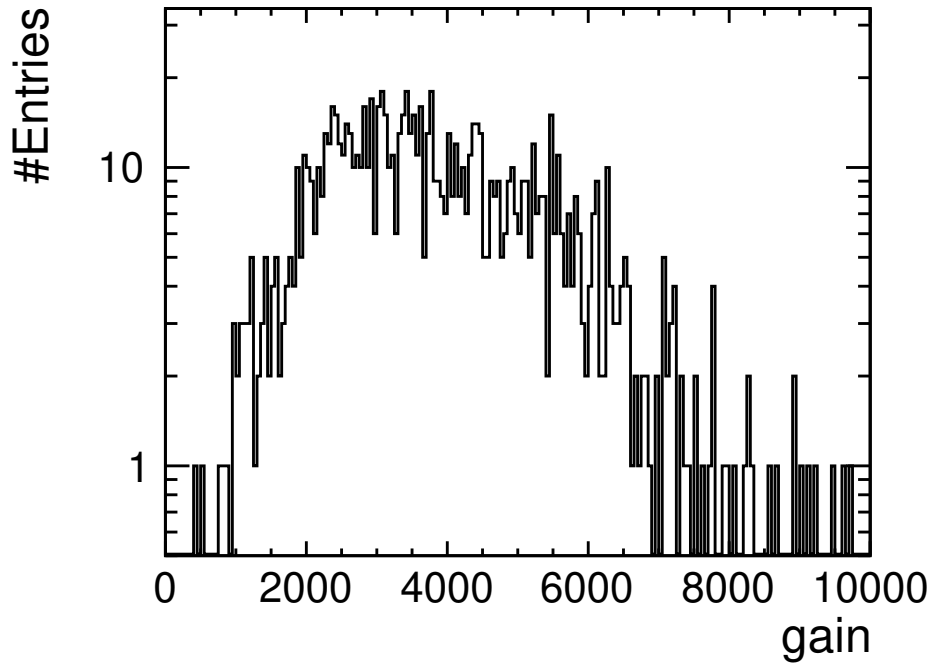

Figure 4.54: The resultant gas gain distributions from toyMC based on $z_{lic} - z_0$-dependent $p_i(l, z_{lic} - z_0)$ instead of $p_i(l)$ from MC.

Compared with the results before truncating at $l = x_0$, the difference between the gas gain calculated using the α at $p_i(l)$ with $J(1)$ as $\frac{1}{2}$ derived from theory and the gas gain obtained from the toyMC simulation results were in reasonable agreement, however, it is still significant underestimate (∼40%)

Therefore, it is found that $p_i(l)$ at $l < x_0$ develops with the distance to next ionisation $z_{lic} - z_0$. If ignored this $z_{lic} - z_0$ dependence, it can make significant difference in the resultant gas gain. Thus, in order to calculate the gas gain analytically, it is necessary to construct a theory that takes this x_0 threshold into account. In Eq. 4.27, we ignored this z dependence, however, for analytical

gas gain calculations, it is important to consider the early stage of avalanche growth and it is necessary to proceed with the calculation with $p_i(l)$ as $p_i(l, z)$.

4.9 Conclusion and Future prospect

The aim of this study was to develop the theoretical understanding of the Gas Elelctron Multiplier (GEM) in order to propose a design whose gain is insensitive to small variations in GEM foil thickness. Such a GEM will result in a GEM with more uniform response, and therefore easier to operate and calibrate. This will lead to obvous advantages when using 100s of such GEM detectors to read out the signals of a large Time Projection Chamber at a future experiment at the ILC, whose lifetime should extend to several decades.

Based on Alkhazov's theory for avalanche development and assuming Legler's model of ionisation, we derived a theoretical "Stability condition" configuration whose gas gain is stable against gap variation.
When the gas gain distribution was plotted as a function of the parallel plate gap and GEM thickness, a region was found in which the gas gain was almost stable with respect to the gap variation in both cases. In the parallel plate case, i.e., under a uniform electric field, the "Stability condition" is not satisfied in this stable region. In the case of GEM geometry with a complex electric field structure near the hole, also the "Stability condition" was not satisfied.

We investigated whether the magboltz results could be reproduced using the Townsend coefficient calculated as a functional of the probability of first ionising collision, and found that they could not be reproduced. The differences became particularly large in the high electric field regime compared to the low electric field regime. This indicates that there is a strong dependence on the strength of the electric field for the calculation of the Townsend coefficient.

To investigate whether the inability to reproduce the Magboltz results is due to the scope of Alkhazov's theory or to a problem with the probability of first ionising collision used to calculate the Townsend coefficient, a simple microscopic avalanche simulator was developed.

The simulator results show that the probability of first ionising collision is strongly influenced by the avalanche growth process and has z-dependence.

Since we have discussed the Legler's model in Alkhazov's theory assuming that this z-dependence is negligible, the derived "Stability condition" does not take this z-dependence into account.

The z-dependence of the probability of first ionising collision is found to be very important in discussing the stability of gas gain. As a future perspective, we will derive a "Stability condition" that takes this z-dependence into account and investigate the geometry conditions under which the gas gain is stable with respect to the gap variation.

The development of the Simple Microscopic Avalanche Simulator, relatively high speed tool, and the identification of the reason why Alkhazov's theory does not hold true in this study have provided a solid foundation for providing feedback to the actual TPC-GEM in the future. This is a major step toward solving the discharge problem of the GEM described in the first section.

CHAPTER 5

APPENDIX

Contents

5.1 Polarisation

$$d\sigma_{Ll} = N g_{e_L}^2 g_{f_L}^2 (1+\cos\theta)^2 \, d\cos\theta \tag{5.1}$$

$$d\sigma_{Lr} = N g_{e_L}^2 g_{f_R}^2 (1-\cos\theta)^2 \, d\cos\theta \tag{5.2}$$

$$d\sigma_{Rl} = N g_{e_R}^2 g_{f_L}^2 (1-\cos\theta)^2 \, d\cos\theta \tag{5.3}$$

$$d\sigma_{Rr} = N g_{e_R}^2 g_{f_R}^2 (1+\cos\theta)^2 \, d\cos\theta \tag{5.4}$$

$$d\sigma_l = \frac{1}{2}(1-P_-)\frac{1}{2}(1+P_+)d\sigma_{Ll} + \frac{1}{2}(1+P_-)\frac{1}{2}(1-P_+)d\sigma_{Rl} \tag{5.5}$$

$$d\sigma_r = \frac{1}{2}(1-P_-)\frac{1}{2}(1+P_+)d\sigma_{Lr} + \frac{1}{2}(1+P_-)\frac{1}{2}(1-P_+)d\sigma_{Rr} \tag{5.6}$$

$$
\begin{aligned}
d\sigma_l &= N\left(\frac{1}{2}(1-P_-)\frac{1}{2}(1+P_+)g_{e_L}^2 g_{f_L}^2(1+\cos\theta)^2\right.\\
&\quad\left.+\frac{1}{2}(1+P_-)\frac{1}{2}(1-P_+)g_{e_R}^2 g_{f_L}^2(1-\cos\theta)^2\right)\,d\cos\theta\\
&= \frac{N}{4}\left((1-P_-)(1+P_+)g_{e_L}^2 g_{f_L}^2(1+\cos\theta)^2+(1+P_-)(1-P_+)g_{e_R}^2 g_{f_L}^2(1-\cos\theta)^2\right)\,d\cos\theta\\
&= \frac{N}{4}\left(((1-P_-P_+)-(P_--P_+))g_{e_L}^2 g_{f_L}^2(1+\cos\theta)\right.\\
&\quad\left.+((1-P_-P_+)+(P_--P_+))g_{e_R}^2 g_{f_L}^2(1-\cos\theta)^2\right)\,d\cos\theta\\
&= \frac{N}{4}(1-P_-P_+)g_{f_L}^2\left((1-P_e)g_{e_L}^2(1+\cos\theta)^2+(1+P_e)g_{e_R}^2(1-\cos\theta)^2\right)\,d\cos\theta\\
&= \frac{N}{4}(1-P_-P_+)g_{f_L}^2\left[\left((1-P_e)g_{e_L}^2+(1+P_e)g_{e_R}^2\right)(1+\cos^2\theta)\right.\\
&\quad\left.+2\left((1-P_e)g_{e_L}^2-(1+P_e)g_{e_R}^2\right)\cos\theta\right]\,d\cos\theta\\
&= \frac{N}{4}(1-P_-P_+)g_{f_L}^2(g_{e_L}^2+g_{e_R}^2)\left[(1-A_eP_e)(1+\cos^2\theta)+2(A_e-P_e)\cos\theta\right]\,d\cos\theta
\end{aligned}
$$

$$
\begin{aligned}
d\sigma_r &= N\left(\frac{1}{2}(1-P_-)\frac{1}{2}(1+P_+)g_{e_L}^2 g_{f_R}^2(1-\cos\theta)^2\right.\\
&\quad\left.+\frac{1}{2}(1+P_-)\frac{1}{2}(1-P_+)g_{e_R}^2 g_{f_R}^2(1+\cos\theta)^2\right)\,d\cos\theta\\
&= \frac{N}{4}(1-P_-P_+)g_{f_R}^2(g_{e_L}^2+g_{e_R}^2)\left[(1-A_eP_e)(1+\cos^2\theta)-2(A_e-P_e)\cos\theta\right]\,d\cos\theta
\end{aligned}
\tag{5.7}
$$

$$
\frac{d\sigma}{d\cos\theta} = \frac{N}{4}(1-P_-P_+)(g_{e_L}^2+g_{e_R}^2)(g_{f_L}^2+g_{f_R}^2)\left[(1-A_eP_e)(1+\cos^2\theta)+2(A_e-P_e)A_f\cos\theta\right]
\tag{5.8}
$$

5.2 Derivation: Alkhazov's Theory

Here we derive the recurrence formula of the moment of avalanche fluctuation. First, let's start from Eq. 4.29

$$M_n = \sum_{N=0}^{\infty} \frac{1}{\bar{N}(x)} \left(\frac{N}{\bar{N}(x)} \right)^n \bar{N}(x) P(N;x) \tag{5.9}$$

with Eq. 4.27

$$P(N;x) = \int_0^x dl p_i(l) \sum_{N'=1}^{N-1} P(N';x-l) P(N-N';x-l). \tag{5.10}$$

We found

$$
\begin{aligned}
M_n &= \int_0^x dl\ p_i(l) \sum_{N=1}^{\infty} \sum_{N'=1}^{N-1} \frac{1}{\bar{N}(x)} \left(\frac{N}{\bar{N}(x)} \right)^n \bar{N}(x) \\
&\quad P(N'; x-l) P(N-N'; x-l) \\
&= \int_0^x dl\ p_i(l) \sum_{N=1}^{\infty} \sum_{N'=1}^{N-1} \left(\frac{\bar{N}(x-l)N}{\bar{N}(x-l)\bar{N}(x)} \right)^n P(N'; x-l) P(N-N'; x-l) \\
&= \int_0^x dl\ p_i(l) \left(\frac{\bar{N}(x-l)}{\bar{N}(x)} \right)^n \sum_{N=1}^{\infty} \sum_{N'=1}^{N-1} \left(\frac{N' + (N-N')}{\bar{N}(x-l)} \right)^n P(N'; x-l) P(N-N'; x-l) \\
&= \int_0^x dl\ p_i(l) \left(\frac{\bar{N}(x-l)}{\bar{N}(x)} \right)^n \sum_{N=1}^{\infty} \sum_{N'=1}^{N-1} \sum_{k=0}^{n} \frac{n!}{k!(n-k)!} \left(\frac{N'}{\bar{N}(x-l)} \right)^k \\
&\quad \left(\frac{N-N'}{\bar{N}(x-l)} \right)^{n-k} P(N'; x-l) P(N-N'; x-l) \\
&= \int_0^x dl\ p_i(l) \left(\frac{\bar{N}(x-l)}{\bar{N}(x)} \right)^n \sum_{k=0}^{n} \frac{n!}{k!(n-k)!} \sum_{N'=1}^{\infty} \sum_{N-N'=1}^{\infty} \left(\frac{N'}{\bar{N}(x-l)} \right)^k \left(\frac{N-N'}{\bar{N}(x-l)} \right)^{n-k} \\
&\quad P(N'; x-l) P(N-N'; x-l) \\
&= \int_0^x dl\ p_i(l) \left(\frac{\bar{N}(x-l)}{\bar{N}(x)} \right)^n \sum_{k=0}^{n} \frac{n!}{k!(n-k)!} \sum_{N'=1}^{\infty} \left(\frac{N'}{\bar{N}(x-l)} \right)^k P(N'; x-l) \\
&\quad \sum_{N-N'=1}^{\infty} \left(\frac{N-N'}{\bar{N}(x-l)} \right)^{n-k} P(N-N'; x-l) \\
&= \int_0^x dl\ p_i(l) \left(\frac{\bar{N}(x-l)}{\bar{N}(x)} \right)^n \sum_{k=0}^{n} \frac{n!}{k!(n-k)!} \sum_{N'=1}^{\infty} \left(\frac{N'}{\bar{N}(x-l)} \right)^k P(N'; x-l) \\
&\quad \sum_{N-N'=1}^{\infty} \left(\frac{N-N'}{\bar{N}(x-l)} \right)^{n-k} P(N-N'; x-l) \\
&= \int_0^x dl\ p_i(l) \left(\frac{e^{\alpha(x-l)}}{e^{\alpha x}} \right)^n \sum_{k=0}^{n} \frac{n!}{k!(n-k)!} M_k M_{n-k} \\
&= \int_0^x dl\ p_i(l) e^{-n\alpha l} \sum_{k=0}^{n} \frac{n!}{k!(n-k)!} M_k M_{n-k}
\end{aligned}
\tag{5.11}
$$

5.2.1 Derivation of p(z)

Start from Eq. 4.28 with Eq. 4.27, we found

$$
\begin{aligned}
p(z,x) &= \bar{N}(x) P(\bar{N}(x) z; x) \\
&= \bar{N}(x) \int_0^{\infty} dl\ p_i(l) \sum_{N'=1}^{N-1} P(\bar{N}(x-l) z''; x-l) P(\bar{N}(x) z - \bar{N}(x-l) z''; x-l) \\
&= \bar{N}(x) \int_0^{\infty} dl\ p_i(l) \sum_{N'=1}^{N-1} \frac{p(z''; x-l)}{\bar{N}(x-l)} \frac{p\left(\bar{N}(x-l) \left(\frac{\bar{N}(x)}{\bar{N}(x-l)} z - z'' \right); x-l \right)}{\bar{N}(x-l)}.
\end{aligned}
$$

For large x, the avalanche is well developed and dependence on x disappears. Then, the average number of electrons produced in the avalanche process $\bar{N}$ can be calculated by $N = e^{\int \alpha dx}$, and since x-dependence disappears for large x as mentioned above, α can be regarded as a constant and expressed as $e^{\alpha x}$.

Then,

$$\frac{\bar{N}(x)}{\bar{N}(x-l)} = \frac{e^{\alpha x}}{e^{\alpha(x-l)}} = e^{\alpha l},$$
$$1 = \Delta N' = \bar{N}(x-l)\Delta z''$$

Therefore, we can find

$$\begin{aligned}
p(z,x) &= \bar{N}(x)\int_0^\infty dl\ p_i(l)\sum_{N'=1}^{N-1}\frac{p(z'';x-l)}{\bar{N}(x-l)}\frac{p\left(\bar{N}(x-l)\left(\frac{\bar{N}(x)}{\bar{N}(x-l)}z-z''\right);x-l\right)}{\bar{N}(x-l)} \\
&= \bar{N}(x)\int_0^\infty dl\ p_i(l)\sum_{N'=1}^{N-1}\frac{1}{(\bar{N}(x-l))^2}p(z'')p(ze^{\alpha l}-z'') \\
&= \int_0^\infty dl\ p_i(l)\sum_{N'=1}^{N-1}\frac{\bar{N}(x)}{\bar{N}(x-l)}\frac{1}{\bar{N}(x-l)}p(z'')p(ze^{\alpha l}-z'') \\
&= \int_0^\infty dl\ p_i(l)\int_0^{ze^{\alpha l}} dz''e^{\alpha l}p(z'')p(ze^{\alpha l}-z'') \\
&= \int_0^\infty dl\ p_i(l)e^{\alpha l}\int_z^\infty dz'\delta(z'-ze^{\alpha l})\int_0^{z'} dz''p(z'')p(z'-z'') \\
&= \int_z^\infty dz'\int_0^{z'} dz''p(z'')p(z'-z'')\int_0^\infty dl\ p_i(l)\delta(z'-ze^{\alpha l})e^{\alpha l} \\
&= \frac{1}{\alpha z}\int_z^\infty dz'\int_0^{z'} dz''p(z'')p(z'-z'')p_i\left(\frac{1}{\alpha}\ln\frac{z'}{z}\right)
\end{aligned} \tag{5.12}$$

where $z' = ze^{\alpha l} \rightarrow l = \frac{1}{\alpha}\ln\frac{z'}{z}, e^{\alpha l} = \frac{z'}{z}$, and $dl = \frac{1}{\alpha z'}dz'$

5.2.2 Derivation of $p_i(l)$

Start from Eq. 4.45, we found

$$p_i(l)dl = \frac{\lambda_0^0}{0!}e^{-\lambda_0} \cdot \frac{\lambda_1^1}{1!}e^{-\lambda_1} \tag{5.13}$$

where $\lambda_0 := n\sigma_0(l - x_0)\theta(l - x_0)$ and $\lambda_1 := n\sigma_0\theta(l - x_0)$, then

$$\begin{aligned} p_i(l)dl &= \frac{\lambda_0^0}{0!}e^{-\lambda_0} \cdot \frac{\lambda_1^1}{1!}e^{-\lambda_1} \\ &= e^{-n\sigma_0(l-x_0)}n\sigma_0\theta(l - x_0)e^{-n\sigma_0 dld}dl \\ &= n\sigma_0\ dle^{-n\sigma_0(l-x_0)-n\sigma_0 dl}\theta(l - x_0) \end{aligned} \tag{5.14}$$

By performing Taylor expansion around dl,

$$n\sigma_0 dle^{-n\sigma_0 dl} \simeq n\sigma_0 dl \tag{5.15}$$

Therefore we obtain

$$p_i(l) = e^{-}n\sigma_0(l - x_0)n\sigma_0\theta(l - x_0) \tag{5.16}$$

Acknowledgements

I am deeply grateful to all the ILC physics subgroup members and all the LC-TPC group members for their support and proper guidances, and valuable discussions. I would like to express my deepest appreciation to the supervisor Assoc. Prof. Daniel Jeans for his invaluable guidance and support. His expertise and encouragement helped me to complete this research and write this thesis. At every moment, he has been present and supportive, and has given me the best guidance. This thesis would not have been completed without him. Cycling and skiing with him are wonderful memories.

I would also like to thank Prof. Keisuke Fujii who supervised my second part of this thesis for giving me an opportunity to be involved particle physics. His strong support and advise, and lecture on the physics made enormous contribution to this work.

I also deeply appreciate Prof. Makoto Kobayashi who guided my TPC work for your great lectures on TPC experiments over night and over night. He gave me a lot of supports and detailed advice.

I am especially thankful to reviewing and detailed feedback my referees Assoc. Prof. Kunihiro Nagano. He has always been so kind and supportive. Without his support and kind words, this research would not have been possible.

I express my sincere thanks to Prof. Keisho Hidaka, Dr. Junping Tian, Dr. Ryo Yonamine, Dr. Masakazu Kurata, and Dr. Taikan Suehara for their encouragement and guidance, and constant support.

I am also grateful to members of the KEK Energy Frontier group for their help and support. I also would like to thank the KEK ILC group members, Prof. Akiya Miyamoto, Prof. Toshiaki Tauchi, Dr. Tsunehiko Omori, and Dr. Yasuhiro Sugimoto for their strong support. I am happy to have a fulfilling school life at KEK together with Dr. Tomohisa Ogawa, Dr. Satoshi Higashino, Dr. Haruki Kindo, Mr. Atsushi Mizukami, Dr. Takahiro Mizuno, Dr. Yumi Aoki, Mr. Shoya Fujii, Mr. Shiwen An, Mrs. Jurina Nakajima, and Ms, Misaki Sube.

I would also like to thank Prof. Ronald Dean Settles, Prof. Takeshi Matsuda, Prof. Akira Sugiyama, Prof. Takashi Watanabe, Prof. Yukihiro Kato, Prof. Shinya Narita, Assoc. Prof. Takahiro Fusayasu, and Ms. Aiko Shoji.

My special thanks extended to Dr. Junpei Fujimoto, Dr. Katsumasa Ikematsu, Dr. Shin-ichi Kawada for their kind support and valuable discussions.

I am indebted to the secretaries at KEK, Mrs. Hisako Ohata, Mrs. Hitomi Kusama, Mrs. Yuko Honda, and the member of KEK Public Relations Office Mrs. Mako Kikuchi, and the KEK SOKENDAI office staffs for their kindness and support in my KEK student life. Their significantly important for me to concentrate on my thesis smoothly.

I also would like to appreciate Prof. Hiroshi Igarashi and Dr. Nobuyuki Motoyui for their special lectures on quantum physics and mathematics.

Finally, I aknowledge Prof. Masaomi Shioden who first introduced me to the fascinating world of particle physics. His wonderful lectures led me to the field of particle physics.

Last but not least, I would like to express my deepest gratitude to my family, who brighten my everday, Ryuji Yumino, Naomi Yumino, Ryuta Yumino, Yuki Yumino, Shuta Yumino, Masami Akino, Hisako Akino, my dear dogs Ohagi-chan and Kinako-chan, and my dear cat Tau-chan born in KEK for their love, support, and warm encouragement I have received throughout my life.

REFERENCES

[1] Carsten Burgard, 2016. URL `https://texample.net/tikz/examples/model-physics/`.

[2] Lyndon Evans and Philip Bryant. Lhc machine. *Journal of Instrumentation*, 3(08):S08001, aug 2008. URL `https://dx.doi.org/10.1088/1748-0221/3/08/S08001`.

[3] A Airapetian, V Dodonov, L Micu, D Axen, V Vinogradov, D Akerman, B Szeless, P Chochula, C Geich-Gimbel, P Schacht, et al. *ATLAS detector and physics performance: Technical Design Report, 1.* Number CERN-LHCC-99-014. ATLAS-TDR-014, 1999.

[4] A Airapetian, V Dodonov, L Micu, D Axen, V Vinogradov, D Akerman, B Szeless, P Chochula, C Geich-Gimbel, P Schacht, et al. *ATLAS detector and physics performance: Technical Design Report, 2.* Number CERN-LHCC-99-015. ATLAS-TDR-015, 1999.

[5] S. Chatrchyan et al. The CMS Experiment at the CERN LHC. *JINST*, 3: S08004, 2008.

[6] Collaboration ATLAS. Event display of a H $\rightarrow$ 4e candidate event. URL `http://cds.cern.ch/record/1459495`. General Photo, 2012.

[7] A. D. Martin F. Halzen. *Quarks and Leptons: An Introductory Course in Modern Particle Physics.* John Wiley and Sons Inc, 1984.

[8] D. A. Greenwood W. N. Cottingham. *An Introduction to the Standard Model of Particle Physics.* Cambridge University Press, 2007.

[9] Avelino Vicente. Phenomenology of supersymmetric neutrino mass models. 2011, 1104.0831.

[10] Keisuke Fujii, Christophe Grojean, Michael E. Peskin, Tim Barklow, Yuanning Gao, Shinya Kanemura, Hyungdo Kim, Jenny List, Mihoko Nojiri, Maxim Perelstein, Roman Poeschl, Juergen Reuter, Frank Simon, Tomohiko Tanabe, Jaehoon Yu, James D. Wells, Hitoshi Murayama, and Hitoshi Yamamoto. Physics case for the international linear collider. 2015, 1506.05992.

[11] David London and Jonathan L Rosner. Extra gauge bosons in e 6. *Physical Review D*, 34(5):1530, 1986.

[12] RW Robinett and Jonathan L Rosner. Minimally extended electroweak gauge theories in so (10) and e6. In *AIP Conference Proceedings*, volume 99, pages 193–201. American Institute of Physics, 1983.

[13] Paul Langacker. The physics of heavy z′ gauge bosons. *Reviews of Modern Physics*, 81(3):1199, 2009.

[14] Shuichiro Funatsu, Hisaki Hatanaka, Yutaka Hosotani, Yuta Orikasa, and Naoki Yamatsu. Fermion pair production at e- e+ linear collider experiments in gut inspired gauge-higgs unification. *Physical Review D*, 102(1): 015029, 2020.

[15] Markus Aicheler, PN Burrows, N Catalan, R Corsini, M Draper, J Osborne, Daniel Schulte, Steinar Stapnes, and MJ Stuart. The compact linear collider (clic)-project implementation plan. *arXiv preprint arXiv:1903.08655*, 2019.

[16] Sridhara Dasu, Emilio A Nanni, Michael E Peskin, et al. Strategy for understanding the higgs physics: the cool copper collider. *arXiv preprint arXiv:2203.07646*, 2022.

[17] I Agapov, M Benedikt, A Blondel, M Boscolo, O Brunner, M Chamizo Llatas, T Charles, D Denisov, W Fischer, E Gianfelice-Wendt, et al. Future circular lepton collider fcc-ee: Overview and status. *arXiv preprint arXiv:2203.08310*, 2022.

[18] CEPC Study Group et al. Cepc conceptual design report: Volume 1-accelerator. *arXiv preprint arXiv:1809.00285*, 2018.

[19] João Barreiro Guimarães da Costa, Yuanning Gao, Shan Jin, Jianming Qian, Christopher G Tully, Charles Young, Lian-Tao Wang, Manqi Ruan, Hongbo Zhu, Mingyi Dong, et al. Cepc conceptual design report: Volume 2-physics & detector. 2021.

[20] Rey Hori, 2018. URL `http://www.yk.rim.or.jp/~reyhori/pages/galacc5_e.html`.

[21] Ties Behnke. The international linear collider technical design report-volume 4: detectors. Technical report, Argonne National Lab.(ANL), Argonne, IL (United States); Pacific Northwest, 2013.

[22] Andre Sailer, S Lu, D Hynds, M Frank, R Simoniello, F Gaede, Marko Petric, G Voutsinas, and N Nikiforou. Dd4hep based event reconstruction. In *J. Phys. Conf. Ser.*, volume 898, page 042017, 2017.

[23] Sea Agostinelli, John Allison, K al Amako, John Apostolakis, H Araujo, P Arce, M Asai, D Axen, S Banerjee, G 2 Barrand, et al. Geant4—a simulation toolkit. *Nuclear instruments and methods in physics research section A: Accelerators, Spectrometers, Detectors and Associated Equipment*, 506 (3):250–303, 2003.

[24] Chris Adolphsen. The international linear collider technical design report-volume 3. ii: Accelerator baseline design. Technical report, Argonne National Lab.(ANL), Argonne, IL (United States); Thomas Jefferson ⋯, 2013.

[25] MA Thomson. Particle flow calorimetry and the pandorapfa algorithm. *Nuclear Instruments and Methods in Physics Research Section A: Accelerators, Spectrometers, Detectors and Associated Equipment*, 611(1):25–40, 2009.

[26] K.G. Hayes. τ branching fraction. 2010.

[27] Wolfgang Kilian, Thorsten Ohl, and JŘrgen Reuter. Whizard—simulating multi-particle processes at lhc and ilc. *The European Physical Journal C*, 71(9):1742, 2011.

[28] Stanisław Jadach, Johann H Kühn, and Zbigniew Was. Tauola-a library of monte carlo programs to simulate decays of polarized τ leptons. *Computer Physics Communications*, 64(2):275–299, 1991.

[29] Avery McIntosh. The jackknife estimation method. *arXiv preprint arXiv:1606.00497*, 2016.

[30] P Osland, AA Pankov, and AV Tsytrinov. Identification of extra neutral gauge bosons at the international linear collider. *The European Physical Journal C*, 67:191–204, 2010.

[31] Cesare Bini. Study of the performance of the micromegas chambers for the atlas muon spectrometer upgrade. *Journal of Instrumentation*, 9(02): C02032, 2014.

[32] Ioanis Giomataris. Micromegas: results and prospects. *ICFA Instrumentation Bulletin*, 19, 1999.

[33] Fabio Sauli. Gem: A new concept for electron amplification in gas detectors. *Nuclear Instruments and Methods in Physics Research Section A: Accelerators, Spectrometers, Detectors and Associated Equipment*, 386(2-3): 531–534, 1997.

[34] Fabio Sauli. The gas electron multiplier (gem): Operating principles and application. *Nuclear Instruments and Methods in Physics Research Section A: Accelerators, Spectrometers, Detectors and Associated Equipment*, 805: 2–24, 2016.

[35] Fabio Sauli, L Ropelewski, and P Everaerts. Ion feedback suppression in time projection chambers. *Nuclear Instruments and Methods in Physics Research Section A: Accelerators, Spectrometers, Detectors and Associated Equipment*, 560(2):269–277, 2006.

[36] Tomohisa Ogawa and Yumi Aoki. Simulation study on impact of gem geometry for gas gain uniformity, 2017, 1701.05421.

[37] Penning F M. Über ionisation durch metastabile atome, 1927.

[38] GD Alkhazov. Statistics of electron avalanches and ultimate resolution of proportional counters. *Nuclear Instruments and Methods*, 89:155–165, 1970.

[39] William P Jesse and John Sadauskis. Alpha-particle ionization in mixtures of the noble gases. *Physical review*, 88(2):417, 1952.

[40] H. Schindler, 2012. URL `http://cern.ch/garfieldpp/`.

[41] S. F. Biagi, 1995. URL `http://magboltz.web.cern.ch/magboltz`.

[42] C. Geuzaine and J.-F. Remacle, 2009. URL `https://www.csc.fi/web/elmer`.

[43] CSC IT Center for Science, 2005. URL `https://www.csc.fi/web/elmer`.

[44] Takeshi Fujiwara, Yuki Mitsuya, Hiroyuki Takahashi, T Fushie, S Kishimito, B Guerard, and M Uesaka. The performance of glass gem. *Journal of Instrumentation*, 9(11):P11007, 2014.

[45] Ö Şahin, I Tapan, Emin N Özmutlu, and R Veenhof. Penning transfer in argon-based gas mixtures. *Journal of Instrumentation*, 5(05):P05002, 2010.

[46] S Anvar, P Baron, M Boyer, J Beucher, D Calvet, P Colas, X De La Broise, E Delagnes, A Delbart, F Druillole, et al. Large bulk micromegas detectors for tpc applications. *Nuclear Instruments and Methods in Physics Research Section A: Accelerators, Spectrometers, Detectors and Associated Equipment*, 602(2):415–420, 2009.